**UNIVERSITY OF SOUTHAMPTON**

FACULTY OF ENGINEERING AND THE ENVIRONMENT

COMPUTATIONAL ENGINEERING AND DESIGN GROUP

# Computational simulations of complex chiral magnetic structures

by

**David Ignacio Cortes**

A THESIS SUBMITTED FOR THE DEGREE OF

DOCTOR OF PHILOSOPHY

SUPERVISORS: Prof. Hans Fangohr, Dr. Ondrej Hovorka

October, 2017

UNIVERSITY OF SOUTHAMPTON

ABSTRACT

FACULTY OF ENGINEERING AND THE ENVIRONMENT
COMPUTATIONAL ENGINEERING AND DESIGN GROUP

Doctor of Philosophy

**COMPUTATIONAL SIMULATIONS OF COMPLEX CHIRAL MAGNETIC STRUCTURES**

by David Ignacio Cortes

Since the last century there has been significant progress in the research of novel magnetic materials, which has been stimulated by the development of magnetic based technologies such as information recording. In recent years, advances in imaging and microscopy techniques have allowed the experimental observation of chiral magnetic orderings in a range of materials where Dzyaloshinskii-Moriya interactions (DMI) are present. In particular, a whirling structure known as a magnetic skyrmion has become popular since it can be as small as a few nanometres in size, and its non-trivial topology provides this configuration with an extra stability and particle-like features. It has been demonstrated that these properties make a skyrmion an important candidate for a variety of potential applications, especially for storing information bits. In general, the thermal stability of magnetic structures is an engineering problem that is crucial for any real life application of a magnetic technology. Hence, recently the stability of skyrmions has started to be addressed. In this thesis we investigate, through computer simulations, chiral magnetic structures, with special emphasis on skyrmions, in different materials with DMIs. In addition, we implement a numerical algorithm called the Nudged Elastic Band Method (NEBM) to calculate transition paths and energy barriers between equilibrium states of ferromagnetic systems. The barriers can be used to estimate the average lifetime, and hence stability, of these states. We apply the NEBM to analyse the destruction mechanisms of a skyrmion in a thin film and we find that the lowest energy barrier is associated to the skyrmion annihilation through the boundary of the sample. Furthermore, we study hexagonally shaped ferromagnetic islands to find parameter regions, such as applied field or sample size, where different chiral configurations can be stabilised, combining energy and NEBM calculations. Our results are obtained using computer software developed at our research group in a collaborative manner and we discuss the importance of good coding and data sharing practices for computational based scientific research.

# Contents

# List of Figures

# List of Tables

# Declaration of Authorship

I, David Ignacio Cortes, declare that this thesis entitled "Computational simulations of complex chiral magnetic structures" and the work presented in it are my own and has been generated by me as the result of my own original research. I confirm that:

1. This work was done wholly or mainly while in candidature for a research degree at this University;
2. Where any part of this thesis has previously been submitted for a degree or any other qualification at this University or any other institution, this has been clearly stated;
3. Where I have consulted the published work of others, this is always clearly attributed;
4. Where I have quoted from the work of others, the source is always given. With the exception of such quotations, this thesis is entirely my own work;
5. I have acknowledged all main sources of help;
6. Where the thesis is based on work done by myself jointly with others, I have made clear exactly what was done by others and what I have contributed myself;
7. Parts of this work have been published as:
    - D. Cortés-Ortuño, W. Wang, M. Beg, R. A. Pepper, M.-A. Bisotti, R. Carey, M. Vousden, T. Kluyver, O. Hovorka, and H. Fangohr. *Thermal stability and topological protection of skyrmions in nanotracks.* Scientific Reports, **7**(1):4060, 2017.

Signed:

Date:

# Acknowledgments

I would like to thank Hans Fangohr for his continuous support and research advice during my PhD, and for the experience on computational tools I gained during these years. I also want to thank Ondrej Hovorka for the interesting discussions and his support.

I would also like to acknowledge the Finmag/Fidimag team: Weiwei Wang, Marijan Beg, Ryan Pepper, Marc-Antonio Bisotti, Rebecca Carey, Mark Vousden, Maximilian Albert and Thomas Kluyver, for all the collaborative work on the codes we use in this thesis. And to the experimental group from the University of Hamburg for the discussions and experimental data used in a chapter of this thesis.

In particular, I would like to thank to Weiwei and Marc-Antonio for developing Fidimag. Weiwei, Marijan, Ryan, Ollie and Can for fruitful discussions on research and non-research topics. And Ryan and Ollie for helping me a lot by proof reading this thesis.

Quisiera agradecer a mi amada Romina por su infinito apoyo. A mis padres, mi hermano y mi familia que están lejos y siempre los extraño, y a mis amigos (una larga lista pero yo se que saben quiénes son) en Chile y acá en Southampton. También quiero agradecer a David Laroze y Pedro Landeros en Chile porque me otorgaron las herramientas y apoyo para poder empezar y salir exitoso en este viaje.

I would like to acknowledge financial support from my scholarship sponsor CONICYT with its programme Becas Chile 72140061, the Institute for Complex Systems Simulation with EPSRC's DTC grant EP/G03690X/1, and EPSRC's CDT in Next Generation Computational Modelling grant EP/L015382/1.



# Nomenclature

**Atomistic variables**

| | |
|---|---|
| $\boldsymbol{\mu}$ | magnetic moment |
| $\mathbf{D}_{ij}$ | Dzyaloshinskii vector |
| $\mathbf{s}$ | magnetic moment orientation (opposite to the total angular momentum, see Section 1) |
| $\mathcal{K}_{\mathrm{u}}$ | uniaxial anisotropy constant |
| $\mathscr{H}$ | Hamiltonian |
| $a$ | atomistic lattice constant in plane |
| $a_z$ | atomistic lattice constant along thickness |
| $D$ | Dzyaloshinskii-Moriya constant |
| $J$ | exchange interaction constant |
| $P$ | number of spins |
| $S$ | total spin number |

**Constants**

| | |
|---|---|
| $\mu_{\mathrm{B}}$ | Bohr constant |
| $\hbar$ | reduced Planck constant |
| $g$ | g-factor |

**Micromagnetic Variables**

| | |
|---|---|
| $\mathbf{m}$ | normalised magnetisation field |
| $A$ | exchange constant |
| $D_{\mathrm{c}}$ | Dzyaloshinskii-Moriya constant |
| $E$ | free energy |
| $K_{\mathrm{u}}$ | uniaxial anisotropy constant |
| $M_{\mathrm{s}}$ | saturation magnetisation |

**NEBM variables**

| | |
|---|---|
| $\mathbf{Y}$ | energy band |
| $\mathbf{Y}_i$ | $i$th image of an energy band |
| $N$ | number of images in an energy band |

**Vectors**

| | |
|---|---|
| $\mathbf{B}$ | external magnetic field in Tesla units |
| $\mathbf{r}$ | position vector |

# Introduction

At the beginning of the twentieth century the development of quantum theory allowed the description of magnetism in materials and its origin at the atomic level[1]. The understanding of magnetic phenomena in different materials fostered the technological development of magnetic recording media, which started in the fifties with the creation of the first magnetic hard disk drives. Thereafter, the need for storing massive amounts of data in the smallest possible device has motivated the search for new mechanisms to store information. The current paradigm in magnetic recording is a technique known as perpendicular magnetic recording. This technology is based on a layer of a magnetic material made of assemblies of columnar magnetic grains that can be individually magnetised perpendicularly to the layer plane (up or down). Therefore, these grains are used to write bits of information using a magnetic recording head [3, 4]. Nowadays, the main constraint to this method is the further reduction in size of the magnetic grains: a limit is being reached where a grain's magnetisation randomly fluctuates, phenomenon known as superparamagnetism, which makes them unstable and thus information recording is no longer viable. Trying to address this problem, the scientific community has proposed a variety of alternative magnetic recording technologies [5, 6] but real life application is still challenging for their application due to engineering limitations.

In recent years, research in magnetism has focused on a particular range of materials that have a broken symmetry in the crystal or from effects at the interface when put together with another system. This asymmetry generates an extra interaction between spins, which is known as Dzyaloshinskii-Moriya interaction (DMI), that helps to the stabilisation of chiral structures in the magnetisation field of the material. Although these

[1] It is known from ancient times that magnetic materials orient to a specific direction, which is caused by their interaction with an external field, *e.g.* the Earth's magnetic field. Or they can interact with other particular materials [2]. A magnet can be modelled as having a north and a south pole, a dipole, as can be intuitively observed in magnet bars, where opposite poles attract and similar poles repel each other. These interactions can be explained from the magnetic field that magnets generate around them and from their tendency to align with an external magnetic field. Magnetic phenomena originates at the atomic level due to the movement of electrons and especially by a fundamental property of the electron (such as mass) called *spin*. The spin is a non-trivial concept to define, but it can be thought as a tiny magnet, *i.e.* a magnetic dipole with a specific orientation. Thus, in magnetic materials, which are made of thousands of atoms, spins interact with each other and tend to align under an external magnetic field. Spins can align in different directions according to the intrinsic nature of a material and as a whole, they constitute what is know as *magnetisation* or spin field. If the sum of the orientations generated by all the spins is non zero, for instance if all of them are aligned in the same direction, we say that the material is *magnetised*.

materials were theoretically predicted in the sixties, only recently advances in imaging and microscopy techniques have allowed the experimental observation of chiral configurations in them and to better understand the underlying physics of the DMI. In these antisymmetric materials it has been shown that the DMI has effects on the properties of magnetic structures, such as velocity or stability, that prove beneficial for future technologies [7–9]. In particular, a high interest has fallen upon a swirling magnetic structure known as skyrmion, which resembles a hedgehog or a whirlpool depending on the origin of the DMI. The peculiar topology of a skyrmion makes it a stable configuration against the transition towards other more trivial magnetic structures, thus they can behave as particles. This feature, together with the fact that they can be as small as only a few nanometres in size, create an enormous potential for their application in a variety of magnetic technologies, especially for high density information recording where skyrmions can be used as information bits [7–9].

One of the main restrictions for any data processing and storage technology is the stability of the data, i.e. the robustness of information carriers against random thermal fluctuations at operating temperature. A well established method to analyse the stability of a system is computing what is known as *energy barrier* between two equilibrium states. This barrier is the energy that thermal fluctuations, or any other excitation, needs to provide to the system to drive one equilibrium state to the other. In perpendicular magnetic recording, for example, both a grain pointing up and down are equilibrium states and an energy barrier is the energy necessary to jump from one state towards the other. This energy magnitude can be used to estimate the average time that the system can remain in each state or the average frequency where the system will jump to another state, which is know as transition rate. Therefore, an energy barrier provides the time scale over which information can be stored in the device without corruption. The computation of an energy barrier presumes that the system will follow a transition that requires the least energy cost, known as a minimum energy path.

In 1963, Brown [10] developed a full theoretical model to describe transition rates of single magnetic grains or macrospins. For more complex structures, such as skyrmions, an analytical formulation of their thermal stability is a non-trivial task, thus it is necessary to rely on numerical methods for the calculation of energy barriers. Numerical techniques for the estimation of the thermal stability of large and complex systems have become popular since the increasing availability of computational power of modern times. In this context, a known algorithm for computing energy barriers in magnetic systems, which was originally devised in the context of theoretical chemistry, is the Nudged Elastic Band Method[2] (NEBM) [11–13].

The understanding of the minimum energy paths for the skyrmion transitions, specifically the destruction or creation of a skyrmion, and the energy barrier associated to

[2]The NEBM is a discrete numerical algorithm that works either with a continuum or an atomistic model of a magnetic material. For the former, the continuous magnetisation field is discretised into a mesh of magnetic moments.

these processes, are crucial for their application in future magnetic technologies. This topic has gained noticeable popularity since multiple experimental studies have detected skyrmions in a wide range of materials and the possibility of manipulating them by different methods [7–9], however their thermal stability is not completely comprehended. Some of the challenges for characterising their stability is to know other possible equilibrium states in a particular material and to parameterise the different interactions for the skyrmion stabilisation.

In this thesis we analyse three main topics. Firstly, we study, using computational simulations, the properties of chiral magnetic textures, especially skyrmion-like configurations, in materials where the non-symmetric DMI is present. In this context, at the introductory chapter of this work, where we mathematically explain the magnetism of ferromagnetic materials, we define skyrmions and we numerically solve an analytical model to describe them. Consequently, in Chapter 3 we study skyrmions in cobalt based samples and analyse the effect of the demagnetising field on the skyrmion size. We compare this effect using two different theoretical frameworks to describe a magnetic material: using discrete spins at the atomistic level and a continuum approximation of the material. In Chapter 4 we describe the properties of different magnetic configurations in PdFe islands on top of an iridium surface. This material is known for hosting skyrmions of only a few nanometres in size. Through a collaboration with the group of Roland Wiesendanger from the University of Hamburg, we compare computer simulations of these islands with their experimental findings. In particular, we are interested on the feasibility of observing a magnetic configuration known as target state, which we analyse by hysteresis-like methods or a stability study by means of an external magnetic field.

Secondly, we focus on the calculation of energy barriers of skyrmion-like magnetic orderings. In Chapter 2 we introduce the NEBM and show three simple systems to test this algorithm. Additionally, we explain how a continuum model is not optimal to simulate the transition of a skyrmion, thus making a discrete spin model a preferable option. In Chapter 3 we apply the NEBM to skyrmions hosted in Co stripes to analyse their thermal stability and topological protection. These results are published in Ref. [1]. In Chapter 4 we perform a short study about the stability of a target state in a PdFe island.

Finally, we dedicate Chapter 5 to the discussion of reproducible research and open science in the context of computational simulations. In modern research, these topics have become relevant because of the increasing popularity of computational simulations for the study of physics phenomena. In particular, this thesis is based on computer simulations for the study of magnetic properties of different materials, thus we believe that good practices for coding and sharing data are significantly important for high quality research.

# Magnetism theory

Chapter 1



Magnetic phenomena of materials can be understood by referring to the concept of the *magnetic moment* of atoms. This quantity, which has an associated direction, is a measure of the torque against the influence of an external magnetic field[1] and is directly related to the to the atomic angular momentum. The magnetic moment mainly originates from two sources: the orbital angular momentum and an intrinsic quantum property known as spin. According to how the orbital levels are filled in different materials, a variety of magnetic phenomena can arise, such as ferromagnetism, paramagnetism, diamagnetism, ferrimagnetism or antiferromagnetism. This can also be determined according to the system's response against an external magnetic field. The spin plays a crucial role in the magnetism of solids since, theoretically, the orbital angular momentum itself (*i.e.* using a classical description) cannot explain experimentally observed magnetic interactions (see Bohr-van Leeuwen theorem [14]).

The orbital angular momentum is caused by the motion of electrons around the atomic nucleus and it can be explained using classical theory. It is known from electromagnetic theory that the torque exerted by a magnetic field $\mathbf{B}$ on a magnetic dipole $\boldsymbol{\mu}$ is

$$\boldsymbol{\tau} = \boldsymbol{\mu} \times \mathbf{B} \tag{1.1}$$

If we use a classical picture of an electron orbiting around a nucleus, Bohr's model of the atom, we can relate the magnetic moment to the angular momentum $\mathbf{L}$ and define the corresponding quantum mechanical operator as (See Appendix A for details)

$$\hat{\boldsymbol{\mu}}_L = \frac{(-e)}{2m_e}\hat{\mathbf{L}} = -\frac{\mu_\mathrm{B}}{\hbar}\hat{\mathbf{L}} \tag{1.2}$$

where $e > 0$ is the charge of the electron, $m_e$ its mass and $\mu_\mathrm{B}$ the Bohr magneton

$$\mu_\mathrm{B} = \frac{e\hbar}{2m_e} \approx 9.274 \times 10^{-24}\,\mathrm{J\,T^{-1}} \tag{1.3}$$

For the case of the spin, there is no valid classical picture. Some models, such as the electron devised as a sphere with charge distributed over its surface, lead to wrong conclusions. However, the mathematical formalism to describe the spin is equivalent to the

[1] From the classical theory, it is possible to define the magnetic moment as the dipole term from a tiny loop of current.

one used to describe the angular momentum, thus we can see analogies in their definition. From experiments and quantum mechanical theory, the magnetic moment due to the spin operator $\hat{\mathbf{S}}$ can be defined as

$$\hat{\boldsymbol{\mu}}_S = \frac{g_S(-e)}{2m_e}\hat{\mathbf{S}} = -\frac{g\mu_B}{\hbar}\hat{\mathbf{S}}, \tag{1.4}$$

where $g_S$ is the g-factor and $\mu_B > 0$ is the Bohr magneton. We notice that this expression is similar to the orbital momentum contribution, except for the g-factor, which is approximately 2.002 for the electron. Since we have two main contributions to the angular momentum of the atom we consider the total angular momentum

$$\begin{aligned}\hat{\boldsymbol{\mu}} &= \hat{\boldsymbol{\mu}}_S + \hat{\boldsymbol{\mu}}_L \\ &= -\frac{\mu_B}{\hbar}(g_L\hat{\mathbf{L}} + g_S\hat{\mathbf{S}}) \\ &\approx -\frac{\mu_B}{\hbar}(\hat{\mathbf{L}} + 2\hat{\mathbf{S}}) \\ &= -\frac{\mu_B}{\hbar}(\hat{\mathbf{J}} + \hat{\mathbf{S}}),\end{aligned}$$

where $g_L = 1$ for the g-factor of the orbital angular momentum and where we have assumed $g_S \approx 2$. When computing the time average of the total magnetic moment, it is possible to demonstrate that only the component along $\hat{\mathbf{J}}$ is non zero, hence we can simplify the expression to [15, 16]

$$\hat{\boldsymbol{\mu}} = -\frac{g\mu_B}{\hbar}\hat{\mathbf{J}}, \tag{1.5}$$

with $g$ as the Landé factor.

Although we have defined these relations for a single spin, the commutator relations for the operators still apply for the total orbital angular momentum and spin of a multielectron system, which are defined as

$$\hat{\mathbf{L}}_T = \sum_i \hat{\mathbf{L}}_i \quad \text{and} \quad \hat{\mathbf{S}}_T = \sum_i \hat{\mathbf{S}}_i\,. \tag{1.6}$$

Hence, the total angular momentum is

$$\hat{\mathbf{J}}_T = \sum_i (\hat{\mathbf{L}}_i + \hat{\mathbf{S}}_i) = \sum_i \hat{\mathbf{J}}_i\,. \tag{1.7}$$

In reality, most of the elements are multielectron systems thus, for simplicity, we will call the total operators (and corresponding vectors) $\hat{\mathbf{L}}$, $\hat{\mathbf{S}}$ and $\hat{\mathbf{J}}$. Using a quantum mechanical formalism to solve these systems is not straightforward [17]. In this thesis, we are mostly interested in computing spatially dependent magnetic orderings at zero temperature and a standard method to do this is approximating the total angular momentum operators as classical vectors. Accordingly, based on the Heisenberg Hamiltonian, in the next subsections we explain in detail the assumptions we made to the quantum

magnetism theory. Furthermore, we specify the origin of the dynamics of magnetic moments under the effect of an external field, which we use in the semi classical approximation of the operators to describe different magnetic phenomena at one scale above the atomic level and within a continuum approximation.

## 1.1. Semi-Classical approximation

If we analyse the dynamics of the atomic angular momentum when applying an external field to the system (see Appendix A), it is possible to demonstrate that the expectation value of the corresponding operator[2] precesses around the field, just as we would expect from a classical magnetic moment. We can therefore define the magnetic moment as

$$\boldsymbol{\mu} = -\frac{g_J \mu_B}{\hbar} \left\langle \hat{\mathbf{J}} \right\rangle . \tag{1.8}$$

Within a semi-classical approximation, we can treat these expectation values as classical pseudo-vectors and, to simplify our notation, we will define them in the opposite direction of the angular momentum. In ferromagnets, which are the materials of interest in our study, the main contribution to the angular momentum comes from the spin [14], thus we will refer to the spin **S** rather than **J** in our calculations (though we can still refer to the total angular momentum by using the $g_J$ Landé factor instead of $g_S$). Therefore, setting **S** as a classical vector antiparallel to the angular momentum expectation value[3] as

$$-\frac{1}{\hbar} \left\langle \hat{\mathbf{S}} \right\rangle \longrightarrow \mathbf{S}, \tag{1.9}$$

we define the magnetic moment of an atom as

$$\boldsymbol{\mu} = g \mu_B S \mathbf{s}, \tag{1.10}$$

where **s** is the magnetic moment direction unit vector and $S = |\mathbf{S}|$ must be considered as an *effective* total spin (angular momentum) magnitude[4]. Using Hund's rule to compute the atomic ground state of a multielectron system and estimate the expectation value of the angular momentum operator, we might think that $\boldsymbol{\mu}$ should be given in integers of $\mu_B$. However, for a real material, effects from the crystal lattice perturb $\boldsymbol{\mu}$ to give a non-integer number of Bohr magnetons per atom [2, 14]. In principle, a more accurate approximation of the magnetic moment magnitude can be computed from theory that considers delocalised electrons but, for our purposes, we will use an effective value

[2] We must have present that in a quantum mechanical theory, we can only measure the component of the operator along a quantisation axis, which is usually taken as the $z$ axis [2].

[3] We set the $\hbar$ factor on the basis that for a wavefunction $|L, L_z, S, S_z\rangle$, the expectation value of $\hat{L}^2$ is $\hbar^2 L(L+1)$.

[4] Remember that, quantum mechanically, a system with spin $S$ has $(2S+1)$ possible discrete values for the $\hat{S}_z$ operator.

taken from published results based on experiments or *ab initio* calculations. This works well when we assume localised magnetic moments, as we explain in more detail in Subsection 1.2, hence it is more common in the literature to define the magnetic moment direction as

$$\mathbf{s} = \frac{\boldsymbol{\mu}}{|\boldsymbol{\mu}|}, \tag{1.11}$$

and the magnitude of the magnetic moment is taken in Bohr magneton units as we explained before.

## 1.2. Localised magnetic moments

To describe a magnetic material we will model the atoms as having localised magnetic moments at fixed atomic sites, which are arranged in a lattice according to the crystallographic structure of the material. This picture can be formulated mathematically as the Heisenberg Hamiltonian which models the direct exchange interaction between neighbouring spins (see Section 1.4). This model can be extended to include the interaction of spins with an external magnetic field or interactions arising from the material.

The concept of localised magnetic moments works well for magnetic insulators [17] or $4f$ metals. For the case of ferromagnetic transition metals, such as Fe, Co and Ni, they are better represented by a free electron gas model where itinerant electrons are completely delocalised, for example the Hubbard model. On the other hand, assuming localised moments is useful to describe the variation of the magnetic moments in space [14] to find the ground state of a magnetic system and it can explain different thermodynamic properties. In addition, a perturbation expansion applied to the Hubbard model and using classical spins vectors, leads to the Heisenberg Hamiltonian as a second order perturbation [18]. Although choosing any of these two models will inevitably make assumptions and not account for every possible physical effect, we choose localised magnetic moments since it has been successful in accurately depicting magnetic orderings in comparison with experimental data [19–21]. Moreover, this model allows us to easily compute magnetic interactions between spins, which are the main cause of the variety of observed magnetic structures.

## 1.3. Continuum approximation

When the sizes of magnetic samples are large enough, a quantum or atomistic description of these systems is not effective because a system with a significant number of spins increases the complexity of the theory to obtain an analytical solution or makes it more difficult to achieve a numerical solution. In this case we will rely on an approximation of the magnetic interactions known as micromagnetics. This theory has been successful to describe a vast number of magnetic phenomena, such as the formation of domains,

in systems with dimensions ranging from a few nanometres up to the scale of micrometres.

Micromagnetics is the limit to the continuum of a material where, instead of treating single spins in a lattice, $\mathbf{S}_i$, we use a magnetisation field $\mathbf{M}(\mathbf{r})$, $\mathbf{r} = (x, y, z)$ being a spatial vector pointing into the $(x, y, z)$ coordinate. The micromagnetic approximation is based on the hypothesis of a slowly varying spatial variation of the magnetisation at the scale of the atomic sites such that the spin field in the medium can be approximated as a continuum. This approximation is often shown as the limit $\mathbf{s} \to \mathbf{M}/M_s$, with $M_s$ as the saturation magnetisation, which is obtained by measuring the system average magnetisation under a strong magnetic field, in order to uniformly magnetise the sample. The magnetisation $\mathbf{M}$ is defined as the magnetic moment $\boldsymbol{\mu}$ per unit volume and assuming a homogeneous sample, we can write

$$\mathbf{M} = M_s \mathbf{m} = \frac{|\boldsymbol{\mu}|}{\Delta V}\mathbf{m} = \frac{g\mu_B S}{\Delta V}\mathbf{m} \tag{1.12}$$

where $\Delta V$ is the volume of the unit cell, $g$ the Landé factor, $\mu_B$ the Bohr magneton, $M_s$ the saturation magnetisation and $\mathbf{m}$ the unit magnetisation field vector, which is a spatial dependent spin direction.

It is worth mentioning that we will apply the micromagnetic theory at zero temperature, where $M_s$ is constant.

## 1.4. Magnetic interactions

Among the different magnetic phenomena found in nature, ferromagnetism is characterised by materials where neighbouring magnetic moments tend to align parallel between each other, producing a non zero average magnetisation in absence of an external magnetic field and below a critical temperature known as Curie temperature. The main mechanism responsible for this phenomenon is of quantum origin: it is caused by the symmetry[5] of the material wave functions (particles) and the Coulomb interaction between electrons (see Ref. [14] and page 180 of [2]), which favours the parallel alignment of neighbouring spins. The result is a short range interaction known as Exchange interaction. Apart from the exchange, magnetic moments also interact by other quantum effects such as spin orbit coupling, which generates anisotropy, or by response to external or internal fields. As a result, these interactions generate an effective internal field that can be used to compute the evolution of the spins according to the Landau Lifshitz equation, or to minimise the energy of the system. Mathematically, the effective field at the $i$th lattice site $\mathbf{H}_{\text{eff}}^{(i)}$ for a given interaction, can be computed from the corresponding Hamiltonian $\mathscr{H}$ as

[5] Electrons are fermions thus their wavefunction must be antisymmetric. This conveys the famous Pauli exclusion principle.

$$\mathbf{H}_{\text{eff}}^{(i)} = -\frac{1}{\mu}\frac{\partial \mathscr{H}}{\partial \mathbf{s}_i}. \tag{1.13}$$

In taking the continuum limit, the Hamiltonian becomes a functional and therefore, the partial derivative turns into a functional derivative [22]. To distinguish the free energy in this limit, from the discrete Hamiltonian, we use the notation $E = E(\mathbf{r})$. The effective field is then

$$\mathbf{H}_{\text{eff}}(\mathbf{r}) = -\frac{1}{\mu_0 M_s}\frac{\delta E(\mathbf{r})}{\delta \mathbf{m}}. \tag{1.14}$$

The next Subsections are dedicated to explain and formally describe these interactions in the context of ferromagnets, both from a discrete spin and a micromagnetic theoretical framework.

### 1.4.1. Exchange Interaction

Theoretically, direct ferromagnetic exchange interactions between spins can be described in a simplified manner using the Heisenberg Hamiltonian. Within a discrete spins formalism in the semi-classical approximation, it has the expression

$$\mathscr{H}_{\text{ex}} = -\sum_{\substack{\langle i,j\rangle \\ i\neq j}}^{N} \mathbf{S}_i \cdot \mathbf{J}_{ij} \cdot \mathbf{S}_j \,, \tag{1.15}$$

where $\mathbf{J}_{ij}$ is a symmetric exchange tensor[6], $\mathbf{s}_i$ and $\mathbf{s}_j$ are the spin directions at lattice sites $i$ and $j$ respectively, $N$ is the number of spins in the sample and the summation refers to counting pairs of neighbouring spins only once. For our study, the tensor will be diagonal and if we assume homogeneous materials, we can just write it as a constant, i.e. $\mathbf{J}_{ij} \approx J$. The corresponding field at the $i$th lattice site in this approximation is

$$\mathbf{H}_{\text{ex}} = \sum_{j\neq i}^{\text{NN}} \mathbf{J}_{ij} \cdot \mathbf{S}_j \approx \sum_{j\neq i}^{\text{NN}} J\,\mathbf{S}_j \,. \tag{1.16}$$

Starting from this model it is possible to approximate the discrete mathematical expression into the continuum limit, considering the crystal lattice geometry [14,23] and a slow spatial variation of the magnetisation (see Section 1.3). Accordingly, the exchange energy can be expressed as

$$E_{\text{ex}} = A\int_V \mathrm{d}V(\boldsymbol{\nabla}\mathbf{m})^2 = A\int_V \mathrm{d}V\left(\sum_{\alpha=x,y,z}(\boldsymbol{\nabla} m_\alpha)^2\right), \tag{1.17}$$

with $V$ as the volume of the magnetic material, $A$ as an exchange constant (in Joules per metre units), which depends on the crystallographic nature of the sample, and $\mathbf{M} =$

[6] Using a quantum mechanical approach, direct exchange interactions can be described by an *exchange integral*. The exchange tensor approximates this integral for the Heisenberg Hamiltonian [2, 14].

$M_s\mathbf{m}$ the continuous magnetisation field. The exchange constant can be estimated experimentally for complex materials, but it can also be derived for simple lattice structures. Referring to [14], we can relate the constant to the discrete model using

$$A = \frac{JS^2c}{2a_z}. \tag{1.18}$$

In equation 1.18, $J$ is the Heisenberg exchange integral approximation for a homogeneous material, $S$ is the effective total spin, $a_z$ is a lattice constant along the thickness, which we choose as the $z$ direction, and $c$ a crystal constant. It is often the case that $J$ is taken as $S^2$ $J$. The crystal constant has the values $c = 1, 2, 4$ for SC, BCC and FCC structures, respectively. In this context, Aharoni [14] states that $c = 2\sqrt{2}$ for a hexagonal close-packed crystal, however, if we consider a hexagonal structure in two dimensions we obtain $c = \sqrt{3}$, which we derive in Appendix C.

### 1.4.2. Zeeman Interaction

The interaction of the spins with an external magnetic field can be described within the atomistic model as

$$\mathscr{H}_{\text{Zeeman}} = -\sum_{i}^{N} \mu_i \mathbf{B} \cdot \mathbf{s}_i \tag{1.19}$$

In the continuum limit this expression reads

$$E_{\text{Zeeman}} = -\mu_0 \int_V \mathrm{d}V \mathbf{H} \cdot \mathbf{M} \tag{1.20}$$

In these equations, $\mathbf{B} = \mu_0\mathbf{H}$ is the applied external field, with $\mu_0$ as the vacuum permeability. The field $B$ is given tesla units and $\mathbf{H}$ is given in ampere per meter units.

### 1.4.3. Anisotropy

Anisotropy refers to preferred directions where spins tend to align, which depends on the magnetic crystal nature. When this direction is determined by a unique axis, we have an uniaxial anisotropy. In the discrete spins framework the Hamiltonian is written as

$$\mathscr{H}_{\text{a}} = -\sum_{i}^{N} \mathcal{K}_i \left(\mathbf{s}_i \cdot \hat{\mathbf{u}}\right)^2 \tag{1.21}$$

The micromagnetic version of this expression is straightforward to derive and reads

$$E_{\text{a}} = -\int_V \mathrm{d}V \, K(\mathbf{r}) \left(\mathbf{m} \cdot \hat{\mathbf{u}}\right)^2 \tag{1.22}$$

In both equations, $\mathcal{K}$ and $K$ are the anisotropy constant, given in Joules for the discrete model and in Joules per cubic metre in the continuum, and $\hat{\mathbf{u}}$ is the unit vector

describing the anisotropy axis. When $\mathcal{K}$ and $K > 0$, spins tend to align to $\hat{\mathbf{u}}$ since this decreases the overall energy of the system, and the plane perpendicular to this axis is known as *hard* plane. Otherwise, we would have a hard axis and an easy plane. In expressions 1.21 and 1.22, the anisotropy constants can vary spatially, but for the majority of the studies these parameters are taken as constants along the sample, assuming an homogeneous material.

Other kinds of anisotropy depend on the symmetries of the magnetic sample. For example, a shape anisotropy is induced by the dipolar interaction in uniformly magnetised samples, a magneto elastic anisotropy is the product of the stress applied to the system and surface anisotropies originate from the crystal structure at the surface of the system [14, 24]. Most of these have a mathematical expression for the energy similar to an uniaxial anisotropy. A derivation of the expressions to describe different anisotropies can be found in a theoretical study from Lindner and Farle [25].

### 1.4.4. Dzyaloshinskii-Moriya Interactions

These interactions arise due to broken symmetries in a magnetic material and the underlying mechanism generating them differ according to the geometry and crystal nature of the sample. They were phenomenologically predicted by Dzyaloshinskii [26] in the context of antiferromagnetism, and later analytically studied by Moriya [27]. They are also called anisotropic exchange interactions (AEIs) since they can be described through the non-diagonal components of the exchange tensor $\mathbf{J}_{ij}$. In the following we will explain the most commonly discussed kind of DMIs found in ferromagnetic materials.

In some specific bulk ferromagnetic systems, such as the so called B20-type compounds FeGe and MnSi, which belong to the $P2_13$ space group, AEIs are present due to a broken group symmetry in the crystal or molecule structure, hence they are also known as bulk DMIs. Mathematical expressions to describe them can be derived expanding the free energy with respect to the symmetries of the material where, in the continuum limit, gives rise to energy terms that are linear with respect to the first spatial derivative of the magnetisation. These terms are known as Lifshitz invariants and they were applied by Bogdanov and Yablonskii [28, 29] to describe the formation of vortices in magnetic crystals of specific crystallographic groups or classes. Later, they were named DMIs [30, 31]. Formally, Lifshitz invariants[7], normalised by the quadratic mag-

[7] These are linear terms with respect to the first spatial derivative of an order parameter, in our case the magnetisation, that are invariants with respect to the symmetry operations of the space group of the material. In a ferromagnetic material the DMI energy density is expressed in terms of these quantities. Lifshitz invariant-like terms were originally studied by Landau and Lifshitz in the context of second order phase transitions, where the thermodynamic potential of a crystal lattice is expanded in terms of an order parameter that depends on the symmetry group of the crystal [32]. The same formalism was applied by Dzyaloshinskii in his phenomenological studies about antiferromagnets and weak ferromagnetism [26, 33]. In Ref. [34] Bak and Jensen expand the free energy of the $P2_13$ space groups materials FeGe and MnSi, obtaining a term that can be expressed as a Lifshitz invariant. This is possibly the first known example of Dzyaloshinskii's theory applied to a ferromagnetic material.

netisation norm $M_s^2$, are defined as

$$\mathcal{L}_{ij}^{(k)} = m_i \frac{\partial m_j}{\partial x_k} - m_j \frac{\partial m_i}{\partial x_k}\,, \tag{1.23}$$

where $i, j, k \in \{x, y, z\}$. Recent experimental works have reported the observation of chiral magnetic structures stabilised by DMIs in a variety of these non symmetric materials: the $T$ class (or B20) metallic compounds FeGe [35, 36], MnSi [37], MnGe [38] and $Fe_{1-x}Co_xSi$ [39–41], the $T$ class insulator $Cu_2OSeO_3$ [42, 43], the $O$ class metallic alloys $Co_xZn_yMn_z$ [44] and $(Fe,Co,Rh)_2Mo_3N$ [45], the $D_{2d}$ class Mn-Pt(Pd)-Sn Heusler compounds [46] and the $C_{3v}$ semiconductor and insulator $GaV_4S_8$ [47].

Other materials where AEIs arise are those with broken symmetries on surfaces or interfaces. In this context Moriya [27] explained through a relativistic treatment AEIs for the surfaces of materials using Dzyaloshinskii's theory of antisymmetric spin coupling. A summary of his work can be found in the paper of Crépieux and Lacroix [48]. In addition, in Ref. [48] it is explained an AEIs 3-sites mechanism, originally proposed by Fert and Levy [9, 49], which has been experimentally relevant in the last years. In very thin samples this 3-sites mechanism originates from the spin-orbit coupling (SOC) effect between atoms in two different ways [9, 49]:

1. at the interface of a magnetic layer and a heavy metal, where every pair of atoms in the magnet interact with a third atom in the metallic material, which has a strong SOC,

2. in a magnetic layer from the interaction of two magnetic spins with a third non-magnetic atom that has a large SOC.

The interactions caused by the breaking of inversion symmetry at the interface (1.) are known as interfacial DMIs and they have been experimentally proven in different Cobalt [50–55] and Iron [56–59] based systems [8, 9] and Manganese on Tungsten [60, 61] samples.

Recent experimental works have tried to explain the dependence of the interfacial DMI on the thickness of the sample [62]. It has been observed that the DMI is mainly present in the magnetic monolayer next to the interface with the non magnetic sample [63].

Mathematically, the discrete Hamiltonian for any kind of DMI has the structure[8]

[8] This expression was theoretically derived by Moriya using Anderson's theory of superexchange [27]. As an anisotropic exchange, it can be written as equation 1.15 using the off diagonal terms of the exchange matrix. Specifically, we can decompose the exchange tensor [64] into a sum of an isotropic, a symmetric (S) and an antisymmetric (A) term as $\mathbf{J}_{ij} = J_{ij}\mathbf{I} + \mathbf{J}_{ij}^{\mathrm{A}} + \mathbf{J}_{ij}^{\mathrm{S}}$, with $\mathbf{I}$ as the identity matrix. The first term leads to an isotropic exchange $J_{ij} = (1/3)\mathrm{Tr}\mathbf{J}_{ij}$, the second is a traceless symmetric tensor $\mathbf{J}_{ij}^{\mathrm{S}} = (1/2)(\mathbf{J}_{ij} + \mathbf{J}_{ij}^{T}) - J_{ij}\mathbf{I}$, which leads to a symmetric anisotropic exchange [65], and the final term is an antisymmetric tensor $\mathbf{J}_{ij}^{\mathrm{A}} = (1/2)(\mathbf{J}_{ij} - \mathbf{J}_{ij}^{T})$. This last term can be used to express the antisymmetric DMI expression 1.24 by converting $\mathbf{S}_i \cdot \mathbf{D}_{ij} \cdot \mathbf{S}_j$, with $\mathbf{D}_{ij} = \mathbf{J}_{ij}^{\mathrm{A}}$, to a cross product.

$$\mathscr{H}_{\mathrm{DM}} = \sum_{\langle i,j \rangle} \mathbf{D}_{ij} \cdot \mathbf{S}_i \times \mathbf{S}_j \,, \tag{1.24}$$

where $\mathbf{D}_{ij}$ is the Dzyaloshinskii tensor, which depends on the material. For example,

$$\mathbf{D}_{ij} = D\hat{\mathbf{r}}_{ij} \,, \tag{1.25}$$

with $\hat{\mathbf{r}}_{ij}$ the unit direction vector from the $i$th site to the $j$th site in the lattice, can be found when discretising the micromagnetic DMI expression of specific materials with bulk DMI[9] (further below we explain the continuum expression of the DMI energy). It can also be found in specific systems with the Fert-Levy AEI [48]. Another well known case is

$$\mathbf{D}_{ij} = D\hat{\mathbf{r}}_{ij} \times \hat{z} \,, \tag{1.26}$$

which is typical of ferromagnetic layers with interfacial DMI [9, 63, 66], where the film plane lies in the $xy$ plane.

The structure of the Hamiltonian in equation 1.24 favours the canting of neighbouring spins in a plane perpendicular to the Dzyaloshinskii vector, thus, when in competition with symmetric exchange, it helps to stabilise twisted magnetic structures such as helicoids or skyrmions. Furthermore, the sign of the DMI constant $D$ (or the vector direction), determines the chirality of the system, *i.e.* the sense of rotation of the spiral structures favoured by the DMI.

In the continuum limit, it is possible to derive expressions for the two aforementioned cases, where we will also show them employing the Lifshitz invariants notation. For the particular case of *parallel* DMI of equation 1.25 and setting $D_{\mathrm{c}}$ as the DMI constant in the micromagnetic limit, we have

$$\begin{aligned} E_{\mathrm{DM}} &= D_{\mathrm{c}} \int \mathrm{d}V \, \mathbf{m} \cdot (\boldsymbol{\nabla} \times \mathbf{m}) \\ &= D_{\mathrm{c}} \int \mathrm{d}V \, \left( \mathcal{L}_{yx}^{(z)} + \mathcal{L}_{xz}^{(y)} + \mathcal{L}_{zy}^{(x)} \right) \,. \end{aligned} \tag{1.27}$$

The energy expression 1.27 is valid for cubic helimagnets ($T$ and $O$ crystal classes) and uniaxial ferromagnets with $D_n$ symmetry [28, 67–69]. For other bulk geometries with a broken crystal symmetry, Bogdanov summarised a list with invariants for different point groups [28] that are directly obtained in the continuum model using crystallographic symmetries.

In the case of two dimensional samples with interfacial DMI, *i.e.* equation 1.26, and systems with $C_{nv}$ symmetry class [28, 29, 67–69], the energy can be described as

[9] Notice that, usually, bulk antisymmetric materials have a very complex crystal structure, thus an expression for the discrete $\mathbf{D}_{ij}$ vector is not straightforward to derive. It could probably be accomplished computing the DMI vectors from first principles.

$$\begin{aligned} E_{\mathrm{DM}} &= D_{\mathrm{c}} \int \mathrm{d}V\, \mathbf{m} \cdot \left[ (\boldsymbol{\nabla} \cdot \mathbf{m})\, \hat{\mathbf{z}} - \boldsymbol{\nabla} m_z \right] \\ &= D_{\mathrm{c}} \int \mathrm{d}V \left( \mathcal{L}_{xz}^{(x)} + \mathcal{L}_{yz}^{(y)} \right) , \end{aligned} \tag{1.28}$$

where $\hat{\mathbf{z}}$ is a unit vector perpendicular to the sample plane.

In general, if the lattice structure is simple enough it is possible to derive a micromagnetic expression for the energy starting from the discrete Hamiltonian, in a similar fashion as the exchange interaction calculation. For instance, the form of equation 1.28 is the same for a square or hexagonal two dimensional lattice, and the lattice information is only present in the DMI constant. In Appendix B we show that approximating $\mathbf{D}_{ij}$ as a constant and using $a_z$ as the thickness of the sample and $a$ as the lattice constant, we obtain, after some algebra, that $D_{\mathrm{c}} = D_{ij} S^2 (a a_z)^{-1}$ for the square and $D_{\mathrm{c}} = D_{ij} \sqrt{3} S^2 (a a_z)^{-1}$ for the hexagonal geometry (usually, the $S^2$ factor is implicit in the $D_{ij}$ term). Interestingly, the Lifshitz invariants form of equation 1.28 has the same expression than the one for a system of symmetry class $C_{nv}$. For other materials or geometries, an expression could be obtained if the Dzyaloshinskii vectors are known, which, in principle, can be calculated by Moriya's symmetry rules [48].

The sign of the DMI constants $D$ or $D_{\mathrm{c}}$, which sets the direction of the Dzyaloshinskii vector, specifies the chirality or preferred sense of rotation of spins. For example, in the case of Co layers on Pt, which we study in Chapter 3, the DMI constant of equation 1.26 or 1.28 is negative.

### 1.4.5. Dipolar interactions

A magnetic dipole, or magnetic moment, can be considered a magnetic field source. The interaction of the magnetic moments with the field of the other dipoles are known as dipolar interactions, and the total field generated by the magnetic moments (which can be seen as the magnetic field generated by the material itself) is known as demagnetising field. In a discrete spin model, the dipolar energy has the structure

$$\mathscr{H}_{\mathrm{d}} = -\frac{\mu_0}{4\pi} \sum_{i}^{N} \sum_{i \neq j} \frac{3 \left( \boldsymbol{\mu}_i \cdot \hat{\mathbf{r}}_{ij} \right) \left( \boldsymbol{\mu}_j \cdot \hat{\mathbf{r}}_{ij} \right) - \boldsymbol{\mu}_i \cdot \boldsymbol{\mu}_j}{r_{ij}^3} \tag{1.29}$$

$\hat{\mathbf{r}}_{ij}$ is the normalised direction vector from the $i$th lattice site to the $j$th point, *i.e.* $\mathbf{r}_{ij} = \mathbf{r}_j - \mathbf{r}_i$ and $r_{ij} = \left| \mathbf{r}_j - \mathbf{r}_i \right|$. Correspondingly, the field at the $i$th lattice point, has the form

$$\mathbf{H}_{\mathrm{d}} = \frac{\mu_0}{4\pi} \sum_{i \neq j} \frac{3 \hat{\mathbf{r}}_{ij} \left( \boldsymbol{\mu}_j \cdot \hat{\mathbf{r}}_{ij} \right) - \boldsymbol{\mu}_j}{r_{ij}^3} \tag{1.30}$$

Compared to the other energy terms, this is one of the most computationally expensive calculations, even in the continuum limit, thus different numerical methods have been developed to estimate them [70–73].

The dipolar energy in the continuum is described as

$$E_{\mathrm{d}} = -\frac{\mu_0}{2}\int \mathrm{d}V\, \mathbf{M}\cdot\mathbf{H}_{\mathrm{d}} \tag{1.31}$$

with $\mathbf{H}_{\mathrm{d}}$ as the dipolar field (also know as demagnetising or stray field). Looking at Maxwell's equation in a ferromagnetic body,

$$\boldsymbol{\nabla}\times\mathbf{H}_{\mathrm{d}} = 0 \tag{1.32}$$

in the absence of free currents, thus the dipolar field can be calculated using a potential function $\Phi$ such that

$$\mathbf{H}_{\mathrm{d}} = -\boldsymbol{\nabla}\Phi. \tag{1.33}$$

If we now use Maxwell's equation for the zero total magnetic flux through a surface

$$\boldsymbol{\nabla}\cdot\mathbf{B} = 0, \tag{1.34}$$

with $\mathbf{B} = \mu_0(\mathbf{H}+\mathbf{M})$, which considers the magnetisation in the material, the potential $\Phi$ can be obtained directly by replacing 1.33 into 1.34 and solving the resulting Poisson equation

$$\nabla^2\Phi = \boldsymbol{\nabla}\cdot\mathbf{M} \tag{1.35}$$

with the boundary conditions (from the condition of continuity of the fields) [14]

$$\Phi_{\mathrm{in}} = \Phi_{\mathrm{out}} \qquad (\boldsymbol{\nabla}\Phi_{\mathrm{out}} - \boldsymbol{\nabla}\Phi_{\mathrm{in}})\cdot\hat{\mathbf{n}} = \mathbf{M}\cdot\hat{\mathbf{n}} \tag{1.36}$$

where the potential is taken inside or outside the magnetic volume $V$ with surface $\Omega$, using $\hat{n}$ as the vector pointing normal to the volume surface. Notice that if there is no material outside the ferromagnetic body $\Phi_{\mathrm{out}} = 0$ and we have a Laplace equation for $\Phi_{\mathrm{out}}$. Alternatively, we can use the general solution of the differential equation after employing a Green's function formalism

$$\Phi = -\left\{\int_V \frac{\boldsymbol{\nabla}'\cdot\mathbf{M}(\mathbf{r}')}{|\mathbf{r}-\mathbf{r}'|}\mathrm{d}V' - \int_\Omega \frac{\hat{\mathbf{n}}\cdot\mathbf{M}(\mathbf{r}')}{|\mathbf{r}-\mathbf{r}'|}\mathrm{d}\Omega'\right\} \tag{1.37}$$

Analytical expressions for the demagnetising field of magnetic systems with complex magnetisation configurations, are not straightforward to derive. Therefore, when not employing numerical methods it is possible to use approximations in specific geometries. For instance, in thin samples dipolar interactions are usually approximated as a surface anisotropy with a hard axis perpendicular to the sample plane. This is based on the fact that, for systems with ellipsoidal shapes and uniform magnetisation, the demagnetising energy can be described as an effective anisotropy (also called shape anisotropy).

## 1.5. Dynamics

The dynamics of the magnetic moments in a magnetic solid can be derived from the precessional motion of a spin under an effective magnetic field $\mathbf{H}_{\text{eff}}$ (see equations 1.13 and 1.14). Starting from the quantum mechanical evolution of the spin operator within the Heisenberg picture and then taking a semi classical approximation [22, 74, 75], it is possible to obtain the evolution in time $t$ of the spins (see Appendix A). However, this equation does not consider dissipation of energy, which occurs in reality by mechanisms such as spin wave emission or lattice vibrations [22]. To address this phenomenon, Landau and Lifshitz added a phenomenological damping term. Later, Gilbert introduced this dissipation term to the classical spin dynamical equation in the continuum, using a Lagrangian formalism and a Rayleigh dissipation functional [22]. Both the Landau-Lifshitz and Gilbert forms for the dynamical equation agree (they are related by a transformation of the damping constant) and they accurately describe the dynamics of the spins both in the discrete spins and micromagnetic frameworks. We will use the version of the dynamical equation known as Landau-Lifshitz-Gilbert equation [75, 76], which reads

$$\frac{\partial \boldsymbol{\mu}}{\partial t} = -\gamma\, \boldsymbol{\mu} \times \mathbf{H}_{\text{eff}} + \frac{\alpha_{\text{G}}\gamma}{\mu}\, \boldsymbol{\mu} \times \boldsymbol{\mu} \times \mathbf{H}_{\text{eff}}\,. \tag{1.38}$$

In equation 1.38, $\gamma = g\mu_{\text{B}}\hbar^{-1} > 0$ is the gyromagnetic ratio and $0 \leq \alpha_{\text{G}} \leq 1$ is an effective Gilbert damping constant. In the continuum limit, this equation is written as

$$\frac{\partial \mathbf{M}}{\partial t} = -\gamma \mathbf{M} \times \mathbf{H}_{\text{eff}} + \frac{\alpha_{\text{G}}\gamma}{M_{\text{s}}} \mathbf{M} \times \mathbf{M} \times \mathbf{H}_{\text{eff}}\,. \tag{1.39}$$

The damping term makes the magnetisation to decay towards the magnetic field and comes from Gilbert's variational Lagrangian formalism (see page 40 in [75]) applied to the spins evolution equation.

The Landau-Lifshitz-Gilbert equation is used by spin dynamics solvers, such as Finmag [77] and Fidimag [78], to find equilibrium configurations by evolving the system until relaxation, which means $|\partial_t \mathbf{s}| \to 0$ or $|\partial_t \mathbf{m}| \to 0$.

In micromagnetics, an alternative method to find equilibrium states is to apply Brown's equation:

$$\mathbf{M} \times \mathbf{H}_{\text{eff}} = 0 \tag{1.40}$$

with appropriate boundary conditions [14].

## 1.6. Topological numbers

To characterise chiral or non trivial magnetic structures such as skyrmions, which we analyse along this thesis, we are going to employ two mathematical definitions known as *topological charge* and *skyrmion number*. In the context of magnetism, these quantities

measure the number of times that the spin or magnetisation field, restricted to a two dimensional plane, wraps or cover a three dimensional sphere.

### 1.6.1. Topological charge

The topological charge is defined for discrete spin lattices and it is based on computing the spherical angle spanned by triplets of neighbouring spins per every lattice site. This concept was proposed by Berg and Lüscher [79] and, recently, applied by Yin et al. [80] to square arrangements. In this work we have extended the definition to hexagonally arranged lattices (see Supplementary Material of Ref. [1]).

Mathematically, the total topological charge is defined as

$$Q = \sum_{\nu}^{P} q_\nu = \sum_{\nu}^{P} \frac{1}{4\pi} \left(\Omega_{\nu,1,2} + \Omega_{\nu,3,4}\right) , \tag{1.41}$$

where the summation is over $P$ lattice positions of the sample and the $\Omega$ terms are the areas of the spherical triangles, or solid angles, whose vertexes are given by the sets of three neighbouring spins $(\mathbf{s}_\nu, \mathbf{s}_1, \mathbf{s}_2)$ and $(\mathbf{s}_\nu, \mathbf{s}_3, \mathbf{s}_4)$, at every lattice position $\nu$. In a square and hexagonal lattice arrangement, the sets of spins specified per lattice site are depicted in Fig. 1.1a and b respectively (it would be equivalent to use the opposite triangular sets that also cover a unit cell, *e.g.* we could use $\Omega_{\nu,2,3}$ and $\Omega_{\nu,4,1}$ for the square lattice) and Fig. 1.1c shows how the spherical triangle area is defined by the spin triplet $(\mathbf{s}_\nu, \mathbf{s}_1, \mathbf{s}_2)$. The solid angle at the $\Omega_{\nu,1,2}$, which is defined with respect to the neighbouring spins $\mathbf{s}_1$ and $\mathbf{s}_2$, is computed as[10]

$$\exp\left(\frac{1}{2}\mathrm{i}\Omega_{\nu,1,2}\right) = \frac{1}{\rho}\left[1 + \mathbf{s}_\nu \cdot \mathbf{s}_1 + \mathbf{s}_1 \cdot \mathbf{s}_2 + \mathbf{s}_2 \cdot \mathbf{s}_\nu + \mathrm{i}\mathbf{s}_\nu \cdot (\mathbf{s}_1 \times \mathbf{s}_2)\right] \tag{1.42}$$

with

$$\rho = \left[2\left(1 + \mathbf{s}_\nu \cdot \mathbf{s}_1\right)\left(1 + \mathbf{s}_1 \cdot \mathbf{s}_2\right)\left(1 + \mathbf{s}_2 \cdot \mathbf{s}_\nu\right)\right]^{1/2} . \tag{1.43}$$

Similarly for $\Omega_{\nu,3,4}$. It is worth noticing that Berg and Lüscher [79] originally introduced a sign for the exponential in equation 1.42 but we assume the convention that triangles of spins are taken in the counter-clock wise direction, as Yin et al. mention in Ref. [80]. Moreover, this angle is not completely defined for the special configurations where $\mathbf{s}_\nu \cdot (\mathbf{s}_1 \times \mathbf{s}_2) = 0$ and $1 + \mathbf{s}_\nu \cdot \mathbf{s}_1 + \mathbf{s}_1 \cdot \mathbf{s}_2 + \mathbf{s}_2 \cdot \mathbf{s}_\nu < 0$. For these cases, the exponential falls in a branch cut in the complex plane [79, 80], which implies a change in the topological charge that can be related to the condition where a skyrmion is created or collapses.

The definition of the density charge only considers two triangles around a lattice site, missing the contribution from the other neighbours. However, this is necessary to avoid

[10] This derivation can be obtained from the definition of area $\Omega$ of a spherical triangle in a unit sphere $\Omega = A + B + C - \pi$, where $A$, $B$ and $C$ are the internal angles of the triangle [79]. $\Omega$ is also known as spherical *excess*.

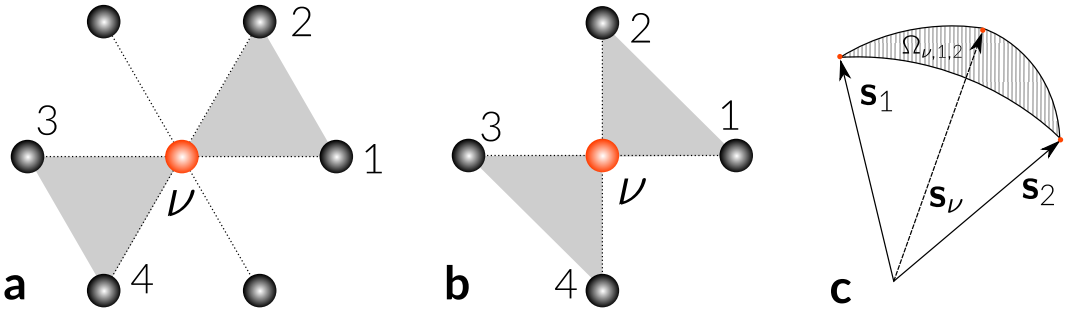


Figure 1.1

**Arrangement of neighbouring spins around a lattice site.** In (a) and (b), the coloured triangles indicate the positions of triplets of spins per lattice site $\nu$ that are used to define a topological charge in discrete hexagonal (a) and square (b) lattices. Numbering and labels are according to equation 1.41. In (c) we show the spherical triangle area $\Omega_{\nu,1,2}$ made by the triplet $(\mathbf{s}_\nu, \mathbf{s}_1, \mathbf{s}_2)$.

double counting when summing up all the contributions from the triangular areas. For a more complete picture of the topological charge per lattice site, we could take into account all the possible triplets of neighbouring spins per lattice site, for example, four triplets in the square lattice.

### 1.6.2. Skyrmion number

In the continuum limit, we use the concept of skyrmion number $Q_{\mathrm{SK}}$[11] to specify the topology of a magnetic configuration. Formally, it is described as

$$Q_{\mathrm{SK}} = \frac{1}{4\pi} \int_{\Omega} \mathrm{d}\Omega \, \mathbf{m} \cdot \frac{\partial \mathbf{m}}{\partial x} \times \frac{\partial \mathbf{m}}{\partial y} \tag{1.44}$$

with $\mathbf{m}$ as the normalised magnetisation and $\Omega$ as a two-dimensional area in the $xy$ plane, where the continuum magnetisation field is defined. For a full skyrmionic texture, where the magnetisation has a full twisting from $m_z = 1$ to $m_z = -1$ (or vicevversa), $Q_{\mathrm{SK}}$ is equal to 1 or -1, depending on the chirality of the structure. This number also indicates that it is possible to map and completely cover the vector field in $\Omega$ into a three dimensional sphere. When the skyrmion is incomplete or has extra twistings, $Q_{\mathrm{SK}}$ is normally less than one.

## 1.7. Skyrmions

In magnetism, skyrmions (SKs) are twisted particle-like structures[12] that are stabilised by different physical mechanisms [7]. The name *Skyrmion* has its origin in the works of the British physicist Tony Skyrme in quantum field theory [81], which was late applied to condensed matter systems such as nematic liquid crystals and magnetic solids [82]. One

[11] Also known as topological charge, winding number or quantum number [7].
[12] In the sense that they are localised in space, have quantised topological charges and undergo phase-transitions [8, 9, 19].

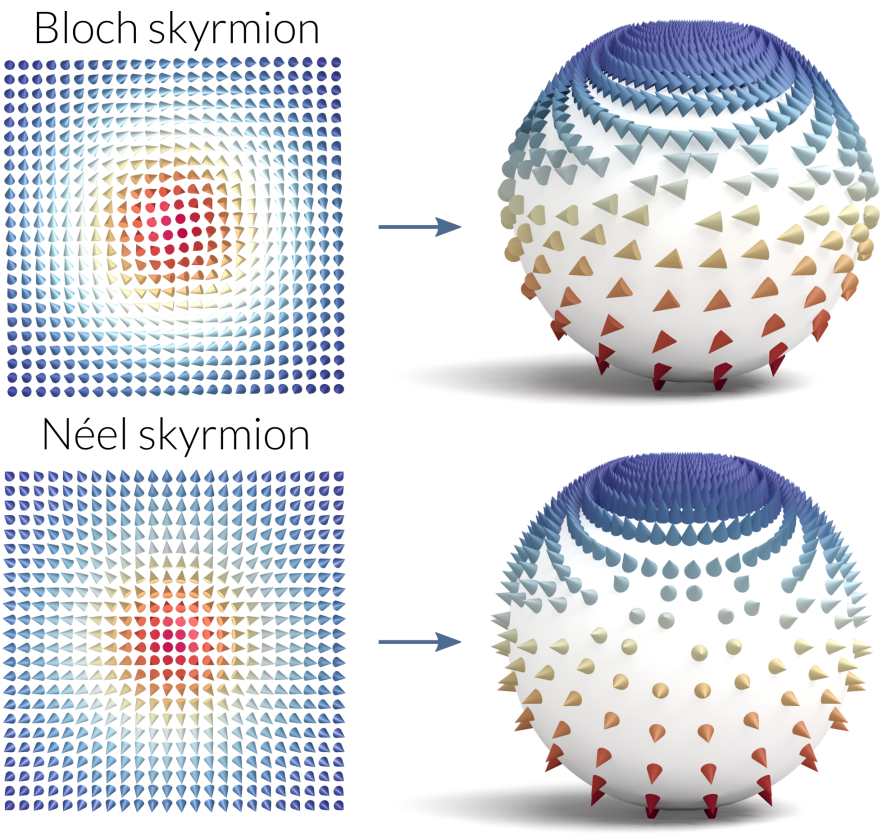


Figure 1.2 **Stereographic projection of skyrmions.** Mapping of the magnetisation or spin field of two kind of skyrmions into a sphere. Depending on the chirality given by the magnetic interactions in the material, we have skyrmions where the spin rotations resemble a Bloch or a Néel domain wall. In the stereographic projection of the skyrmion field, spins inside a circle where $m_z$ or $s_z \approx 0$ are mapped into the south hemisphere and spins outside this region are mapped into the north hemisphere. Both skyrmions have a skyrmion number or topological charge of $|Q| = 1$ since they wrap the whole sphere exactly once.

of the main stabilising mechanisms of magnetic skyrmionic textures are the Dzyaloshiskii-Moriya interactions, which are present in magnetic materials with a broken symmetry (see Section 1.4.4).

A magnetic skyrmion is distinguished by a spin field configuration where a localised core points perpendicular to the plane where it lies, and the magnetic moments around it are symmetrically arranged forming a chiral structure similar to a vortex. This arrangement depends on the nature of the DMI or the phenomenon stabilising the skyrmion. For systems where bulk DMI or an equivalent DMI expression is present, the spin rotations of a skyrmion resemble a Bloch type domain wall, as shown in Fig. 1.2. Similarly, in interfacial DMI or symmetry class $C_{nv}$ systems the spin twistings look like a Néel domain wall, which we also show in Fig. 1.2.

Skyrmionic structures are regarded as topologically protected particles, which means, in the words of Nagaosa and Tokura, that they "are characterised by a topological inte-

ger that cannot be changed by a continuous deformation of the field configuration" [7]. This property is valid for an infinite system but in confined samples the topological protection is non existent because a skyrmion can always be annihilated moving it across the boundary of the system. Nevertheless, it is still possible to define a topological charge (see Section 1.6) that constitutes a physical observable [83]. Moreover, in real systems the concept of topological protection is debatable since atoms are discrete by nature and the process of transforming a skyrmion will have associated a finite energy cost.

The skyrmion topology can be theoretically described using a measure of its whirling configuration, which is the skyrmion Number $Q_{SK}$ or topological charge $Q$ defined in Section 1.6. A skyrmion has associated $|Q_{SK}|$ or $|Q| = 1$ and this refers to how many times the spin field can be fully wrapped around a sphere when doing a mapping of the skyrmion field from the plane (see Fig. 1.2). Conversely, skyrmions that are incomplete or have more than one folding, have associated a smaller skyrmion number, *i.e.* $|Q_{SK}| < 1$. In a skyrmion lattice or when multiple skyrmions coexist, $Q_{SK}$ or $Q$ indicate the number of skyrmions present in the system ($|Q_{SK}| > 1$).

If we compute the topological numbers of the two skyrmions depicted in Fig. 1.2, both magnetic orderings have $Q_{SK}$ or $Q = -1$ because their core points in the $-z$ direction. Both of them are topologically equivalent because we can continuously transform the field of any of them by a $\pi/2$ rotation of the spins to get the other structure, which is consistent by having the same topological number. Furthermore, they are still topologically similar for opposite chiralities, *e.g.* spins of the Bloch skyrmion rotating counter clockwise or spins of the Néel skyrmion pointing inwards towards the centre. These magnetic orderings are topologically different from skyrmions of their same kind when spins at the skyrmion core point in the opposite direction, which means a positive unit topological number, and certainly from magnetic textures with different $Q_{SK}$ or $Q$ magnitudes, such as a ferromagnetic ordering which has zero topological number.

The topological number of a skyrmion is important when defining topological effects related to their structure. The twisted spin arrangement generates an emergent electromagnetic field whose mathematical description involves the topological number [7]. This emergent field affects electrons crossing through the skyrmion. For instance, a flow of electrons is deflected when crossing the skyrmion texture and this generates the known topological Hall effect, which has been measured experimentally [7]. In addition, when a skyrmion moves due to an electric current, it generates an emergent electric field, which produces a *Magnus* force, that drives the skyrmion in a direction transverse to the current direction. This is known as Skyrmion Hall effect [7, 84, 85]. Other spin-torque effects are known in skyrmionic textures, for example, a skyrmion can be manipulated using low current densities, though at lower speeds [7, 49, 86, 87] than domain walls. Ongoing research is trying to understand and tackle a variety of phenomena related to the current-induced motion of skyrmions [9].

Experimentally, skyrmions have been detected in several bulk [35–47] and interfacial [19, 50–59] materials by different methods (see Chapter 4). In particular, the internal structure of skyrmions has been resolved by Spin Polarised Scanning Tunnelling Microscopy [8, 19, 56] and the same technique has been used to create, delete or manipulate them [8, 56]. These topics are currently under extensive research.

Regarding skyrmion stability, it has been mentioned in analytical studies of infinite systems that helicoidal or conical states are usually the ones that have lower energy. The reason is that skyrmions have a gain in energy near the core region due to the exchange interaction, which can be modified by means of external magnetic fields or strong anisotropies [30,88]. Accordingly, large bias fields are required to stabilise hexagonally arranged skyrmion lattices and isolated skyrmions [88]. Through phase transition studies the skyrmion stability has been characterised by comparing the role of the intrinsic properties of the chiral structures, for instance, the double twisting of a skyrmion in two dimensions, with the energy of the system [30, 88, 89]. Additionally, near critical temperatures (where the system becomes paramagnetic), it has been observed that the skyrmion lattice formation is favoured. Here, thermal fluctuations contribute to the stabilisation of skyrmions in a small region of a temperature-field $T - H$ phase diagram, which has been corroborated experimentally [7, 35, 39, 42]. Nonetheless, for the materials studied in those experiments, such as MnSi, the $T - H$ diagrams indicate that the presence of an external magnetic field is always required for the stabilisation of a skyrmion, which is not optimal for technological applications. Recent works have reported the experimental observation of zero-field skyrmions in FeGe [90] and even at room temperature for thin interfacial systems [51, 55], which can lead to future works with detailed phase diagrams of skyrmions in these materials.

Further studies on skyrmion stability have proposed the study of skyrmionic orderings in confined structures [8, 51, 66, 86, 87, 91] such as nanodots or nanotracks. Interestingly, the border conditions in these systems help to the stabilisation of skyrmions in the absence of external magnetic fields or anisotropies, which is important for energy efficient applications.

Magnetic skyrmions are considered candidates for multiple spin based technological applications, *i.e.* spintronics. In Ref. [9] and [8], Fert et al. and Wiesendanger extensively review advances in skyrmion related research, different potential skyrmion based technologies and the current challenges in device engineering for their application.

### 1.7.1. An analytical study

Theoretical works about infinite magnetic samples that included DMIs, predicted axially symmetric solutions, specifically, meta stable magnetic vortex-like states with particular properties that could be potentially found in different classes of materials with broken symmetry [30]. These states resemble magnetic bubbles (a large core separated by a small domain wall from a uniformly magnetised background) under certain con-

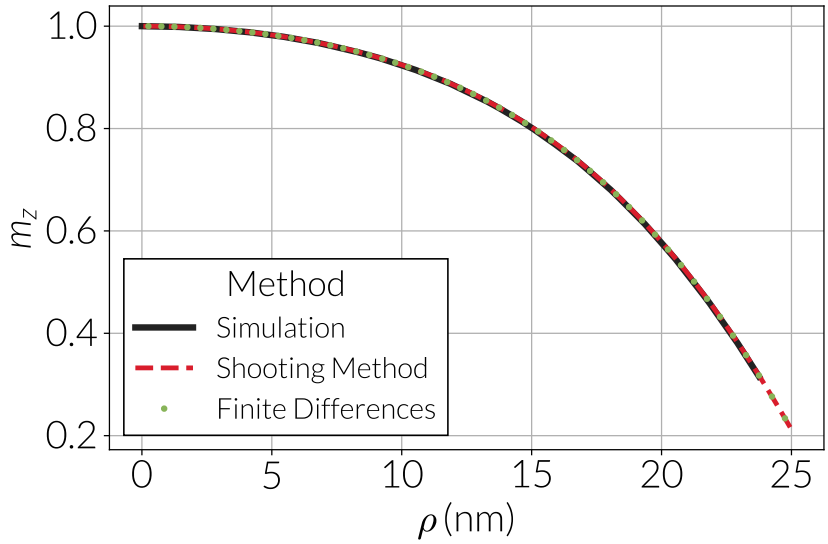


Figure 1.3

**Comparison of numerical solutions for an isolated skyrmion.** Comparison of different numerical methods against a finite elements simulation of a skyrmion in a two dimensional 50 nm wide FeGe nanodisk. The magnetic parameters of this system are: $A = 8.78\,\mathrm{pJ\,m^{-1}}$ for the exchange constant, $D_c = 1.58\,\mathrm{mJ\,m^{-2}}$ for the DMI and $M_s = 0.348\,\mathrm{MA\,m^{-1}}$ for the saturation magnetisation. Both numerical methods solve the differential equation 1.52 only considering DMI and exchange interactions.

ditions, however, bubble domains are unstable and they originate from dipolar interactions. Instead, in the micromagnetic limit the vortex-like states present topological stability and they have a defined chirality due to the DMI [9], thus they are now recognised as skyrmions [67]. In the following, we will present general analytical expressions in the continuum limit, to describe skyrmions in thin magnetic samples, including exchange, DMIs, Zeeman and anisotropic interactions. Accordingly, we need to compute the energy contributions from these interactions and minimise the total energy to obtain equilibrium solutions. As a particular solution, we will show that the only necessary mechanisms to stabilise a skyrmionic state in a finite system are the exchange interaction, the DMI and the boundary effects, which has been confirmed in Refs. [66, 91].

Using the continuum approximation mentioned in Section 1.4, the standard approach to describe a chiral system is to write $\mathbf{M}$ in spherical coordinates,

$$\mathbf{M} = M_s \left(\sin\theta\cos\psi, \sin\theta\sin\psi, \cos\theta\right) , \tag{1.45}$$

and the spatial variables as a function of cylindrical coordinates, *i.e.* $\theta = \theta(\rho, \varphi, z)$ and $\psi = \psi(\rho, \varphi, z)$. This formulation is suitable to describe axially symmetric solutions and the boundary conditions of a confined nanodisk. Because we are considering a thin sample, we will neglect the $z$ dependence in the spatial variables $\theta$ and $\psi$, which means a uniformity of the magnetisation along the $z$ direction. Starting with

the exchange interaction, we can compute the energy per unit volume $w_{ex}$ from equation 1.17 ($E_{ex} = \int dV\, w_{ex}$) by converting the gradients to cylindrical coordinates and using $\mathbf{m} = M_s^{-1}\mathbf{M}$ from 1.45, to obtain

$$\begin{aligned} w_{ex} &= A \sum_j \left[ \left(\partial_\rho m_j\right)^2 + \rho^{-2} \left(\partial_\varphi m_j\right)^2 + \left(\partial_z m_j\right)^2 \right] \\ &= A \left[ (\partial_\rho \theta)^2 + (\partial_\rho \psi)^2 \sin^2\theta + \rho^{-2} \left\{ (\partial_\varphi \theta)^2 + (\partial_\varphi \psi)^2 \sin^2\theta \right\} \right] , \end{aligned} \tag{1.46}$$

where $A$ is the exchange constant and $\partial_\rho = \frac{\partial}{\partial \rho}$ (similar for the other coordinates) and $j \in \{x, y, z\}$. Analogously, the DMI energy can be calculated both for a $T$ class material DMI and for the interfacial DMI cases. For the former, we use the closed form of the bulk DMI expression, equation 1.27, with the rotor in cylindrical coordinates, hence

$$\begin{aligned} w_{DM}^{(bulk)} &= D_c\, \mathbf{m} \cdot \boldsymbol{\nabla} \times \mathbf{m} \\ &= D_c \Big[ \sin(\psi - \varphi)\partial_\rho \theta + \sin\theta \cos\theta \cos(\psi - \varphi)\partial_\rho \psi \\ &\qquad - \rho^{-1} \cos(\psi - \varphi)\partial_\varphi \theta + \rho^{-1} \sin\theta \cos\theta \sin(\psi - \varphi)\partial_\varphi \psi \Big] , \end{aligned} \tag{1.47}$$

where $D_c$ is the DMI constant. For the interfacial case, equation 1.28, we must convert the partial derivatives from Cartesian to cylindrical coordinates to obtain

$$\begin{aligned} w_{DM}^{(int)} &= D_c \left( \mathcal{L}_{zx}^{(x)} + \mathcal{L}_{zy}^{(y)} \right) \\ &= D_c \Big[ \cos(\psi - \varphi)\partial_\rho \theta - \sin\theta \cos\theta \sin(\psi - \varphi)\partial_\rho \psi \\ &\qquad + \rho^{-1} \sin(\psi - \varphi)\partial_\varphi \theta + \rho^{-1} \sin\theta \cos\theta \cos(\psi - \varphi)\partial_\varphi \psi \Big] \end{aligned} \tag{1.48}$$

Including Zeeman interactions and anisotropies is straightforward. If we consider an out of plane magnetic field and out of plane uniaxial anisotropy with anisotropy constant $K > 0$, and apply equations 1.20 and 1.22, we have the following expression for their energy densities

$$\begin{aligned} w_{Zeeman} &= -\mu_0\, M_s H_z m_z = -M_s B_z \cos\theta \\ w_A &= -K\, m_z^2 = -K\, \cos^2\theta \end{aligned} \tag{1.49}$$

In a two dimensional system, the total energy is given by the sum of the interactions in the plane of the sample (for a three dimensional system, symmetric along the thickness $t$, we just multiply the expression by $t$)

$$E = \int d^2\mathbf{r}\, (w_{ex} + w_{DM} + w_{Zeeman} + w_A) \tag{1.50}$$

We can minimise the energy in different ways but under the same underlying principle:

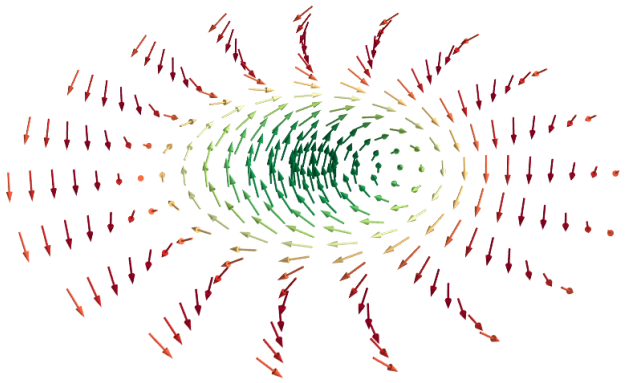

**Visualisation of a numerical solution for an isolated skyrmion.** Magnetisation field of a skyrmion in a 80 nm wide FeGe nanodisk, which has associated a bulk DMI. The field was obtained by solving equation 1.52 with the shooting method. The rotations of the spins for a skyrmion in this material resemble a Bloch domain wall. The border effects cause an extra curling of the magnetisation at the edges of the disk.

Figure 1.4

1. Using Brown's equation 1.40 [14], to get the magnetostatic configuration and the corresponding boundary conditions. In this case

$$\mathbf{H}_{\text{eff}} = -\frac{1}{\mu_0 M_s}\left(\hat{\psi}\frac{1}{\sin\theta}\frac{\delta}{\delta\psi} + \hat{\theta}\frac{\delta}{\delta\theta}\right) w \qquad \frac{\partial \mathbf{M}}{\partial n} = 0$$

   in which $\hat{n}$ is normal in the boundaries (in this case $\hat{n} = \hat{\rho}$) and $\mathbf{m} \times \hat{\theta} = \hat{\psi}$.

2. Performing a direct variation of the energy, that gives boundary conditions naturally:

$$\frac{\delta E}{\delta\psi(\varphi')} = 0 \qquad \frac{\delta E}{\delta\theta(\rho')} = 0$$

3. Similar to (ii), but using Euler's equation directly to variate the energy

$$\frac{\partial w}{\partial u} - \boldsymbol{\nabla}\cdot\frac{\partial w}{\partial(\boldsymbol{\nabla}\boldsymbol{u})} = 0 \qquad \hat{n}\cdot\frac{\partial w}{\partial(\boldsymbol{\nabla} u)} = 0$$

   where $u = \theta,\ \psi$

Furthermore, it is usually stated that, when minimising the energy through variational procedures, the system accepts axial symmetric solutions [28, 30, 67, 69, 88], *i.e.* $\psi = \psi(\varphi)$ and $\theta = \theta(\rho)$, which significantly simplifies the calculations. Indeed, if we perform the variation with respect to $\psi$, we agree that the symmetry accept those solutions, which lead to the description of skyrmions and helicoids. Nevertheless, it is also possible that the differential equations accept answers more complex than linear functions of $\psi(\varphi)$ if we assume appropriate initial conditions. This would allow us to obtain other chiral equilibrium states but making the equations significantly difficult to

solve, as can be seen in a study by Borisov and Rybakov [92], who performed an analytical study of spiral structures using numerical solutions of the variational equations for general $\theta(\rho, \varphi)$ and $\psi(\rho, \varphi)$.

For the particular crystal geometry of a bulk DMI solid, the axial function has solutions in the form $\psi = \varphi \pm \pi/2$, and an interfacial system accepts $\psi = \pm\varphi$. The choice of either sign defines the chirality of the system and for other materials the angle will have a different expression. Correspondingly, the structure of $\psi$ sets the ordering of the spins around the skyrmion core [28, 69, 88].

Using any of the afore mentioned methods to minimise the functional of equation 1.50 and reducing units using

$$\xi = \frac{A}{D_c} \qquad \tilde{\rho} = \xi^{-1}\rho \qquad b = \frac{AM_s B_z}{2D_c^2} \qquad \kappa = \frac{KA}{2D_c^2} \tag{1.51}$$

we obtain the differential equation

$$\partial_{\tilde{\rho}\tilde{\rho}}\theta + \tilde{\rho}^{-1}\partial_{\tilde{\rho}}\theta \mp 2\tilde{\rho}^{-2}\sin(2\theta) + \tilde{\rho}^{-1}\sin^2\theta - b\sin\theta - \kappa\sin(2\theta) = 0 \tag{1.52}$$

where the upper sign refers to a $T$ or $O$ crystallographic class DMI and the lower sign to an interfacial or $C_{nv}$ class DMI system.

For a finite cylindrical system, border conditions lead to the following restrictions

$$\theta(\tilde{\rho} = 0) = 0 \qquad \partial_{\tilde{\rho}}\theta(\tilde{\rho} = \xi^{-1}R) = -\frac{1}{2} \tag{1.53}$$

On the other hand, if we assume an isolated skyrmion in an infinite sample, the vortex structure can be stabilised considering uniaxial anistropy and/or an external magnetic field, imposing the direction of **m** in the centre and at infinity as

$$\theta(\tilde{\rho} = 0) = k\pi \qquad \theta(\tilde{\rho} = \infty) = 0 \tag{1.54}$$

where $k > 0$ is an integer that parametrizes the number of twistings or variations of the skyrmion. These solutions were named as $k\pi$-vortices by Bogdanov and Hubert [30].

Equation 1.53 can be solved using standard numerical methods. In this work we applied the Shooting Method and Finite Differences to compare numerical solutions versus a two dimensional simulation of a 50 nm wide FeGe nanodisk with bulk DMIs. These results are shown in Figure 1.3, where it can be seen a perfect agreement between the analytical theory and the simulation. Analogously, the magnetisation field of a full skyrmion was obtained using a 80 nm wide FeGe nanodisk, which is depicted in Figure 1.4.

We have not included dipolar interactions in this analytical model due to the non linearity of the equations, which makes the energy minimisation process unwieldy. In this regard, in a recent work Kiselev et al. [67] included the demagnetising field to the analytical model for an infinite film, using of an old theory about bubble domains [93]. They

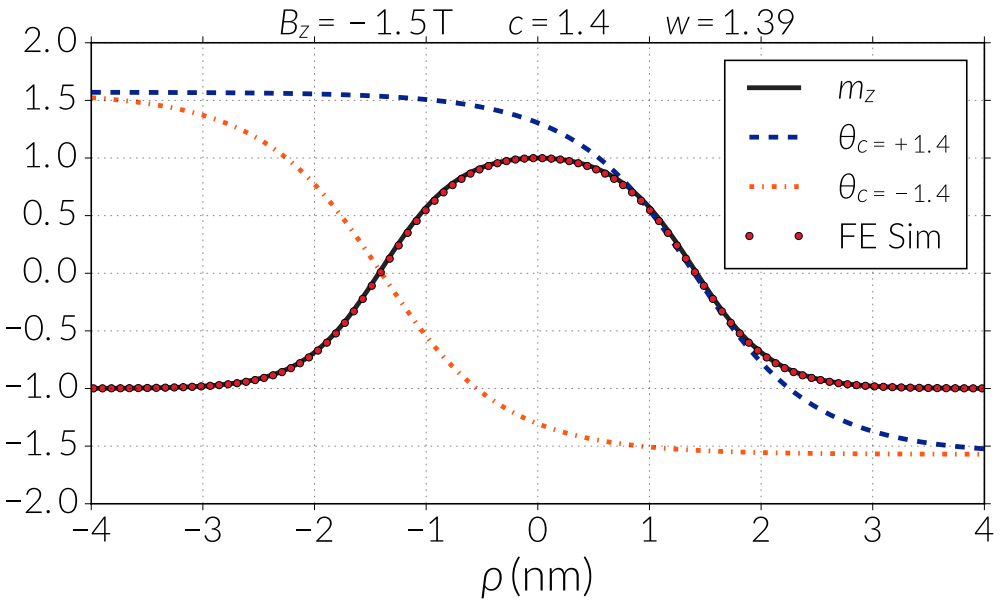


Figure 1.5

**Comparison of simulation and analytical model for an Néel skyrmion.** Out of plane component of the magnetisation field of a skyrmion in a Pd/Fe/Ir sample modelled as an infinite film. The skyrmion is described using an analytical model ($m_z$) and a finite elements simulation (FE Sim). The simulation was performed using periodic boundary conditions and a mesh discretisation of 0.1 nm. The analytical model is a superimposition of two Néel domain wall functions, which are shown as $\theta_c$ functions (see equation 1.55 for details), using the fit parameters from Fig. 2 of Ref. [58]. The skyrmion is stabilised using an out of plane bias field of $B_z = -1.5\,\mathrm{T}$ (in the $-\hat{\mathbf{z}}$ direction) of magnitude.

found isolated skyrmion solutions that are of interest in investigations about skyrmion dynamics in stripes under the influence of electrical currents [49, 86]. In addition, Guslienko [94] directly computed an expression for these interactions in a finite disk, finding vortex and skyrmionic states but without using DMIs, arguing that in a finite nanodot it is possible to stabilise those structures avoiding external fields or anisotropic exchange interactions. However, the nonlinear equations he obtained for the energy minimisation restricts him to compute the ground states using numerical methods or to assume a model for the magnetisation angle $\theta$.

Analytical solutions for the magnetisation field profile of a skyrmion, even in absence of dipolar interactions, are difficult to obtain due to the complexity of the governing differential equations that describe them. In this context, different mathematical functions for the skyrmion profile have been proposed to satisfy the energy minimisation equations [31, 58, 94]. In particular, Romming et al. used a superimposition of two $\pi$ domain wall profiles, since the skyrmion twistings resemble a Néel domain wall for a system with interfacial DMI. Regarding $w$ and $c$ as a $\pi$ domain wall width and position, the magnetisation angle $\theta$ proposed by Romming et al. [58], can be written as

$$\theta_{c,w}(\rho) = \arcsin\left(\tanh\left(\frac{-\rho + c}{w/2}\right)\right) + \arcsin\left(\tanh\left(\frac{-\rho - c}{w/2}\right)\right) \tag{1.55}$$

A comparison of this model with a skyrmion in an infinite PdFe over Ir sample is shown in Figure 1.5. Further details are described in Chapter 4.

## 1.8. Bloch Points in micromagnetism

According to the derivation of the continuum magnetism theory from the atomistic theory, it is assumed, at zero temperature, that the magnetisation is homogeneous and the field varies slowly. However, these assumptions become ambiguous if we accept the existence of singularities in the model, which was initially studied by Feldtkeller in 1965. These defects are known as Bloch points (or Feldtkeller singularities) and are characterised by the topological property that the magnetisation field vectors in a closed surface, *e.g.* a sphere around the singular point, will cover the surface of directions exactly once [95, 96]. Around a Bloch point, the magnetisation varies drastically, thus in the singularity the magnetisation is undefined and its length becomes zero, violating the micromagnetic hypothesis [95] (see Section 1.3). The description of a Bloch point using the continuum theory is not trivial, because it is necessary to consider appropriate boundary conditions around the surface that surrounds it and the condition that the magnetisation vanishes in the singularity. In this context, Feldtkeller firstly obtained an approximation of its energy, demonstrating that the Exchange energy was the leading interaction and, later, Döring corrected the result including the demagnetising field.

Multiple studies [96–99] have theoretically shown that Bloch points are present in the destruction and annihilation dynamics of vortex structures, and they have also been observed experimentally [96]. Moreover, modern computational techniques have allowed the simulation of vortex structures in thick magnetic samples, where the reversal mechanism of the vortex core is driven by a Bloch point moving across the thickness of the system. This has made possible to resolve the magnetisation field around these singularities. In their study, Thiaville et al. [96] provide three theoretically possible structures for a Bloch point, and a recent study by Elías and Verga [100] shows vortex and hedgehog Bloch point structures with different stability using a magnetic sphere. It is worth mentioning that these characterisations cannot fully describe a Bloch point defect since the continuum theory is undefined and in reality, materials are discretised by atomic spacings. The rapid variation of the magnetisation in the singularity suggest that it would be necessary to consider quantum effects to resolve the microscopic nature of the Bloch point dynamics [96, 100, 101].

According to the standard definition of a Bloch point, we notice that the description is intrinsically three dimensional. In our study, we will observe singularities in two dimensional samples, but we can still think about them as a Bloch points because, in theory, superimposing a vortex and anti vortex pair, each of them with the same charge, is topo-

logically equivalent to one of these three dimensional defects. Furthermore, we also observed a similar phenomenon when using a discrete spins lattice, but the definition of a Feldtkeller singularity in this case, is not completely understood because, firstly, the definition should still be valid since we keep assuming a constant length semi classical spin vector **S** in a discrete solid. However, the defect was defined as a continuum field singularity that would be better resolved with improved mesh resolutions, but it is not clear the validity below the atomistic constant, which is fixed for the discrete spin model. Besides these issues, the presence of a Bloch point is not catastrophic for these systems [102] since the energy is still finite.

# Nudged Elastic Band Method

Chapter 2



The Nudged Elastic Band Method (NEBM) is an algorithm that searches for minimum energy paths, *i.e.* transitions with minimum energy cost, between two equilibrium states of a system [11, 12, 103]. This technique was originally developed in the context of theoretical chemistry for the calculation of transition rates between two stable configurations of atoms from a system that can be described by a potential energy surface. The transition between these equilibrium states can be given, for example, by a chemical reaction or a diffusion process, where atoms change their configuration in the process [11, 12]. The NEBM is relevant for computing these transition rates because a minimum energy path is the preferred pathway of a system in its energy landscape. Along this path, the largest energy point is identified as a saddle point[1] in the potential energy surface, which sets the magnitude of an activation energy between the stable configurations. Accordingly, this energy can be used within harmonic transition state theory to estimate reaction rates [11, 12].

Because a magnetic system can be described by the free energy from the different magnetic interactions, it is natural to think that the NEBM can be adapted to describe paths of minimum energy cost between equilibrium states in magnetic materials. In this context, the activation energy would be seen as an energy barrier separating stable configurations that can be used to estimate their stability. First results of the NEBM applied to magnetic systems within the micromagnetic model were published by Dittrich et al. [104], computing minimum energy paths in a variety of simple magnetic systems, which corroborated with analytic theory. For example, they showed minimum energy transitions of small particles and elongated particles, where paths are characterised by coherent rotations and domain wall propagations, respectively. As availability of computational power increased, the method was later applied to larger systems [96, 105–107]. Due to the recent attention on skyrmions for spintronics applications and the open debate on the stability of these configurations, Bessarab et al. [13] published a review of the method with test examples based on chiral systems and using a discrete spin formalism. Furthermore, the review showed an optimised version of the NEBM, which includes geodesic distances in phase space and vector projections to improve the be-

[1] In complex energy surfaces it can exist more than one saddle point along a minimum energy path and the algorithm is also capable of finding other equilibrium states during the minimisation process. In this case, the highest energy saddle point is the one relevant for the estimation of the transition rate.

haviour of the algorithm. They claim that early versions of the method [96, 104, 105, 108] lead to uncontrolled behaviour of the algorithm. This publication has motivated new studies on the NEBM applied to skyrmionic textures [109–113].

In this chapter we give a general description of the algorithm.Consequently, we test the NEBM through different examples with varied degree of complexity. One of these test systems is a test model proposed by Bessarab et al. [13], which we analyse using a discrete spin model and micromagnetics.

Throughout this thesis we will refer to the algorithm simply as NEBM, instead of Geodesic NEBM as is usually done in the literature, since we will be using the optimised version of the method for every computation where it is involved.

## 2.1. The numerical method

To describe a magnetic material we use a discrete spin model, where we define a lattice of $P$ nodes which each have an associated three dimensional spin vector $\mathbf{s}_i$, with $i \in \{0, 1, \ldots, P-1\}$. Equivalently, if we describe a material micromagnetically, it is necessary to discretise the sample into a mesh of $P$ nodes, where every node $i$ represents the magnetisation field $\mathbf{m}_i$ evaluated at the node's coordinates $\mathbf{r}_i$, thus instead of discrete spins we use a discretised field $\mathbf{m}_i = \mathbf{m}(\mathbf{r}_i)$, $i \in \{0, 1, \ldots, P-1\}$. Henceforth, we will use discrete spins to describe the NEBM.

The whole system of spins $(\mathbf{s}_0, \mathbf{s}_1, \ldots, \mathbf{s}_{P-1})$ will be called an *image*, and we will denote it as $\mathbf{Y}$ (see for example the images defined in Section 2.4.1). The geometric ordering of the lattice that represents the arrangement of molecules or atoms, is given by crystallographic nature of the material. Depending on the magnetic configuration of the magnetic moments, an image will have a specific energy. Thus, the energy $E = E(\mathbf{Y})$ of the magnetic sample is parametrised by the magnetic ordering of $\mathbf{Y}$.

In the NEBM, we define a so called *band* of $N$ images $\mathbf{Y}_i$, $i \in \{0, 1, \ldots, N-1\}$, which are identical systems in (ideally) different magnetic configurations. For each of the images at either end of the band, $\mathbf{Y}_0$ and $\mathbf{Y}_{N-1}$, we fix the magnetic configuration to be the two equilibrium states for which we want to find the minimum energy transition. For the other $N-2$ images, $(\mathbf{Y}_1, \mathbf{Y}_2, \ldots, \mathbf{Y}_{N-2})$, we need to set up an initial sequence of magnetic configurations. A graphical representation of this set up is shown in Fig. 2.1 where the in-plane coordinates represent the two-dimensional phase space, every sphere $i$ represents a particular magnetic configuration $\mathbf{Y}_i$ in that phase space, and the surface represents the energy landscape $E(\mathbf{Y})$. In this figure, the equilibrium states lie in two global minima and the initial band (grey spheres) crosses an energy maximum (this energy landscape corresponds to the example defined in Section 2.4.1).

Keeping the images $\mathbf{Y}_0$ and $\mathbf{Y}_{N-1}$ fixed, we apply the NEBM algorithm, which iteratively evolves the band to find the lowest energy path between these two (see the minimum energy path in Fig. 2.1 that passes through a local minimum). This minimisation

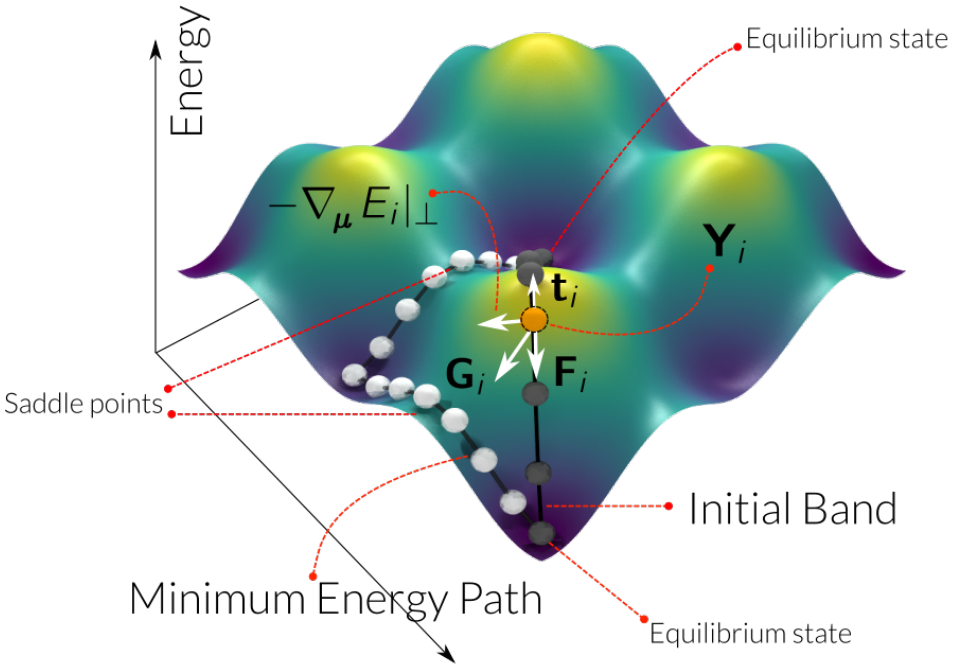


Figure 2.1

**Overview of the NEB method.** A summary of the Nudged Elastic Band method in a system parametrised by two variables. The surface height indicates the energy plotted for all points in this two-dimensional phase space. A set of specific magnetic configuration is shown through spheres, each being one image of the method. For a particular image $\mathbf{Y}_i$ of the initial energy band, we show the effective (total) force $\mathbf{G}$, the gradient component perpendicular to the band $\boldsymbol{\nabla}_{\boldsymbol{\mu}} E|_\perp$ ($\boldsymbol{\mu} = \mu\mathbf{s}$ as the magnetic moment), the tangent to the band $\mathbf{t}$ and the spring force $\mathbf{F}$. The height of the surface $E_i = E(\mathbf{Y}_i)$ shows the energy of image $i$. At the extrema of the band, the magnetic configurations are fixed and localised at energy minima.

is achieved by defining an effective force $\mathbf{G}$ for every image, which depends on vectors $\mathbf{t}$ that are tangents to the energy band. Additionally, since the energy of the band is minimised, the definition of $\mathbf{G}$ includes a spring force $\mathbf{F}$ between the images in order to keep them equally spaced in the phase space and avoid that the images cluster around the fixed states. Accordingly, to distinguish them, we use a Geodesic *distance* [13] which measures the difference of the spins direction between consecutive images (see Section 2.2.7). A minimum energy path is found when the component of the effective force $\mathbf{G}$ perpendicular to the band, *i.e.* perpendicular to $\mathbf{t}$, goes to zero (or the images only move along the band).

When the NEBM reaches convergence (see Section 2.3), the band will ideally pass through a maximum in energy along a single direction in phase space, which is known as a first order saddle point and it determines the energy barrier between the two fixed configurations. This transition path might not be unique and if it is the one with the smallest energy barrier, we call it the minimum energy path. For the final energy band

shown in Fig. 2.1, there are two maxima since the band crosses a metastable state that could be used as an equilibrium configuration, but we can clearly distinguish a single saddle point between every pair of energy minima. In that case the most relevant first order saddle point would be the one with largest energy, which is the barrier that the system needs to climb to get to the other equilibrium state. In general, there is no guarantee that any of the images in the band will sit exactly at the saddle point (commonly, there will be images to either side of the saddle point along the band), and thus the energy at the saddle point (and hence the energy barrier) is generally underestimated. To address this problem and improve the accuracy of the estimate, we can push one of the images into that maximum energy position along the path using a variation of the method called the Climbing Image NEBM [13, 114]. This is based on taking the largest energy point from a relaxed band (with the NEBM), redefine the forces applied to this image and then remove the spring force on it (see Methods for details). As a result, this image will try to climb up in energy along the band (while being allowed to decrease its energy in a direction perpendicular to the band).

## 2.2. Mathematical details

Basically, the algorithm of the NEBM can be summarised as the following steps:

1. Define a magnetic system and find two equilibrium states for which we want to find a minimum energy transition.

2. Set up a band of images and an initial sequence between the extrema. We can use, for example, linear interpolations on the spherical angles that define the spin directions, or Rodrigues' rotation formula on the spin orientations [13], to generate images between the extrema.

3. Evolve the system using a dynamical equation or a minimisation method for the NEBM, which depends on the chosen coordinate system. This equation involves:

    a) Compute the magnetic effective field **H** for every image of the band (images are in different magnetic configurations) and the total energy of every image

    b) Compute the tangent vectors **t** for every image, according to their energies and project them into the spin or magnetisation tangent space of the images

    c) Compute the total force **G** for every image in the band using the tangents and distances between neighbouring images. This requires the gradients (which use the previously calculated effective fields) and the spring forces on the images

    d) Project the total force into the spin or magnetisation tangent space of the images

e) Evolve the system using a dynamical equation or a minimisation method, according to the coordinate system, to zero the total force **G** or its component perpendicular to the tangent vectors **t**

f) Check convergence according to a specified criteria or go back to step 1.

Early versions of the NEBM did not involve to project the vectors into the tangent space in steps b and d. A proper mathematical definition and discussion about the tangent space is given by Bessarab et al. [13]. Their motivation for defining the tangent space is to unconstrain the NEBM, where the constraint is caused by condition of fixing the magnitude of the magnetic moments. A more detailed definition of this projection is provided in Section 2.2.8. Not projecting the vectors leads to an uncontrolled behaviour of the band evolution since the vectors that are supposed to be perpendicular to the band still have a component along the band which interferes with the images movement in phase space [13].

In the following we define the forces and the dynamical equation we use in the algorithm according to our chosen coordinate system.

### 2.2.1. Vectors

As we previously specified, an energy band $\mathbf{Y}$ consists of $N$ copies of a system which we call images, *i.e.*

$$\mathbf{Y} = (\mathbf{Y}_0, \mathbf{Y}_1, \ldots, \mathbf{Y}_{N-1}), \tag{2.1}$$

and every image $\mathbf{Y}_i$ is, ideally, a different magnetic configuration of the system. Each one of these images consists of $P$ spins

$$\mathbf{Y}_i = \left(\mathbf{s}_0^{(i)}, \mathbf{s}_1^{(i)}, \ldots, \mathbf{s}_{P-1}^{(i)}\right) \tag{2.2}$$

The spin vectors can be described in any suitable coordinate system. For our purposes, we will usually denote the spins in Cartesian coordinates, thus we can express the components of the $i$th image as

$$\mathbf{Y}_i = \left(s_{x,0}^{(i)}, s_{y,0}^{(i)}, s_{z,0}^{(i)}, s_{x,1}^{(i)}, \ldots, s_{x,P-1}^{(i)}\right) \tag{2.3}$$

We can see that in this coordinate system, the total number of degrees of freedom is $3P$. Furthermore, in the method we define vectors related to these images, for instance, we define an effective force $\mathbf{G}_i$ or tangent vectors $t_i$ for every image $\mathbf{Y}_i$. This means the effective force vector is expressed as

$$\mathbf{G} = (\mathbf{G}_0, \ldots, \mathbf{G}_{N-1})\,. \tag{2.4}$$

The vectors $\mathbf{G}_i$ will have the same number of components $P$ than the images $\mathbf{Y}_i$ in the chosen coordinate system, thus they will have the same structure than the images as

in equation 2.2. Correspondingly, for a general vector $\mathbf{A} = (\mathbf{A}_0, \ldots, \mathbf{A}_{N-1})$ related to the energy band $\mathbf{Y}$, each component $\mathbf{A}_i$ is associated to the $i$th image of the band. Therefore, using Cartesian coordinates, we can write every vector component $\mathbf{A}_j$ of $\mathbf{A}$ as

$$\mathbf{A}_j = \left(\mathbf{A}_0^{(j)}, \ldots \mathbf{A}_{P-1}^{(j)}\right) = \left(A_{x,0}^{(j)}, A_{y,0}^{(j)}, A_{z,0}^{(j)}, A_{x,1}^{(j)}, A_{y,1}^{(j)}, \ldots, A_{y,P-1}^{(j)}, A_{z,P-1}^{(j)}\right), \quad (2.5)$$

### 2.2.2. Tangents

In our implementation of the NEBM, we follow the rules of Henkelman and Jónsson [103] to compute the tangent vectors associated to every image of an energy band and, for the sake of completeness, we specify them here. These rules are related to the behaviour of the images near saddle points where, according to the energy $E$ of the neighbouring points, different possibilities can arise. Following the notation of Henkelman and Jónsson [103], we can define

$$\begin{aligned}
\mathbf{t}_i^+ &= \mathbf{Y}_{i+1} - \mathbf{Y}_i \\
\mathbf{t}_i^- &= \mathbf{Y}_i - \mathbf{Y}_{i-1} \\
\Delta E_i^{\max} &= \max\left(|E_{i+1} - E_i|,\ |E_i - E_{i-1}|\right) \\
\Delta E_i^{\min} &= \min\left(|E_{i+1} - E_i|,\ |E_i - E_{i-1}|\right)
\end{aligned}$$

According to this, the tangent of the $i$th image, $\mathbf{t}_i$ is:

$$\begin{aligned}
\mathbf{t}_i^+ \quad &\text{if} \quad E_{i+1} > E_i > E_{i-1} \\
\mathbf{t}_i^- \quad &\text{if} \quad E_{i+1} < E_i < E_{i-1}
\end{aligned} \quad (2.6)$$

Additionally, if $E_{i+1} < E_i > E_{i-1}$ or $E_{i+1} > E_i < E_{i-1}$, the tangent is defined as:

$$\begin{aligned}
\mathbf{t}_i^+ \Delta E_i^{\max} + \mathbf{t}_i^- \Delta E_i^{\min} \quad &\text{if} \quad E_{i+1} > E_{i-1} \\
\mathbf{t}_i^+ \Delta E_i^{\min} + \mathbf{t}_i^- \Delta E_i^{\max} \quad &\text{if} \quad E_{i+1} > E_{i-1}
\end{aligned} \quad (2.7)$$

Finally, we normalise these vectors, *i.e.* we set $\mathbf{t}_i \to \mathbf{t}_i/|\mathbf{t}_i|$.

### 2.2.3. Effective force

The effective force $\mathbf{G}$ for the NEBM relaxation is defined for every image, *i.e.* $\mathbf{G}(\mathbf{Y}_i) = \mathbf{G}_i$, and is a sum of a gradient force perpendicular[2] to the band plus a spring force parallel

[2] For a vector $\mathbf{A}$, the parallel and perpendicular component are defined with respect to the tangent vectors as: $\mathbf{A}|_\perp = \mathbf{A} - \mathbf{A}|_\parallel = \mathbf{A} - (\mathbf{A} \cdot \mathbf{t})\mathbf{t}$

to the band (see Ref. [103,104]). In the atomistic model we use the spin moment $\boldsymbol{\mu} = \mu\mathbf{s}$ to define the gradient force. In this case the effective force is expressed as

$$\begin{aligned}\mathbf{G}_i &= -\left\{\nabla_{\boldsymbol{\mu}} E(\mathbf{Y}_i) - \left[\nabla_{\boldsymbol{\mu}} E(\mathbf{Y}_i)\cdot\mathbf{t}_i\right]\mathbf{t}_i\right\} + \mathbf{F}(\mathbf{Y}_i)\\ &= -\left\{\nabla_{\boldsymbol{\mu}} E(\mathbf{Y}_i) - \nabla_{\boldsymbol{\mu}} E(\mathbf{Y}_i)|_{\parallel}\right\} + \mathbf{F}(\mathbf{Y}_i)\\ &= -\nabla_{\boldsymbol{\mu}} E(\mathbf{Y}_i)|_{\perp} + \mathbf{F}(\mathbf{Y}_i)\end{aligned} \tag{2.8}$$

and in the continuum limit, this expression turns into

$$\mathbf{G}_i = -\nabla_{\boldsymbol{M}} E(\mathbf{Y}_i)|_{\perp} + \mathbf{F}(\mathbf{Y}_i) \tag{2.9}$$

As specified in Ref. [13] and Section 2.2.8, to avoid misbehaviour of the band when the forces overlap, we must first project the tangents $\mathbf{t}$ in equation 2.8 or 2.9 into the tangent space and consequently project the effective forces $\mathbf{G}$.

Within the atomistic model, we can evaluate the gradient taking advantage of the effective field definition, which is related to the gradient of the energy with respect to the magnetic moment $\boldsymbol{\mu}$:

$$\nabla_{\boldsymbol{\mu}} E(\mathbf{Y}_i) = \frac{1}{\mu}\frac{\partial E}{\partial \mathbf{s}} = -\mathbf{H}_{\text{eff}}\,. \tag{2.10}$$

Similarly, in micromagnetics the gradient uses the magnetisation

$$\nabla_{\boldsymbol{M}} E \approx \frac{1}{M_s}\frac{\delta E}{\delta \mathbf{m}} = -\mathbf{H}_{\text{eff}} \tag{2.11}$$

The parallel component in the effective force means following the direction of a tangent vector $\mathbf{t}_i$ of an image $\mathbf{Y}_i$ which depends on the energy of its neighbours [103, 104].

### 2.2.4. Climbing Image NEBM

In the Climbing Image technique, we redefine the $\mathbf{G}$ vector for a single image (the climbing image) of the energy band, which is usually close to a saddle point, as [114]

$$\mathbf{G}_i^{\text{CI}} = -\nabla_{\boldsymbol{\mu}} E(\mathbf{Y}_i)|_{\perp} + \nabla_{\boldsymbol{\mu}} E(\mathbf{Y}_i)|_{\parallel}\,, \tag{2.12}$$

remembering to project the corresponding vectors as in Section 2.2.3.

### 2.2.5. Spring force

Since the energy of the band is minimised, it is necessary to set a spring force $\mathbf{F}$ between the images in order to keep them equally spaced in the phase space and avoid the clustering of images around the fixed states. Accordingly, the spring force is defined using the distance between neighbouring images

$$\mathbf{F}(\mathbf{Y}_i) = k\left(|\mathbf{Y}_{i+1} - \mathbf{Y}_i| - |\mathbf{Y}_i - \mathbf{Y}_{i-1}|\right)\mathbf{t}_i. \tag{2.13}$$

For an optimal behaviour of the algorithm, the images distances are defined by a Geodesic length using Vincenty's formulae [13].

Dittrich et al. [104] stated that their results did not require its application when using a variable order and time step method. In our study, the spring force has an influence in the results, affecting the number of iterations necessary for the algorithm converge and to achieve a better equispaced band. An estimation of the spring constant $k$ in equation 2.13 is difficult to compute, because it depends on many factors of the NEBM, such as the size of the system, number of spins, interactions involved and the coordinates system. We performed a series of tests to check optimal values for $k$, and it is usually in a range around $10^2$ to $10^5$. For larger order of magnitudes, the algorithm requires significant computation time, especially when using a small criteria for stopping the algorithm (see Section 2.3).

### 2.2.6. Initial condition

We describe the magnetisation using Cartesian coordinates, although any suitable coordinate system could also be used [13]. Our approach to determine the minimum energy band is to set an initial energy band using a linear interpolation of the spin angles between the fixed equilibrium images $\mathbf{Y}_0$ and $\mathbf{Y}_{N-1}$ in spherical coordinates, and then to evolve the band in the chosen Cartesian coordinates to find the minimum energy transition path between the fixed images. The advantages of using a Cartesian description of the spins is that the energy band is better defined when the spins directions are close to the poles but it is still necessary to constrain their length, which is fixed at zero temperature. While we discuss the initial energy band, we note that is also possible to manually specify an initial guess for the transition, usually by taking one or more images from a known path, for example the intermediate states when applying a spin polarised current between two equilibrium states.

#### 2.2.6.1. Linear interpolations

Using the standard definition for the magnetisation in spherical angles,

$$\mathbf{s} = (\sin\theta\cos\psi, \sin\theta\sin\psi, \cos\theta)\,, \tag{2.14}$$

the linearly interpolated initial state of the magnetisation is obtained through the angles of corresponding spins, between two different images, say $\mathbf{Y}_i$ and $\mathbf{Y}_k$ with $i < k$ (we usually use the extreme images, hence $i = 0$ and $k = N$). Thus, for every spin $j \in \{0, \ldots, P-1\}$ of the system, if we perform $n$ interpolations, the interpolated angles $(\theta_j^{(I)}, \psi_j^{(I)})$ of the image $\mathbf{Y}_I$, $I \in \{i, \ldots, k\}$, are

$$\begin{aligned}\theta_j^{(l)} =& \theta_j^{(i)} + \frac{l}{n+1}\left[\theta_j^{(k)} - \theta_j^{(i)}\right] \\ \psi_j^{(l)} =& \psi_j^{(i)} + \frac{l}{n+1}\left[\psi_j^{(k)} - \psi_j^{(i)}\right]\end{aligned} \tag{2.15}$$

### 2.2.7. Distances

There are different ways of defining the distance in phase space between two images, $d_{j,k} = |\mathbf{Y}_j - \mathbf{Y}_k|$. In the following sections we show three different cases. The most relevant are the Geodesic distances because according to the optimised version of the NEBM [13], the projection of vectors into the spin or magnetisation tangent spaces (see Section 2.2.8) implies that paths in energy landscape are now defined in curved spaces, where Geodesic distances are the optimal choice.

Regarding the figures with NEBM results, most of them have the abscissa defined as as the distance from the first image of the band $\mathbf{Y}_0$. This simply means summing up the distances from neighbouring images, *i.e.* the *i*th image in the band will be at a distance

$$d = \sum_{j=0}^{i-1} d_{j+1,j} = \sum_{j=0}^{i-1} \left|\mathbf{Y}_{j+1} - \mathbf{Y}_j\right| \tag{2.16}$$

from the first extreme of the band, which we measure in arbitrary units.

#### 2.2.7.1. Geodesic

The optimised version of the NEBM proposed by Bessarab et al. [13] considers a Geodesic distance based on Vicenty's formulae:

$$d_{j,k} = \sqrt{\left(\delta_0^{(j,k)}\right)^2 + \left(\delta_1^{(j,k)}\right)^2 + \ldots \left(\delta_{P-1}^{(j,k)}\right)^2} \tag{2.17}$$

where

$$\delta_i^{(j,k)} = \arctan 2\left(\left|\mathbf{s}_i^{(j)} \times \mathbf{s}_i^{(k)}\right|, \mathbf{s}_i^{(j)} \cdot \mathbf{s}_i^{(k)}\right) \tag{2.18}$$

This definition works better with the optimised NEBM [13] since spin directions are defined in a unit sphere where vectors are projected in order to be tangent to the spin spheres. This makes trajectories in energy landscape to be defined in curved spaces.

#### 2.2.7.2. Cartesian

The first versions of the method simply used an Euclidean distance based on the difference between corresponding spins. In Cartesian coordinates it reads

$$d_{j,k} = \frac{1}{3P}\left\{\sum_{j=0}^{P-1}\sum_{\alpha\in\{x,y,z\}}\left[\left(s_\alpha^{(j)} - s_\alpha^{(k)}\right)^2\right]\right\}^{1/2} \tag{2.19}$$

where we have scaled the distance by the number of degrees of freedom of the system (or an image).

#### 2.2.7.3. Spherical

In spherical coordinates, if we denote the spin components as

$$\mathbf{s} = (\sin\theta\cos\psi, \sin\theta\sin\psi, \cos\theta),$$

the definition is similar to the Euclidean norm:

$$|\mathbf{Y}_{i+1} - \mathbf{Y}_i| = \frac{1}{2P}\left\{\sum_{j=0}^{P-1}\left[\left(\psi_j^{(i+1)} - \psi_j^{(i)}\right)^2 + \left(\theta_j^{(i+1)} - \theta_j^{(i)}\right)^2\right]\right\}^{1/2}, \tag{2.20}$$

where $\left(\psi_j^{(i)}, \theta_j^{(i)}\right)$ is the pair of components of the $j$-th magnetic moment, $\mathbf{s}_j$, in the $i$-th image $\mathbf{Y}_i$. In this reference frame, there is one less degree of freedom, and it is implicit that the magnetisation length is constant. When using spherical coordinates, we avoid ambiguities in the $\psi$ angles differences $\Delta\psi = \psi_k^{(i)} - \psi_k^{(j)}$, by rescaling it to $2\pi - \Delta\psi$ when the difference is larger than $\pi$ (analogously if $\Delta\psi < -\pi$, in that case it is used $\Delta\psi + 2\pi$).

### 2.2.8. Projections

In Ref. [13] it is argued that since spin vectors can be characterised by two spherical angles (the length constraint becomes implicit), it is possible to define a two dimensional Riemannian sphere for every spin vector. Therefore, projecting a vector $\mathbf{A} = (\mathbf{A}_1, \ldots, \mathbf{A}_{P-1})$ into the spin or magnetisation tangent space of an image $\mathbf{Y}_i$, means that for every component $\mathbf{A}_j$ of the vector, we compute its component perpendicular to the corresponding $j$th spin vector $\mathbf{s}_j$ of this image. Mathematically, this is expressed as

$$\mathcal{P}_{\mathbf{s}_j}\mathbf{A}_j = \mathbf{A}_j - \left(\mathbf{A}_j \cdot \mathbf{s}_j\right)\mathbf{s}_j\,, \tag{2.21}$$

for $j \in \{0, \ldots, P-1\}$. As a result, the projected vector $\mathcal{P}_{\mathbf{s}_j}\mathbf{A}_j$ is tangent to the 2D-Riemannian sphere associated to $\mathbf{s}_j$ [13].

Hence, the total projection $\mathcal{P}$ into the spin or magnetisation tangent space is defined as

$$\mathcal{P}\mathbf{A} = \left(\mathcal{P}_{\mathbf{s}_0}\mathbf{A}_0, \mathcal{P}_{\mathbf{s}_1}\mathbf{A}_1, \ldots \mathcal{P}_{\mathbf{s}_1}\mathbf{A}_{P-1},\right)\,, \tag{2.22}$$

which in Cartesian coordinates can be expressed as

$$\mathcal{P}\mathbf{A} = (A_{x,0} - (\mathbf{A}_0 \cdot \mathbf{s}_0)s_{x,0}, \ldots, A_{z,P-1} - (\mathbf{A}_{P-1} \cdot \mathbf{s}_{P-1})s_{z,P-1})\,. \tag{2.23}$$

One of the steps of the steps of the NEBM, for example, involves calculating the vectors tangent to the band $\mathbf{t}$ for every image, thus $\mathbf{t} = (\mathbf{t}_0, \ldots, \mathbf{t}_{N-1})$ (remember that the energy band was defined with $N$ images). Notice that every tangent vector $\mathbf{t}_i$ is specified by tangents for every spin, *i.e.* $\mathbf{t}_i = (\mathbf{t}_0^{(i)}, \ldots, \mathbf{t}_{P-1}^{(i)})$. Therefore, *projecting* $\mathbf{t}$ into the tangent space of the energy band $\mathbf{Y}$, means projecting every vector $\mathbf{t}_i$ into the corresponding image $\mathbf{Y}_i$. This implies computing equation 2.22 with $\mathbf{t}_i$ instead of $\mathbf{A}$.

### 2.2.9. Relaxation of the bands

A minimum energy path for an energy band is found when the components of the effective force $\mathbf{G}$ perpendicular to the band are zeroed. This implies that images in the band only move along the band and the downhill energy minimisation, given by the gradient term in $\mathbf{G}$, is finished. An optimal path occurs when all the components of $\mathbf{G}$ are completely zero, which means that images are equally spaced along the band.

In our implementation of the method, the relaxations of the energy bands are achieved using a first order differential equation where every image is evolved with a fictional time $\tau$. In Cartesian coordinates we use a minimisation based on the Landau-Lifshitz-Gilbert equation, which has been used previously by Suess et al. [105]:

$$\frac{\partial \mathbf{Y}_i}{\partial \tau} = -\gamma\, \mathbf{Y}_i \times \mathbf{Y}_i \times \mathbf{G}_i + c\sqrt{\left(\frac{\partial \mathbf{Y}_i}{\partial \tau}\right)^2}\left(1 - \mathbf{Y}_i^2\right)\mathbf{Y}_i \tag{2.24}$$

In equation 2.24 the last term exists to constrain the length of the spins using a suitable factor $c$ and $\gamma$ is a factor in units of Hz $\mathrm{T}^{-1}$, which determines the time scale. This factor is irrelevant since we are using a artificial time parameter, thus we set $\gamma = 1$. The evolution of equation 2.24 will make the images to move in the direction of the effective forces $\mathbf{G}$ and thus follow a steepest descent path in the energy landscape, as occurs with the Landau-Lifshitz-Gilbert equation when removing the precessional term.

## 2.3. Implementation of the algorithm

We implemented this algorithm in our finite differences micromagnetics and atomistic simulations software Fidimag [78]. The interface of this code is written in Python and the main calculations are wrtitten in C code, connecting both languages through Cython. The integration of the NEBM dynamical equation is made with a library for stiff and non-stiff ordinary differential called CVODE which is part of a suite called Sundials [115]. Documentation about the code structure can be found in the Nudged Elastic Band Method section of Fidimag's documentation [116].

### 2.3.1. Convergence

We define the convergence of the NEBM as follows. We first calculate the norms of the difference (in corresponding degrees of freedom) between the energy bands of the last

computed NEBM step and the previously computed step. Consequently we scale them by the number of degrees of freedom (spins) per image. In Cartesian coordinates one of these norms is

$$\Delta \mathbf{Y}_i = \frac{1}{3P}\sqrt{\left(\mathbf{Y}_i^{(\mathrm{LAST})} - \mathbf{Y}_i^{(\mathrm{PREV})}\right)^2}, \tag{2.25}$$

where $i \in \{0, \ldots N-1\}$. We finally compute the maximum of these norms and divide by the last time discretisation $\Delta t$ given by the integrator [115]. Thus, we say the band converged if this value, $\max(\Delta \mathbf{Y}_i)/\Delta t$, is smaller than a specified criteria. We usually use values ranging from $10^{-1}$ down to $10^{-6}$.

## 2.4. Test systems

We have implemented the NEBM algorithm in our atomistic and finite differences software Fidimag [78]. Based on the examples proposed by Dittrich et al. [104] and the results of Bessarab et al. [13], we have analysed different test examples where the energy paths are known.

### 2.4.1. Two interacting particles

A simple model for testing the NEBM is a system where two particles of volume $V$ and separated by a distance $R$, have an uniaxial anisotropy easy axis oriented perpendicular (or parallel) to a line connecting their centre and which are only coupled via dipolar interactions. We describe the spins assuming that the spins rotate in a single plane, thus we can characterise the system by two angles $(\theta_1, \theta_2)$, as show by the inset to the right of Fig. 2.26. Accordingly, we can formulate an analytical description of the system's energy assuming macrospins as in the Stoner-Wohlfart model obtaining

$$\frac{E(\theta_1, \theta_2)}{K_\mathrm{u} V} = \sin^2\theta_1 + \sin^2\theta_2 + \left(\frac{\mu_0}{4\pi}\frac{V M_\mathrm{s}^2}{2K_\mathrm{u}R^3}\right)(\sin\theta_1 \sin\theta_2 - 2\cos\theta_1\cos\theta_2), \tag{2.26}$$

where $K_\mathrm{u}$ is the anisotropy constant and $M_\mathrm{s}$ the saturation magnetisation. In this system the global minima are the two configurations where both particles point in the same direction along the anisotropy axis, and metastable states appear when they point in opposite directions along the anisotropy axis. A full picture of the energy landscape for this two particle model can be seen from Fig. 2.1.

We simulate this system using our micromagnetics code by setting two cubic cells of 3 nm side, separated by a distance of $R = 6$ nm. We use standard material parameters of $K_\mathrm{u} = 1.5\,\mathrm{MJm}^{-3}$ and $M_\mathrm{s} = 3.8 \times 10^5\,\mathrm{Am}^{-1}$.

For the NEBM, the initial state is specified as a coherent rotation of the spins from one equilibrium state towards the other. After evolving the system with the NEBM the algorithm found the minimum energy path where one spin rotates first and then

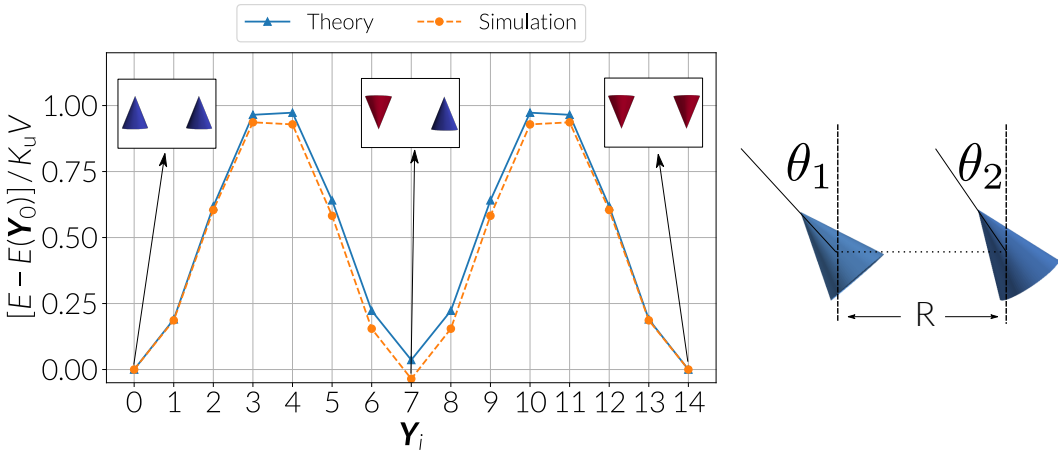


Figure 2.2

**Reversal of two anisotropic macrospins.** Minimum energy path of two particles separated by a distance $R$ where an uniaxial anisotropy easy axis oriented perpendicular to a line crossing their centres. A model of this system is shown in the right image, where it is assumed that the particles rotate in the same plane, thus the minima occur when both $(\theta_1, \theta_2)$ are 0 or $\pi$. The particles interact only via dipolar interactions. The energy path is an asynchronous rotation of the spins. The $x$-axis refers to the image numbers. The energy is shifted with respect to the energy of the first image and rescaled by a factor. The theory curve is given by equation 2.26.

the other spin rotates until the system reaches the other global minimum. In this asynchronous rotation, there is a local minimum where spins point in opposite directions, *i.e.* $(\theta_1, \theta_2) = (\pi, \pi/2)$, generating two energetically degenerate saddle points in the energy path. This can be seen from Fig. 2.2, where we compare the energies of the images in the band with the analytical equation 2.26, taking the angles from the simulation and shifting the energy scale with respect to the first image energy. Here we clearly observe the two saddle points before and after a metastable state, which set the energy barrier magnitude for the particles reversal transition, and where it is evident a good agreement with the analytical model. Small insets in the plot indicate the magnetic configurations of the corresponding images.

### 2.4.2. Elongated particle

A more complex test system, with a larger number of degrees of freedom, is an elongated particle with an uniaxial anisotropy along its main axis, thus two global minima are identified when all the spins point along the two possible orientations along the easy axis.

As in the two particles example, we use micromagnetics to describe this system. We set up a cuboid of 12 nm × 12 nm × 70 nm, discretised by cubic cells of 2 nm side. The initial state for the NEBM is specified again by a coherent rotation of the spins from one anisotropic direction towards the opposite one. The minimum energy path in this

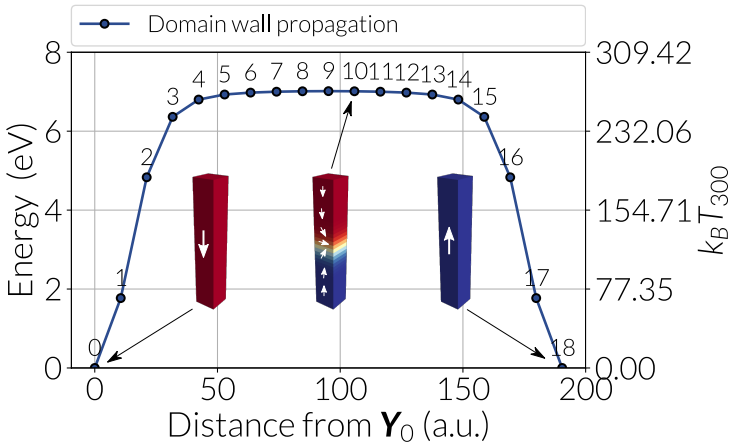


Figure 2.3 **Magnetisation reversal of an elongated particle.** Minimum energy path of an elongated particle with uniaxial anisotropy oriented along the particle's long axis. The minimum energy transition is given by the nucleation, propagation and destruction of a transverse domain wall, moving across the system's main axis. Small insets depict snapshots of specific images of the energy band. The energy is shifted with respect to the equilibrium states energy.

case is a domain wall propagation triggered at one of the extremes of the particle. This domain wall travels along the particle's long axis and reverses the spins behind it until completing the particle magnetisation reversal, which is the other global minimum. We chose a cuboid geometry for simplicity but a cylindrical shape can be used to compare the results with a full analytical model [117, 118].

We show in Fig. 2.3 the result of the NEBM applied to this system, where the minimum energy transition is given by the magnetisation reversal mediated by a domain wall. The figure also shows snapshots of the corresponding images in the energy band, where we notice that between the 5th and the 13th image, the energy does not change. This means that any state given by the domain wall positioned inside the long particle is degenerate in energy, and the total energy only changes when the domain wall is nucleated or destroyed at any of the extremes. For this case, the energy barrier is around 7 eV.

### 2.4.3. Skyrmion based NEBM test model

Bessarab et al. [13] proposed a toy model to simulate a skyrmion on a discrete spin lattice in order to test the NEBM. This test model considers a system of 21 by 21 spins with periodic boundary conditions. The model Hamiltonian reads

$$\mathscr{H} = -J\sum_{\langle i,j\rangle}^{N} \mathbf{s}_i \cdot \mathbf{s}_j - D\sum_{\langle i,j\rangle}^{N} \left(\mathbf{r}_{ij}\times\hat{\mathbf{z}}\right)\cdot\left[\mathbf{s}_i\times\mathbf{s}_j\right] - \mu\sum_{i}^{N}\mathbf{B}\cdot\mathbf{s}_i \tag{2.27}$$

which has the convention $\langle i,j\rangle$ in the sums, indicating a summation over every spin pair

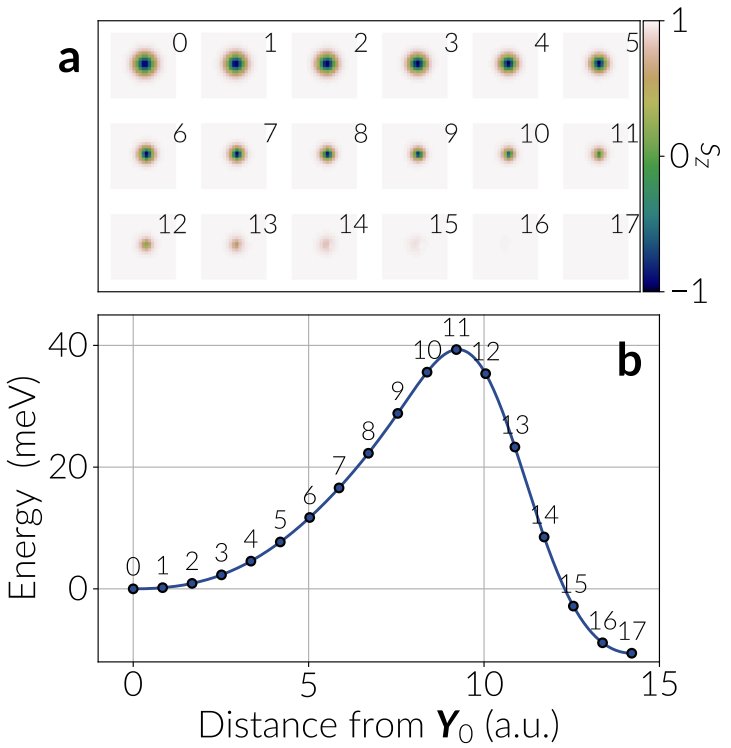


**Skyrmion collapse.** Minimum energy path of a skyrmion in a 21 by 21 spins system arranged in a two dimensional square lattice with periodic boundary conditions. (a) Images of the energy band depicted in (b), colourised according to the out of plane component of the spin orientations. The numbering is according to the labels of (b). (b) Energy band curve for the skyrmion annihilation. The energy is shifted with respect to the skyrmion energy.

Figure 2.4

without repetition. The magnetic parameters are: an exchange constant of $J = 10$ meV, an interfacial DMI constant of $D = 66$ meV, a magnetic moment of $\mu = 2\mu_B$ and an out of plane magnetic field of 25 T. The ground state of the system is a ferromagnetic ordering along the magnetic field. A skyrmion with a hedgehog-like profile and its core pointing in the opposite direction of the field is stabilised as a metastable configuration. The uniform ordering and the skyrmion are shown as the 0th and 17th images, respectively, in Fig. 2.4 and 2.5.

Fixing the two equilibrium states at the extrema of a band, we initialise the band using linear interpolations between them and evolve the system with the NEBM. The result is shown in Fig. 2.4, where a barrier of 39.03 meV, with respect to the skyrmion energy, was found after a reasonable number of NEBM iterations. This magnitude is in agreement with the approximate value of 40 meV obtained in Ref. [13]. The resulting transition is the skyrmion annihilation by collapse and a sequence showing the spin field for this process is provided in Fig. 2.5, where the three images correspond to the skyrmion, the saddle point and the uniform ordering of the energy path shown in Fig. 2.4.

This test model can be reproduced using the code from the repository in Ref. [119].

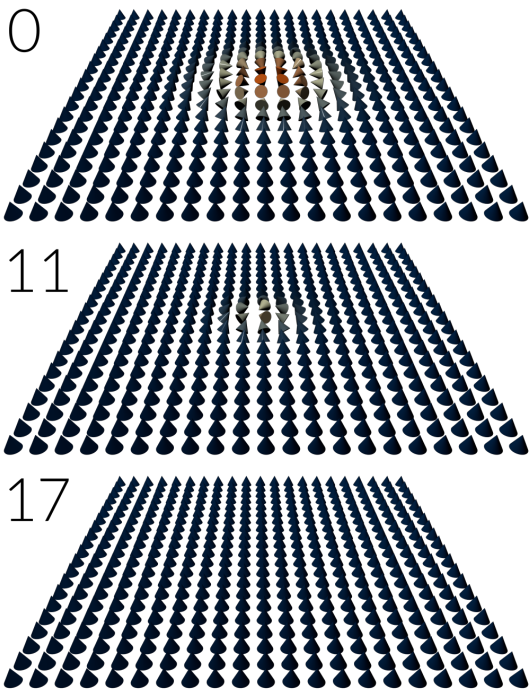


Figure 2.5 **Skyrmion collapse.** This sequence shows the annihilation of a skyrmion via a collapse which is obtained from the test system of the NEBM specified in Section 2.4.3. Each snapshot is an image of the energy band of Fig. 2.4 hence the numbering goes according to the labels on the curve of Fig. 2.4b. In the sequence we recognise the two equilibrium states, a skyrmion and the uniform ordering as the 0th and 17th image, respectively, and the saddle point of the energy path, given by the 11th image.

### 2.4.4. NEBM test model in the continuum

Initial studies of the stability of magnetic systems based on the NEBM analysed materials in the micromagnetic limit. The NEBM works for continuum systems because numerically it is necessary to discretise the material, and thus the fields from the magnetic interactions, into a mesh, making it possible to directly apply the algorithm. In principle, improving the numerical discretisation of the material, which is done by reducing the mesh spacings, should give a better approximation of the system. However, when topological singularities are present the energy depends on the discretisation. For example, in Ref. [96] Thiaville et al. apply the NEBM to analyse the reversal of magnetic vortexes by the propagation of Bloch points and they find that the mesh discretisation has an influence of the energy barrier magnitudes. The structure of a skyrmion is similar to a magnetic vortex configuration thus we are interested in observing if a similar phenomenon occurs for the minimum energy paths relevant to a skyrmion.

We apply the NEBM to the test system of Section 2.4.3 in the continuum limit and using a 20 nm by 20 nm two dimensional mesh. For the simulations we use finite differences and we assume a cubic lattice with a lattice constant of $a = 5$ Å. Accordingly,

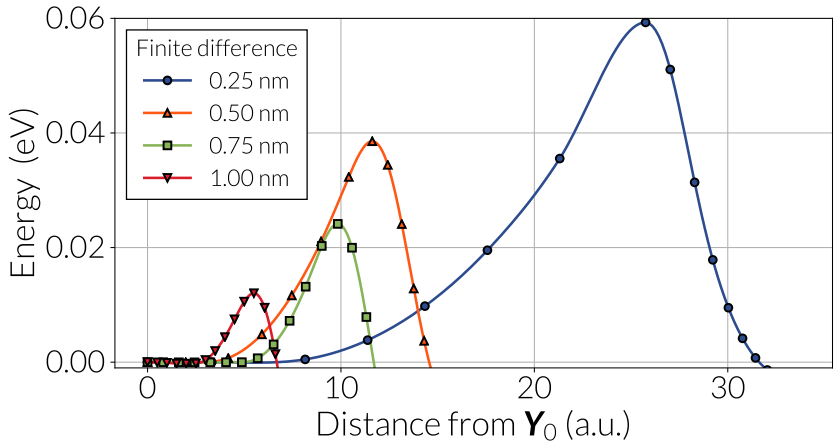


Figure 2.6

**Effect of the mesh discretisation on the energy barriers in the continuum.** The curves are energy bands of the skyrmion-uniform ordering transition. The system is the same as the one specified in Section 2.4.3 but in the micromagnetic limit and using a 20 nm × 20 nm square mesh. Different cases refer to different spacings between mesh nodes for the finite differences discretisation. For the conversion of atomistic parameters into micromagnetic parameters it is assumed a lattice constant of 5Å and the same value is used for the thickness.

the magnitude of the magnetic parameters under this model are (see Appendix D): a exchange constant of $A = 3.204\,\mathrm{pJ\,m^{-1}}$, a DMI (interfacial) constant of $D = 3.84\,\mathrm{mJ\,m^{-2}}$, a saturation magnetisation of $M_s = 148367\,\mathrm{A\,m^{-1}}$ and the magnetic field of 25 T to stabilise the skyrmionic configuration. We specify different mesh discretisations, *i.e.* different spacings between mesh nodes, from 0.25 nm (80 × 80 magnetic moments) up to 1.0 nm (20 × 20 magnetic moments) in steps of 0.25 nm. Setting the NEBM simulation between a skyrmion and the ferromagnetic state as in Section 2.4.3, we relaxed every case with the algorithm (improving the position of the point near the saddle point with the climbing image NEBM) and plot the resulting energy bands in Fig. 2.6, where the bands describe the collapse of a skyrmion. Energy values are shown with respect to the skyrmion energy and rescaled using the corresponding lattice thickness $a_z = a$ in every curve. We notice that using a mesh spacing equal to the atomic spacing of 0.50 nm, given by the curve with upward triangles in Fig. 2.6, we recover the result of Section 2.4.3, where the energy barrier is around 39 meV. The tendency for the other curves is evident, reducing the mesh discretisation the energy barrier is larger and using coarser meshes the energy barriers are smaller. The saddle points of every band, given by the images with largest energy in Fig. 2.6, refer to the point in the skyrmion collapse process where only a few spins of the skyrmion core remain before reversal (see the 11th image of Fig. 2.5 as a reference). At this stage it is clear that the skyrmion core behaves like a singularity since reverting these spins has a large energy cost and violates the assumption in micromagnetics of a smooth change in the magnetisation field. This situation must be derived from the non-trivial topology of the skyrmion, in partic-

ular within the micromagnetic limit where a topological protection of this structure is meaningful. The increasing energy magnitudes with smaller mesh spacings can be justified mathematically by observing that when discretising the derivatives of the exchange and DMI energy in the continuum, these terms are proportional to the inverse of the finite difference size (mesh discretisation). These issues tell us that a continuum model for this kind of transition is not optimal. A better description that avoids the discretisation dependency would be using the discrete spin model but large systems in this model would require long computation times.

# Skyrmions in Cobalt systems

Chapter 3



In 2013, Sampaio et al. [86] published a theoretical study about generating skyrmions in Cobalt disks with interfacial DMI using localised spin polarised currents in the middle of the magnetic sample. Furthermore, it was shown that small density currents in narrow stripes can move skyrmions, allowing a new method to write and erase data in an energy efficient nano sized memory device. Following experimental works studying cobalt based samples, in particular stacked multilayered systems, have successfully identified the presence of skyrmions in these materials and, lately, have been focused on stabilising sub 100 nm skyrmions, enhancing the DMI magnitude in the material and generating skyrmions using electric currents, among other effects [9, 50–52, 54, 55, 120].

The concept of skyrmions as data units in an information recording device is analogous to the racetrack memory technology which is based on domain walls [121], but in a skyrmion-based racetrack memory design the information bit 0 or 1 would be encoded by a skyrmion's presence or absence. Correspondingly, an important parameter that needs to be understood is their thermal stability. Specifically, it is necessary to know the average lifetime that a skyrmion will remain stable close to room temperatures, since this information provides the time scale over which data can be stored in the device without corruption.

To analyse the stability of skyrmions, and hence verify if these chiral structures are suitable for information recording, we calculate the energy barriers associated with their mechanisms of destruction and creation in thin ferromagnetic nanotracks with interfacial DMIs. Although we select a cobalt system because of its relevance as a material that can host skyrmions when combined with a heavy metal (see Section 1.4.4 for the DMI origin at the interface of a ferromagnet and a heavy metal), our results are applicable to a variety of interfacial DMI based materials since we analyse these systems in a range of DMI strengths and thus skyrmion sizes. The energy barrier calculations are achieved through the Nudged Elastic Band Method (NEBM) which gives us the minimum energy transitions between the equilibrium states in these skyrmionic systems. Furthermore, the methods shown in this chapter can be extended to magnetic solids with different DMI mechanisms and different geometries.

In Section 3.1 we start describing the magnetic properties of Cobalt systems with interfacial DMI using the discrete spin and micromagnetic theories. Consequently, we discuss the role of the demagnetising field when considering a thin geometry, its influ-

| Constant | Unit | Hexagonal (c) | Hexagonal | Square |
|---|---|---|---|---|
| $a$ | Å | 2.5 | 2.5 | 2.5 |
| $a_z$ | Å | 2.5 | 4 | 4 |
| $J_{ij}$ | meV | 27.026 | 43.24 | 74.90 |
| $\mu_s$ | $\mu_B$ | 0.846 | 1.35 | 1.56 |
| $D_{ij}$ | meV | 0.676 | 1.08 | 1.87 |
| $\mathcal{K}_u$ | meV | 0.0676 | 0.108 | 0.125 |
| $A$ | pJ | 15.0 | | |
| $M_s$ | MA m$^{-1}$ | 0.58 | | |
| $D$ | mJ m$^{-2}$ | 3 | | |
| $K_u$ | MJ m$^{-3}$ | 2.5 | | |
| thickness | nm | 0.4 | | |

Table 3.1 **Magnetic parameters of a Cobalt based magnetic system.** The micromagnetic values, at the bottom of the table, are taken from the theoretical work of Sampaio et al. [86]. The crystal lattice of Cobalt has an hexagonal geometry and atomistic parameters are provided at the second and third column. The second column refers to the parameters when *correcting* the atomic spacing to 2.5 Å instead of the 4 Å assumed for the monolayer in [86]. The last column are the atomistic values if we assume a simple square crystal for the lattice arrangement, which is unrealistic but useful for testing simulations.

ence on a skyrmion configuration and a discrepancy in skyrmion dimensions between the continuum and discrete models. These results will show us that it is necessary to make some corrections to the atomistic parameters to keep an agreement in skyrmion sizes in both theoretical frameworks. Finally, in the next sections we perform a thorough study of the NEBM applied to skyrmion to ferromagnetic (or vice versa) transitions to compute energy barriers of isolated skyrmions in cobalt stripes. These results are obtained using the discrete spin model, and have been published in Ref. [1].

## 3.1. Material characterisation

In reference [86] Sampaio et al. proposed two mono-layered Cobalt systems: a nano sized disk and 40 nm wide nanotracks. Based on them, we will use the following geometries in our analysis:

- An 80 nm wide and 0.4 nm thick disk
- An 80 nm long, 40 nm wide and 0.4 nm or 0.25 nm thick stripe

Both systems have an interfacial DMI whose magnitude we vary and a strong uniaxial out of plane anisotropy. The DMI in a Co based system can be obtained by stacking the cobalt above a heavy metal with a strong spin orbit coupling. Experimental techniques

have been proposed to tune the DMI magnitude by sandwiching the magnetic sample between two different metallic layers that induce interfacial DMIs of opposite symmetry, generating Dzyaloshinskii vectors in the same direction and thus a large DMI [9, 50, 53]. At the time of publication of Ref. [86], there was no experimental evidence of the Co samples under study, thus the magnetic parameters are based on standard Co material. The magnitudes of the parameters in the continuum formalism are specified in Ref. [86], where the sample thickness is assumed as $a_z = 4$ Å and the discretisation of the mesh is set to 1 nm for finite differences. However, we will show in the corresponding section that the skyrmion destruction mechanisms cannot be optimally described within micromagnetics thus we use the discrete spin formalism for the NEBM calculations.

The atomic arrangement of an FCC cobalt layer has an hexagonal structure [63, 86, 109]. We assume a lattice constant of $a = 2.5$ Å and, because we are considering a Co monolayer, the atomic layer spacing should be assumed as $a_z = 4$ Å. However, the demagnetising field causes skyrmions in the micromagnetic model to differ in size than when they are simulated using the atomistic model (see Section 3.3), thus to make the atomistic results comparable to the micromagnetic ones [86], we will assume atomistic lattice distances with equal magnitudes along the plane and layer thickness, *i.e.* $a = a_z = 2.5$ Å (rather than $a_z = 4$ Å), obtaining good agreement in skyrmion dimensions between the discrete and continuum models.

The micromagnetic and atomistic parameters are summarised in Table 3.1 for a specific DMI constant value (we will vary this parameter). The Co lattice is hexagonal by nature but for testing purposes we will also assume a square lattice. We show material values for both geometries in Table 3.1. Additionally, we specify the parameters for the hexagonal lattice when using the original inter layer spacing of $a_z = 4$ Å, which is depicted in the Hexagonal column, and when using the corrected atomic spacing of $a_z = 2.5$ Å, shown in the Hexagonal(c) column.

### 3.1.1. Interfacial DMI

In the continuum, the interfacial DMI can be theoretically described by the energy density in terms of two Lifshitz invariants. Following the formalism of Rohart and Thiaville [66] the invariants are defined with an opposite chirality [86]:

$$w_{\text{DM}} = -D_{\text{c}} \left( \mathcal{L}_{xz}^{(x)} + \mathcal{L}_{yz}^{(y)} \right), \tag{3.1}$$

where $D_{\text{c}} > 0$ is the DMI constant. This changes the skyrmion twisting orientation, compared with the one found in systems such as PdFe over Ir. In the atomistic model, the DMI vector equivalent to this Lifshitz invariant is written as [63] $\mathbf{D}_{ij} = D\hat{\mathbf{z}} \times \hat{\mathbf{r}}_{ij}$. The relation between the DMI constants in both models is given in Appendix D.

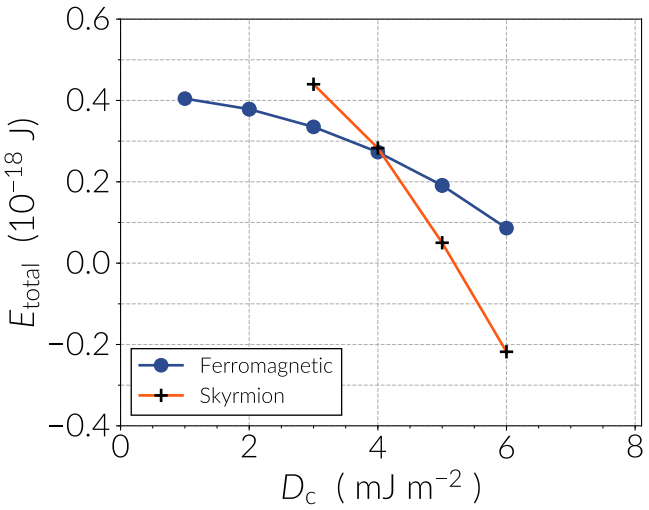


Figure 3.1

**Energy as a function of DMI magnitude for two stable states in a nanodisk.** The sample is specified as a 80 nm wide and 0.4 nm thick Co disk with interfacial DMI. The disk is relaxed with either a skyrmion or a uniform state, which are known stable configurations in this system. The energy of these magnetic structures vary according to the strength of the DMI constant $D_c$ and they change from being metastable to a ground state (if no other chiral configuration has lower energy). The system was simulated in the continuum framework using finite elements of 1.2 nm edge length in average.

### 3.1.2. Equilibrium states

Including the strong anisotropy and the confined geometry, the interfacial DMI in a Co layer favours the stabilisation of chiral structures. In general, we observe four well defined equilibrium states, within the range of DMI magnitudes we study. Two of them are Néel skyrmions with the core pointing up or down with respect to the out of plane ($z$) direction (see top of Fig. 3.2b) and that are degenerate in energy. Similarly, the two other are degenerate ferromagnetic orderings pointing perpendicular to the nanotrack plane (see bottom of Fig. 3.2b), with a small canting at the boundary of the system. We obtained these states by relaxing similar configurations using the Landau-Lifshitz-Gilbert equation. However, we cannot guarantee that these are the only equilibrium configurations since, depending on the $D_c$ or $D$ value, other chiral orderings can arise but they cannot be easily identified. Generally, knowing the true global minima of a specific system is not straightforward, but we will focus on the four aforementioned magnetic states.

In Fig. 3.1 we compare the energies of the skyrmion and ferromagnetic states in Co disks, using our finite element code. In the simulations we take into account the exchange, DMI, uniaxial anisotropy and demagnetising fields, thus the total field is

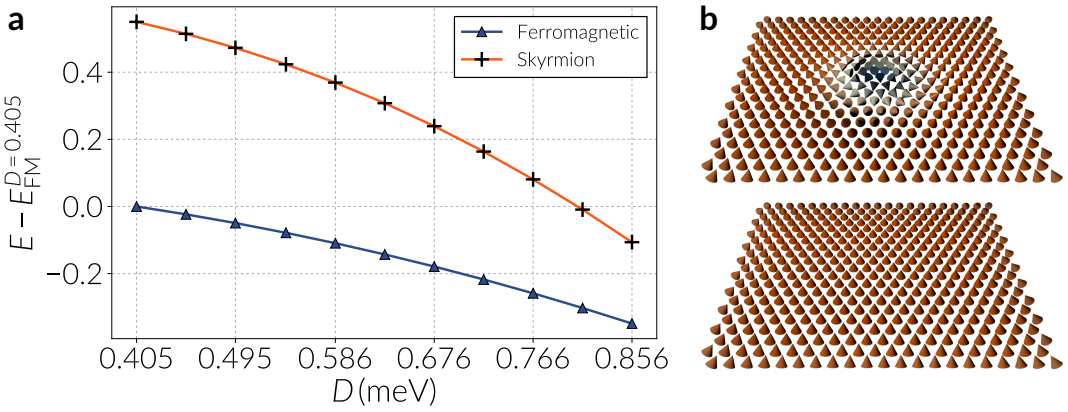


**Energy as a function of DMI magnitude for two stable states in a nanotrack.** The system is defined using a discrete spin model and consists of a Co monolayer made up of 320 × 185 atoms, making a stripe of 80 nm length and 40 nm width. The lattice constants are specified as $a = a_z = 2.5$ Å. The energy scale is shifted with respect to the energy of the uniform state with a DMI constant of 0.405 meV. As in the case of nanodisks, a skyrmion and a uniform ordering are stable states in this stripe system. (a) Energy curves with respect to DMI strength for the two equilibrium states. (b) Snapshots of these configurations in a smaller monolayer.

Figure 3.2

$$E = \int_{V_{\mathrm{disk}}} \mathrm{d}V \left\{ A \sum_{\alpha,\beta \in \{x,y,z\}} \left(\partial_\alpha m_\beta\right)^2 + D_{\mathrm{c}} \left[\mathcal{L}_{zx}^{(x)} + \mathcal{L}_{zy}^{(y)}\right] - K_{\mathrm{u}} (\mathbf{m} \cdot \hat{z})^2 - \frac{\mu_0}{2} \mathbf{M} \cdot \mathbf{H}_{\mathrm{d}} \right\} \quad (3.2)$$

where $V_{\mathrm{disk}}$ is the volume of the disk and $\mathbf{H}_{\mathrm{d}}$ the demagnetising field (see Section 1.4.5). After numerically minimising the energy we see our results agree with Figure 1a in [86], where they use a finite difference approach. Furthermore, over a value of $D_{\mathrm{c}} = 4\,\mathrm{mJ\,m^{-2}}$ the skyrmion changes from being a metastable state (local minimum of $E$) to a regime where its energy is lower than the ferromagnetic state thus is more preferred as a stable state for the system and is likely to be the global minimum, although this DMI value is large compared to experimentally determined values in Co.

A different geometry is the nanotrack which we analyse in detail in Section 3.4. We simulate this system using a discrete spin model with the Hamiltonian

$$\begin{aligned} \mathscr{H} = &- J \sum_{\langle i,j \rangle}^{P} \mathbf{s}_i \cdot \mathbf{s}_j + D \sum_{\langle i,j \rangle}^{P} \left(\hat{\mathbf{z}} \times \mathbf{r}_{ij}\right) \cdot \left[\mathbf{s}_i \times \mathbf{s}_j\right] - \sum_{i}^{P} \mathcal{K}_{\mathrm{u}} \left(\mathbf{s}_i \cdot \hat{\mathbf{z}}\right)^2 \\ &+ \frac{\mu_0 \mu^2}{4\pi} \sum_{\langle i,j \rangle}^{P} \left[ \frac{\mathbf{s}_i \cdot \mathbf{s}_j}{r_{ij}^3} - \frac{3 \left(\mathbf{s}_i \cdot \hat{\mathbf{r}}_{ij}\right) \left(\mathbf{s}_j \cdot \hat{\mathbf{r}}_{ij}\right)}{r_{ij}^5} \right] \end{aligned} \quad (3.3)$$

in a hexagonal lattice of $P = 320 \times 185$ spins. In Fig. 3.2a we summarise the energies of the skyrmion and uniform state as a function of the DMI strength. Snapshots of these configurations are provided in Fig. 3.2b. To match the skyrmion dimensions from micro-

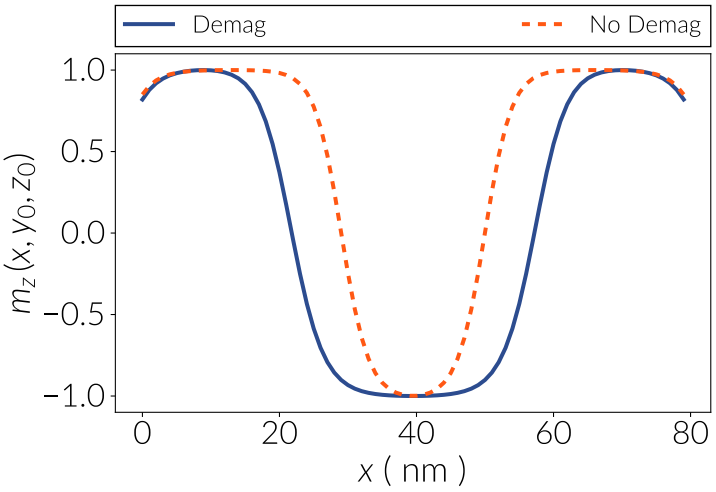


Figure 3.3 **Demagnetising field effect on a skyrmion in a nanodisk.** The image shows the out of plane ($z$) component of the magnetisation profile across the diameter of a 80 nm wide and 0.4 nm thick Co disk. The system was specified with a DMI constant $D$ of 4 mJ m$^{-2}$. Different curves show the magnetisation when considering or not considering the stray field. This magnetic configuration was obtained using finite differences (OOMMF).

magnetic simulations the atomic spacing along the thickness is set to $a_z = 2.5$ Å, hence the range of DMI magnitudes depicted in Fig. 3.2, where the data is given in steps of 0.045 meV, is equivalent to the continuum DMI constants from 1.8 up to 3.6 mJ m$^{-2}$ in steps of 0.2 mJ m$^{-2}$. We see that the ferromagnetic ordering is the global minimum on this whole range, which agrees with the nanodisk energies of Fig. 3.1, and the skyrmion remains as a metastable state, *i.e.* as a local minimum in the energy landscape given by the energy 3.3.

## 3.2. Demagnetising field effects

In Section 3.1 of this Chapter we defined how skyrmions are stabilised in Co disks considering all possible magnetic interactions in the model. In this regard, Sampaio et al. [86] argue that the demagnetising field has a negligible influence on their systems, in particular for a nanodisk. However, we have observed that dipolar interactions help to stabilise skyrmionic textures in similar systems [91], and from the large size of the structures we are considering in this study, which are around 80 nm in length, we believe that dipolar interactions must have a noticeable effect. We must have present that the systems (nanodisk or nanotrack) we are analysing are only a few monolayers thick thus we are in the limit of an ultrathin film. It has been claimed in the literature that in this limit the energy from dipolar interactions is significantly small compared to other energy terms, especially for skyrmions [69, 110, 112]. Moreover, in this limit the demagnetising field can be approximated as an uniaxial anisotropy term [112], especially for cylindrically

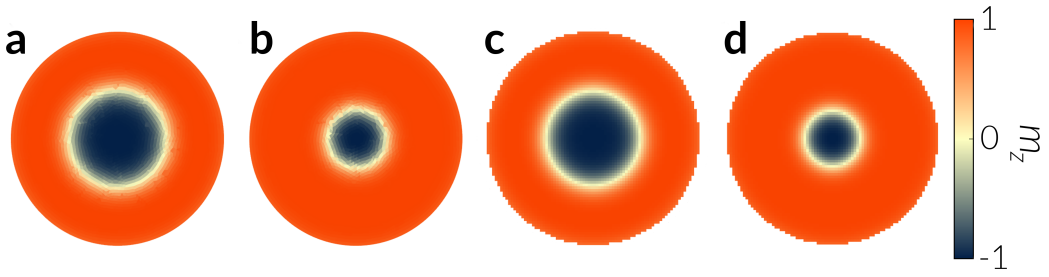


Figure 3.4

**Effect of the demagnetising field on the skyrmion size.** Snapshots of nanodisks hosting a skyrmion. The system specifications are the same than those of Fig. 3.3. Images are different according to the presence or absence of the demagnetising field, and the numerical method. Cases (a) and (b) refer to finite elements (Finmag) with and without dipolar interactions, respectively. Cases (c) and (d) are similar, but using finite differences (Fidimag). Images are coloured according to the out of plane component of the magnetisation.

symmetric structures such as Néel skyrmions [30, 69]. Accordingly, it would be necessary to know the magnitude of the effective anisotropy to compensate the effect of the demagnetising field, which is not always found in the literature for different materials and an analytical approach is too complex to estimate it, in particular when treating with non-colinear magnetic configurations. In our case, numerical simulations allow us to compute the contribution of the dipolar interactions thus we consider its full expression in our calculations. In the following we will attempt to elucidate the effects of the stray field on skyrmions.

To substantiate our claims about the effects of the demagnetising field we reproduced the micromagnetic simulations performed by Sampaio et al. [86] using the same numerical method (finite differences) and material parameters, both with and without inclusion of the demagnetising field. Interestingly, we found that the skyrmion has a smaller size when dipolar interactions are not considered. This has an important influence in the NEBM since a small skyrmion is more confined inside the disk, *i.e.*further away from the boundaries. Therefore, it presents a similar behaviour to a system with a smaller DMI magnitude where the skyrmion can avoid more effectively the annihilation mechanism through a boundary. Conversely, when the demagnetising field is present, the skyrmion is wider.

In Fig. 3.3 we plot the $z$ component of the magnetisation profile along the diameter of a 80 nm wide disk (see caption for parameters details), *i.e.* fixing the $y$ and $z$ coordinates at the centre of the sample. Simulations were performed using Fidimag [78] both with and without dipolar effects. According to this figure, we can clearly see that, with respect to the case without dipolar effects, the skyrmion core, where $m_z = -1$, significantly expands under the influence of the demagnetising field, decreasing the region where $m_z = 1$ close to the boundary (this is also evident from Fig. 3.4a and d).

| Case | Energy ( $10^{-19}$ J ) | Energy ( eV ) |
|---|---|---|
| Finmag (2 layers) - Demag | 2.82 | 1.766 |
| Finmag (2 layers) - No Demag | -0.496 | -0.310 |
| Finmag (1 layer) - No Demag | -0.512 | -0.400 |
| Fidimag (1 layer) - Demag | 2.93 | 1.832 |
| Fidimag (1 layer) - No Demag | -0.424 | -0.265 |
| Fidimag (2 layers) - Demag | 2.93 | 1.832 |
| OOMMF (1 layer) - Demag | 2.93 | 1.832 |
| OOMMF (1 layer) - No Demag | -0.424 | -0.265 |

Table 3.2 **Effect of the demagnetising field on the energy of a skyrmion in a nanodisk.** Total magnetic energy of a skyrmion in 80 nm wide and 0.4 nm thick Co disks with DMI constant $D_c = 4\,\mathrm{mJ\,m^{-2}}$, both when considering (Demag) and not considering (No Demag) dipolar interactions. Simulations were performed using finite elements (Finmag) and finite differences (Fidimag and OOMMF). The mesh discretisation was specified using one or two layers along the thickness.

We can understand this effect by depicting the dipolar field as a shape anisotropy (our system is thin enough), which makes a hard axis perpendicular to the disk plane, favouring the alignment of the spins with the disk plane. At first glance, it seems that it occurs the contrary effect since there is a larger section of spins perpendicular to the plane around the skyrmion core. Nonetheless, the region of spins with in plane components has moved up to approximately 30 nm away from the centre, as shown by the continuous curve in Fig. 3.3 (see Fig. 3.4a and d), covering a larger area of the system and therefore, effectively increasing the number of spins with components parallel to the disk plane. Although the magnetisation profile with non-zero in-plane components does not change drastically, we must bear in mind that there are other effects present because the demagnetising energy is competing against the Dzyaloshinskii-Moriya, exchange and anisotropic interactions, and the boundary effects.

To further clarify the magnetisation field change under the influence of dipolar interactions, we show in Fig. 3.4 the nanodisks with a colour map according to the $m_z$ component of the spins and using both Finmag [77] and Fidimag [78]. Besides the difference in the numerical techniques of the simulation softwares, we confirm in this plot the equivalence between both methods (finite elements and finite differences), although the energies are slightly different. Accordingly, in Table 3.2 we summarise the results of the simulations for the nanodisk used in Fig. 3.3 and 3.4, where units are provided in electron volts (eV). Referring to Fig. 3.4, we see that Finmag has a much better approximation to the curved boundary, therefore the energy differences (because of the demagnetising field) of corresponding simulations in Table 3.2 are more accurate than the magnitudes obtained with the finite difference solvers. On the other hand, Finmag does not have the capability to compute the demagnetising field when using a single layer (it is in fact

a two dimensional simulation that we scale to the real system multiplying the obtained energy by the sample thickness) but we can see that there is not a considerable contrast with the other results if we focus on the values in Joule units. To compare the effect of the number of layers used for the mesh discretisation, on the global energy of the system, we also show in Table 3.2 the energies when using 1 or 2 layers. In the finite differences code the layers are symmetrically arranged on top of each other whereas using finite elements the entities are not symmetrically stacked but are also ordered in two levels.

## 3.3. Disagreement between atomistic and continuum simulations

For materials with interfacial DMI it is possible to approximately convert the magnetic parameters from the continuum to the atomistic model, or vice versa, due to the simplicity of the crystal lattice geometry. It is expected that both theoretical frameworks describe equivalent magnetic structures, although this might depend on the assumptions made when deriving the parameters. The most realistic comparison between the models could be achieved by obtaining an analytical solution for an equilibrium configuration of the system of interest, through a quantum mechanical formalism. However, this is a non trivial problem for systems with hundreds of spins and, even in the semi classical approximation we use, to calculate a closed form function for a stable configuration is impossible. Numerical simulations, on the contrary,facilitate the computation of stable solutions for different systems, which allow us to analyse the properties of magnetic configurations obtained with both theoretical models.

In our comparison, we analyse skyrmion sizes in thin Co nanotracks when considering or removing dipolar interactions from the sample, using different computational techniques. These Co stripes are the systems we analyse in detail in Section 3.4. The system is made of a single layer of Co whose magnetic parameters are specified in Table 3.1. We choose a DMI constant of 3 mJ $m^{-2}$ thus a skyrmion appears as a meta-stable state after relaxation. For the atomistic case we implemented hexagonal (the real lattice geometry) and square lattice (for testing purposes) simulations in Fidimag [78], using an atomic spacing along the thickness of $a_z = 4$ Å. We used finite elements [77] and finite differences [78] to get the micromagnetic solutions. The outcomes of the simulations are summarised in Fig. 3.5.

When considering the stray field in the sample, the two atomistic simulations agree in skyrmion size, as expected, and the same occurs between the micromagnetic results. However, referring to Fig. 3.5a, there is a discrepancy between the discrete and continuum skyrmion profiles. Contrarily, when turning off dipolar interactions, as shown in Fig. 3.5b, all the models relaxed a skyrmion of similar size (we only show the atomistic simulation with hexagonal lattice and the micromagnetic simulation with finite differ-

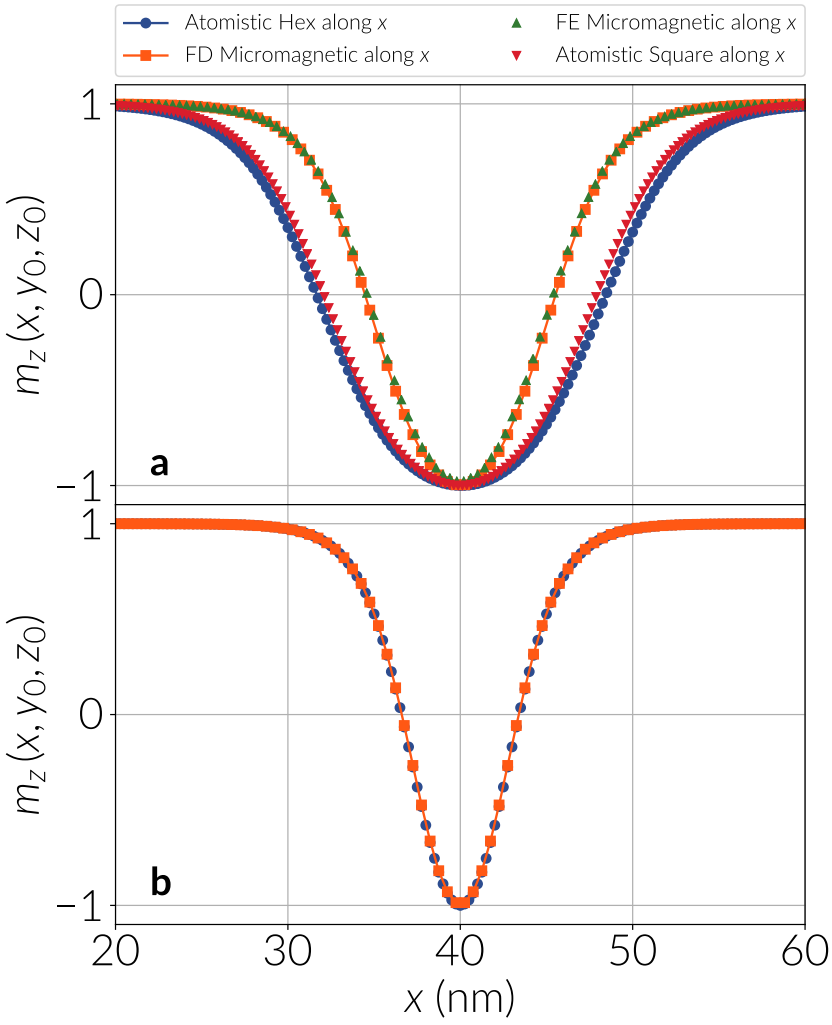


Figure 3.5 **Comparison of skyrmion sizes for atomistic and micromagnetic simulations.** The curves show the out of plane magnetic components of a skyrmion in a Co nanodisk with a DMI constant of $D_c = 3\text{mJ m}^{-2}$, obtained using different simulation techniques. The micromagnetic simulations were specified using finite elements (FE) and finite differences (FD). The atomistic simulations are based on hexagonal (Hex) and square lattices with parameters converted from the continuum using lattice constants of $a = 2.5$ Å and $a_z = 4$ Å (see Table 3.1). The convention to estimate the skyrmion size is to calculate the distance between points were $m_z = 0$ along a line passing through the skyrmion centre, which is located at $(x_0, y_0, z_0)$. (a) Simulations with demagnetising field. (b) Simulations without considering demagnetising field.

ences), indicating that the problem lies in the demagnetising field.

In the case of the discrete spin model, a larger skyrmion size could indicate that dipolar interactions are stronger in this model, since they act as an easy plane anisotropy in a thin film. Furthermore, a careful look into the derivation of the stray field in the continuum model, starting from the discrete model rather than using Maxwell's equations directly, could shed a light into this phenomenon. Specifically, if we refer to Brown [122] or Aharoni [14], an approximation of the dipolar field is achieved taking Lorentz's argu-

ment about considering a *physically* small sphere around every lattice site. This means that the sphere must be small enough so inside it the magnetisation $\mathbf{M}$ is constant or at most changes linearly from one site of the grid to a neighbouring one. The spatial scale where $\mathbf{M}$ changes can be measured through the exchange length, since it gives an idea of the domain wall widths in the material. Additionally, the sphere must be larger than the lattice constant of the material. Therefore, the slowly varying magnetisation inside the sphere allows us to compute the dipolar field considering the magnetisation as a continuum field outside the sphere, *i.e.* we can use Maxwell's equations for the field, say $\mathbf{H}_{\text{out}}$, outside this region, simplifying the computation of the dipolar field contribution of discrete spins to be only inside the sphere, $\mathbf{h}_{\text{in}}$. Summing up, the field of a lattice site $i$ would be

$$\mathbf{H}_i = \mathbf{H}_{\text{out}} + \mathbf{h}_{\text{in}}. \tag{3.4}$$

To calculate $\mathbf{H}_{\text{out}}$, we consider the total continuum dipolar field $\mathbf{H}_{\text{total}}$ and subtract the continuum contribution inside the sphere, $\mathbf{H}_{\text{in}}$, where $\mathbf{M}$ is assumed constant or linear in space. For a sphere in a bulk sample the field inside it is given by

$$\mathbf{H}_{\text{in}} = -\frac{4\pi}{3}\mathbf{M}, \tag{3.5}$$

and is the one used by Brown [122] and Aharoni [14]. However, if we decrease one of the sample dimensions down to a few monolayers, which is the case of interest in our study, the sphere argument is no longer valid since there would be no material in a region of this geometrical construction. For this case, we could probably use a cylinder and if $\mathbf{M}$ is constant or linear, this field term could still be proportional to the magnetisation. This would allow us to keep using Aharoni's arguments, which we discuss in the following.

The discrete contributions to the demagnetising field inside the physically small region means that, for every field component and every lattice site $i$, we must perform the sum of the fields of the other dipoles $j$ inside the region

$$h_{\text{in},i}^{(\nu)} = \sum_{\substack{i \neq j \\ j \in \text{region}}} \left[ -\frac{\mu_j^{(\nu)}}{r_{ij}^3} + \frac{3\left(\boldsymbol{\mu}_j \cdot \mathbf{r}_{ij}\right) r_{ij}^{(\nu)}}{r_{ij}^5} \right] \tag{3.6}$$

where superscripts $\nu \in \{x, y, z\}$ denote Cartesian components, $\mathbf{r}_i$ is the position vector of the $i$th spin, $r_{ij}^{(\nu)} = (\mathbf{r}_j - \mathbf{r}_i)_\nu$ is the $\nu$-component of the distance between the $i$t and $j$th lattice sites and $r_{ij} = \left|\mathbf{r}_i - \mathbf{r}_j\right|$ the norm of the distance. According to Brown [122] and Aharoni [14], for a lattice with cubic symmetry these sums are zero and for non-cubic samples, it is usually possible to write the sum as proportional to the magnetic moments $\boldsymbol{\mu}_i$. Hence, remembering that $\boldsymbol{\mu}_i = g\mu_B \mathbf{S}_i = \mu \mathbf{s}_i$ and that when we perform the continuum limit $\mathbf{S}_i \to S M_s^{-1} \mathbf{M}$, we arrive to the inner field expression

$$\mathbf{h}_{\text{in}} = \Lambda \cdot \mathbf{M} \tag{3.7}$$

with $\Lambda$ as a matrix. Therefore, the stray field energy in the continuum can be written as

$$E_{\text{d}} = -\frac{\mu_0}{2} \int dV \left( \mathbf{M} \cdot \mathbf{H}_{\text{d}} + f(\mathbf{M}^2) + \mathbf{M} \cdot \Lambda \cdot \mathbf{M} \right), \tag{3.8}$$

where $\mathbf{H}_{\text{d}}$ is the micromagnetic demagnetising field (see Section 1.4.5) and $f$ is a function of the magnetisation which, at zero temperature, is a constant, thus it is disregarded. However this term came out of the small sphere assumption, hence in a general case it should be corrected. The last term in the integral is anisotropic and according to Brown [122] and Aharoni [14], it should be considered in that energy term. Therefore, one possibility is that this last expression is not being considered in the micromagnetic simulations because we only assume that the dipolar field is given by $\mathbf{H}_{\text{d}}$, which can be computed from Maxwell's equations.

Our approximations have worked on the basis of Lorentz's argument of taking defined volumes that simplify the stray field expressions in the continuum. In this regard, Adam and Corciovei [123] already questioned these assumptions, arguing that they are not sufficiently rigorous. Accordingly, they provide a more general derivation to correct the demagnetising field, which still gives an anisotropic term that involves second order derivatives and not assuming any particular geometry for a physically small volume around every lattice site [123]. Interestingly, for highly symmetric crystals, these corrections cancel out and $\mathbf{H}_{\text{d}}$ is still the main energy contribution to the dipolar field. Unfortunately, these arguments are only valid in the bulk of a magnetic sample, since Adam and Corciovei [123] focus on samples where surface effects are not important but clearly stating that they are probably noticeable in low dimensional systems, which are the cases of interest in our study.

According to the previous arguments, the following are possible solutions to keep analysing the mismatch between discrete and continuum simulations:

- Correct the anisotropy constant or add a surface anisotropy. The latest could be achieved figuring out how to compute the $\Lambda$ matrix using equation 3.6 in the continuum limit. This should probably give a kind of shape anisotropy with an out of plane hard axis since, for example, assuming a monolayer at $z = 0$, the $z$ component of the magnetisation would be

$$h_{\text{in},i}^{(z)} = \sum_{r_{ij} \in \text{ region}} \left[ -\frac{\mu_j^{(z)}}{r_{ij}^3} \right] \tag{3.9}$$

  but it is necessary to define the small region around a lattice site. Intuitively, we could use a very small sphere covering a single lattice volume, where $r_{ij}^3$ could be approximated by this volume $\Delta V$ and the term would lead to something proportional to $M_{\text{s}} m_z$, *i.e.* an uniaxial out of plane anisotropy. Nevertheless, this is in

contradiction with the argument of a sphere larger than the lattice spacing, unless we are around the limiting case. In addition, a rigorous argument is required to make zero the other field terms.

- We could try to compute the corrections from Adam and Corciovei [123] but having in mind that surface effects are still neglected. In a modern study based on computational calculations and a mixture of micromagnetic and atomistic simulations, performed by Jourdan et al. [124], they argue that the $\Lambda$ matrix is necessary to correct the result near a vortex structure (whose nonlinear magnetic structure is similar to skyrmions), but not specifying how to compute it. In his thesis, Jourdan [125] refers to Adam and Corciovei [123], hence the technique to calculate the matrix might be similar.

## 3.4. NEBM applied to Nanotracks

We begin our analysis by performing a systematic study of long tracks with different DMI constants. We define the DMI in a range from 2.6 up to 3.6 mJ m$^{-2}$ in steps of 0.2 mJ m$^{-2}$. To apply these values to a discrete spin model, we converted them from micromagnetic values considering the hexagonal nature of the sample, assuming an atomic spacing of $a_z = 2.5$ Å along the thickness. Therefore, magnetic parameters are taken from the Hexagonal(c) column of Table 3.1, making the equivalent atomistic DMI constants in the discrete model to range from $D = 0.586$ meV up to 0.811 meV in steps of 0.045 meV. The Hamiltonian to describe this system is given by the expression 3.3.

In the range of DMI magnitudes we choose, the skyrmion energy is always larger than the uniform configuration energy but it starts to get closer to that of the ferromagnetic state as the $D$ value increases, which we show in Fig. 3.2. Additionally, the systems differ in skyrmion size, where a skyrmion gets larger as the DMI constant increases (see Fig. 3.11 for detailed values of the skyrmion sizes). The length of the track is not relevant as long as the skyrmion size is not affected by the long edge boundaries, since the isolated skyrmion does not interact with them. On the other hand, the stripe width is defined according to Ref. [86], which is reasonable for a novel technological application, and the skyrmion will slightly interact with the short edge boundaries when the DMI is strong enough. Larger DMI magnitudes than the values we specify are not analysed since skyrmions acquire an elongated shape [86, 126] and the skyrmion loses its symmetrical character. A different method to modify the skyrmion dimensions, rather than varying the DMI, is tuning the uniaxial anisotropy, where a stronger anisotropy reduces the skyrmion size. However its mechanism is different to the antisymmetric exchange, thus the energy landscape is likely to change and analysing this effect goes beyond the scope of this study.

For every case, we use two different initial bands for the NEBM: (i) a linear interpolation using spherical coordinates, which means interpolating the spherical angles that

describe the magnetic moments and (ii) a skyrmion displacement towards one edge of the disk, making it disappear at the boundary.

After relaxation with the NEBM, we obtained three different transitions. One of these paths is a symmetric skyrmion collapse (shrinking) until the last spin at the skyrmion centre flips to give rise to the ferromagnetic ordering, which originates from the linear interpolation initial state. The second transition is given by the annihilation of the skyrmion core through a singularity that resembles a Bloch point (see Section 1.8). This structure has a topological charge opposite to that of the skyrmion and the transition where it is involved is observed for DMI magnitudes of 0.676 meV and above. The third transition we observe is given by the displacement of the skyrmion towards the boundary, where the skyrmion configuration is deformed until annihilation. Detailed images of these three different transitions and the initial states are provided in Fig. 3.12 and 3.13.

### 3.4.1. Boundary annihilation

We observe the skyrmion annihilation at a boundary for every DMI value. In particular, for the case of $D = 0.676$ meV, we show in Fig. 3.6b the energy band for this path and in Fig. 3.6a, the corresponding images where the skyrmion is annihilated at the boundary (see Supplementary Video S4 in Ref. [1]). Additionally, in Fig. 3.6d, we illustrate the total topological charge of the images where a smooth transition towards the uniform state occurs.

We analyse the dependence of the energy bands with respect to the DMI strength in Fig. 3.7 for the first few images of every band, and in Fig. 3.8 we plot the energy barriers with respect to the skyrmion energy using the continuous curve approximation, which is a cubic polynomial that uses information from the tangents of the images in the band (a comparison of the energy barriers values using the approximation with respect to the actual data points is shown in Section 3.4.3). The tendency in Fig. 3.8 is that the barriers decrease almost quadratically with larger DMI magnitudes, where a maximum is observed around $D = 0.676$ meV (see Table 3.3). In general, these barriers are significantly smaller than the energy difference between the skyrmion and the ferromagnetic state. To check the robustness of the results we also modified the NEBM spring constant values and we found out that there are small variations of the barriers when changing this parameter, which is mostly due to the image positioning in the band, and if the spring constant is too large the method struggles to converge. In the results of Fig. 3.7, we can notice that when increasing the DMI strength, the resolution of the images before the saddle point gets poorer, however these variations are not large and applying the climbing image method to the largest energy states gives energy barrier magnitudes similar to those obtained when performing a polynomial approximation of the band.

In the range of DMI magnitudes we analysed the skyrmion destruction at the bound-

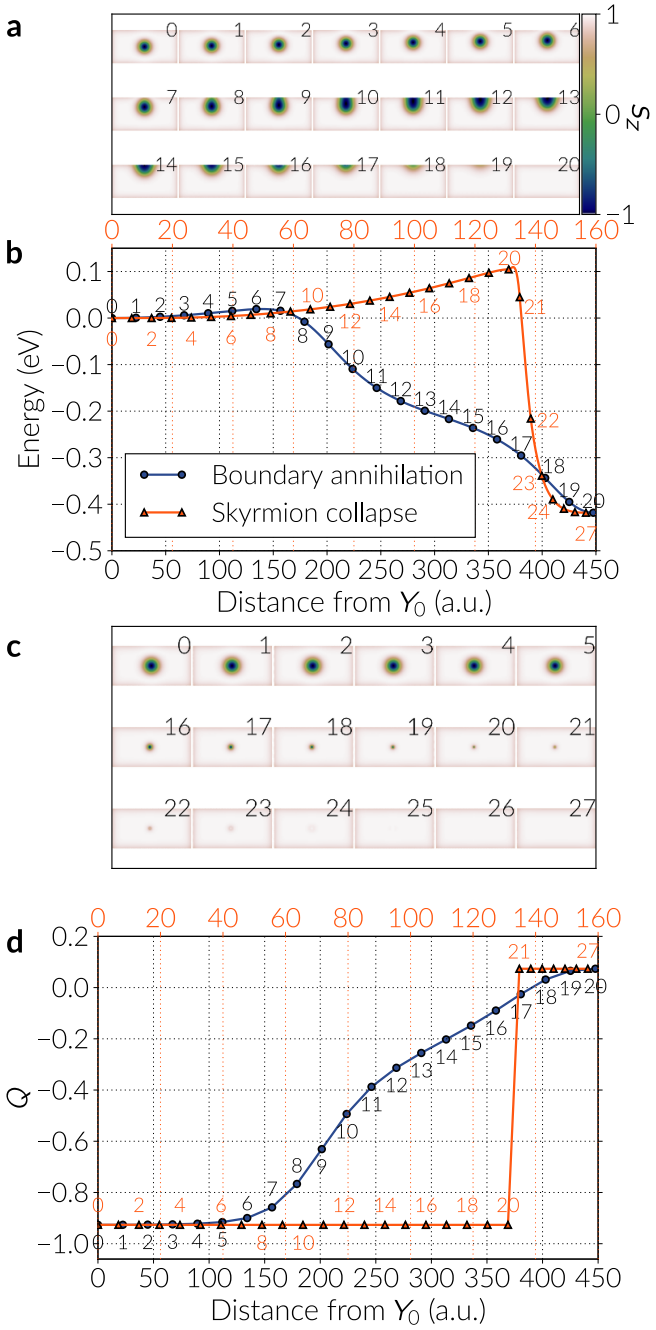


**Minimum energy paths of a skyrmion in a cobalt nanotrack.** The DMI constant of the system is $D = 0.676$ meV of magnitude. There are two different paths: a skyrmion annihilation at a boundary and a symmetrical skyrmion collapse. (a) Images of the band for the boundary annihilation, annotated according to the numbers in the corresponding curve in (b). The colour scale refers to the out of plane ($z$) component of the magnetisation field. (b) Energy bands for both minimum energy paths as a function of the distance from the first image (left extreme of the bands). The top scale refers to the skyrmion collapse case. (c) Images of the band for the skyrmion collapse. (d) Topological charge (skyrmion number) $Q$ as a function of the images distances for the cases depicted in (b). The top scale refers to the skyrmion collapse case.

Figure 3.6

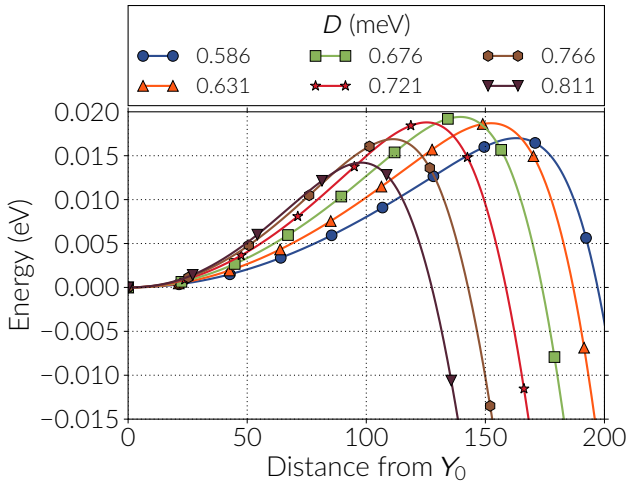


Figure 3.7 **Energy bands for the skyrmion annihilation at the boundary.** The bands are shown for different DMI constant $D$ and only for the first few images of the bands. The first or extreme left image is the skyrmion configuration and, for every case, the energy is redefined with respect to the skyrmion energy. The continuous line is a cubic polynomial interpolation.

ary is the transition that has the lowest activation energy. Specifically, the energy barriers are an order of magnitude smaller than the skyrmion collapse transitions. This demonstrates the lack of topological protection for the skyrmions, which is due to the finiteness of the system.

### 3.4.2. Skyrmion destruction

When relaxing energy paths that directly involve the destruction of the skyrmion core in a region inside the track, the spins at the center of the skyrmion reverse to form a ferromagnetic state. This is a non trivial process since the band suffers drastic changes in energy when the NEBM tries to converge to a minimum energy transition and the system must undergo a topological change. This path is (according to our observations) the most likely for a skyrmion situated in a large or infinite sample, where it is meant to be topologically protected, thus we expect a larger energy barrier than in the transition mediated by a boundary.

We firstly found that for DMI magnitudes of $D = 0.676$ meV and below, the algorithm converged to the skyrmion collapse process, which is similar to the one depicted in Fig. 3.6c. In Fig. 3.9a we show the first images of the bands, where the skyrmion state is given by the left extrema, and we observe pronounced peaks at the saddle points. These points are the images that have a tiny skyrmion with only a few spins defining its core before reversing. It is worth noting that these saddle points have a finite energy since we have a discrete number of magnetic moments, whereas in a continuum model it is likely that the peak depends on the discretisation of the continuum mesh

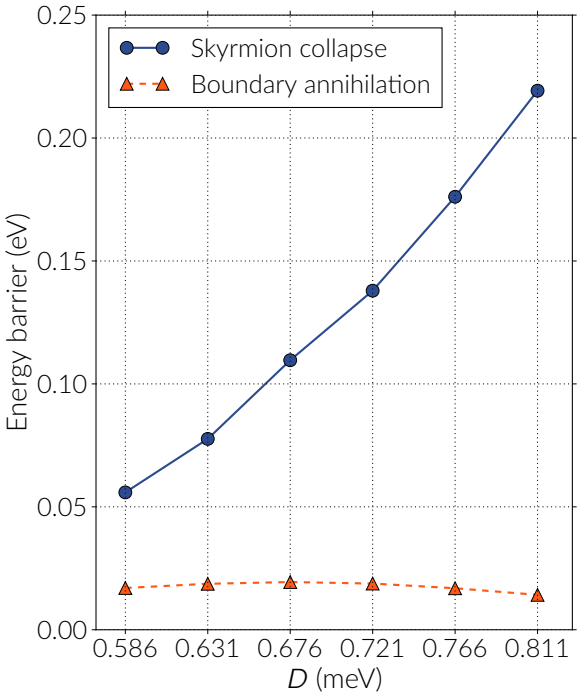


**Energy barriers for two different energy paths.** The energy barrier dependence on the DMI constant is shown for skyrmion collapse and skyrmion annihilation at the boundary. The energy barriers are calculated with respect to the skyrmion energy and using a cubic polynomial interpolation on the images of the energy bands.

Figure 3.8

that defines the material. In our results, the saddle point energies (and thus the energy barriers) increase with the DMI constant, where values range between 0.1 and 0.25 eV larger than the skyrmion energy. Around the saddle points, the energy landscape must have a rough shape since the neighbouring images usually have a drastic change in energy. Specifically, we observed that when the images move along the band before the algorithm reaches convergence, the images that cross this region suffer large energy alterations (see Supplementary Video S1 in Ref. [1] as an example). In order to resolve more accurately the energy value of the saddle points, we applied the climbing image technique on them, slightly reducing their energy and improving the resolution around them. We show these results in Fig. 3.9b (see also Supplementary Video S5 in Ref. [1]). The value of the energy barriers are summarised in Fig. 3.8 and Table 3.3, where the magnitudes increase almost linearly with the DMI magnitudes. Furthermore, as we did for the boundary annihilation, using the case of $D = 0.676$ meV, we plot in Fig. 3.6b the energy band of the skyrmion collapse path and the corresponding images in Fig. 3.6c. We notice that the saddle point lies between the 20th and the 21st image, where the last few spins at the tiny skyrmion core reverse, and there is a drastic change in energy in the next images. A different perspective of this phenomenon is observed when looking at the topological charge values of the images in Fig. 3.6d. Up to the 20th image,

| | Energy barrier (eV) | | |
|---|---|---|---|
| $D$ (meV) | Boundary | Collapse | Singularity |
| 0.586 | 0.0170 | 0.0559 | |
| 0.631 | 0.0187 | 0.0776 | |
| 0.676 | 0.0194 | 0.1096 | |
| 0.721 | 0.0188 | 0.1379 | 0.3445 |
| 0.766 | 0.0169 | 0.1761 | 0.3728 |
| 0.811 | 0.0142 | 0.2193 | 0.4016 |

Table 3.3 **Energy barriers for the skyrmion destruction energy paths..** Energy values are computed with respect to the skyrmion energy for different DMI constants. The singularity driven skyrmion destruction is only observed for strong enough DMI constant magnitudes.

the images preserve the skyrmion structure, thus having equivalent skyrmion number. However, after this point the skyrmion core is reversed and the skyrmion ordering is lost, which is indicated by a drastic change in the topological charge magnitude.

For DMI magnitudes of $D = 0.766$ meV and above, the NEBM converged to a path where the skyrmion core is destroyed by the emergence of a singularity close to the skyrmion boundary. These paths have associated energy barriers of above 0.3 eV (see Table 3.3) and we show the first images of the bands in Fig. 3.9a (see Supplementary Video S2 and Supplementary Video S6 in Ref. [1], for the evolution of the band and for the transition, respectively). The singularity that drives the skyrmion towards the ferromagnetic state resembles a Bloch point, and Fig. 3.10 shows the sequence of images of the band where this structure destroys the skyrmion, for the system with a DMI constant of $D = 0.721$ meV. This series of snapshots are zoomed around the skyrmion core and the numbers at the top left of every row indicate the image numbers in the band, which correspond to the annotated points of the curve with stars in Fig. 3.9a. The left column in Fig. 3.10 is the topological charge per lattice site $q_i$, the middle column is the DMI energy density and the right column shows the spin vector field where the colors indicate the component of the magnetisation perpendicular to the track plane, $m_z$. At the 14th image of the sequence (second row), we observe that the skyrmion core concentrates to the left side of the original skyrmion core with a drop in negative DMI energy. Moreover, the topological number is reduced since the spins in a tiny region cover most of the directions in a unit sphere, like a small skyrmion (at the 13th snapshot the topological charges are smaller since the different spin directions are more spread out). Consequently, at the 15th image a singularity emerges, which has a chirality opposite to the skyrmion, indicated by the positive gain in DMI energy and a positive charge. At this point, the skyrmion core has already been annihilated. The singularity has a hedgehog structure occupying a radius of around 3 lattice sites, and it will expand to give rise to the ferromagnetic state at the end of the energy band, decreasing the DMI energy. Characterising this singularity as a Bloch point is not trivial due to its two

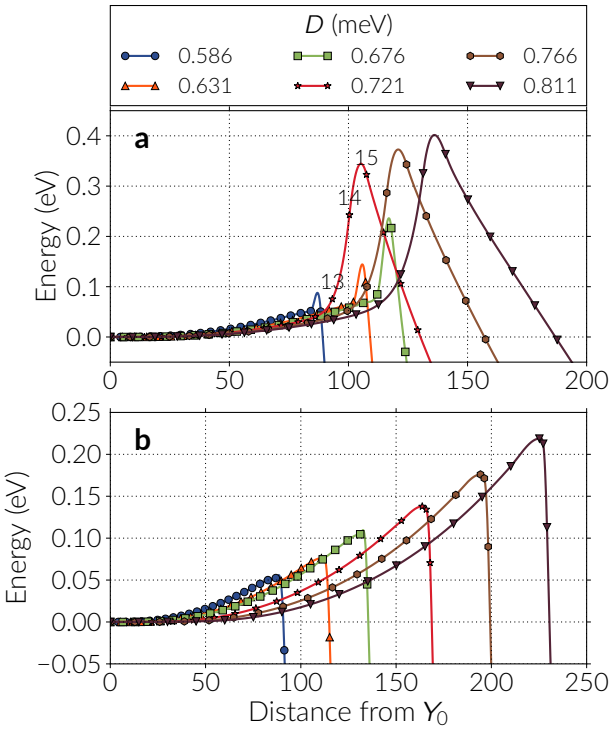


Figure 3.9

**Energy bands for two skyrmion destruction mechanisms.** The bands are shown for different DMI constant $D$ and only for the first few images of the bands. The first or extreme left image is the skyrmion configuration and for every case, the energy is redefined with respect to the skyrmion energy. The continuous line is a cubic polynomial interpolation. (a) The energy bands obtained with the NEBM. The curves for DMI values of $D = 0.676$ meV and below, are the skyrmion collapse. For values of $D = 0.721$ meV and above, the bands are the skyrmion destroyed by a Bloch point like singularity. (b) Refined energy bands obtained with the Climbing Image NEBM applied to the largest energy points of the curves in Figure (a). We expect the data in (b) to be a better approximation of the energy barrier. For this case, all the bands converged towards the skyrmion collapse path.

dimensional nature and the lacking of an appropriate resolution to mathematically define it. In fact, the critical process lies between the 14th and 15th image and if we refer at Fig. 3.9a, the 15th image is close to the saddle point of the band. Interestingly, diverse studies [80, 86, 127] have reported the mechanism of destroying or nucleating a skyrmion by means of a non trivial topological structure, when applying spin polarised currents. In particular, Elías and Verga [127] characterise this singularity by its internal magnetic field, which relates to the topological charge, and Sampaio et al. [86] show how a singularity concentrates DMI energy at the border of the skyrmion before it is nucleated (see Fig. S3 of their Supplementary Information). This transition is not a minimum energy path but it is an alternative path to disrupt the skyrmion stability that seems to be preferred by the system when following certain dynamical processes.

Although the bands where a singularity destroys the skyrmion converged without exhibiting the energy fluctuations observed in the cases with smaller DMI constants

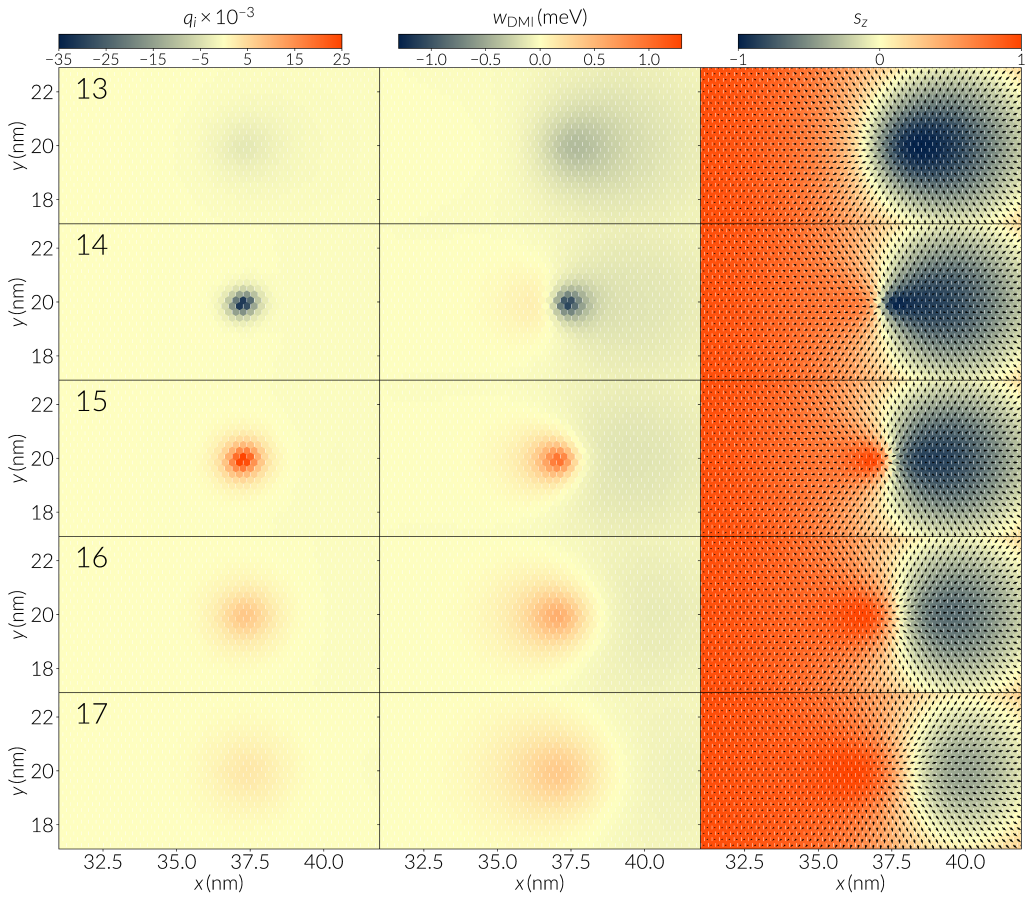


Figure 3.10 **Skyrmion destruction mediated by a topological singularity.** The sequence shows the snapshots of the energy band images for an nanotrack system of DMI constant $D = 0.721$ meV, described by a hexagonally arranged discrete spin lattice. This band corresponds to the annotated curve of Fig. 3.9a. The left column shows the topological charge density, the middle sequence the DMI energy density per lattice site and the right column the corresponding magnetisation fields. The hexagonal mesh can be distinguished from the honeycomb shaped data points. The numbers at the top left of every row indicate the image number from the energy band.

(see Fig. 3.14), they are not very stable and are likely to pass through a higher order saddle point. This is because after applying the climbing technique on the images at the saddle points, the bands converged towards the skyrmion collapse transitions. These paths have smaller energy barriers, as shown in Fig. 3.9b, and the energy barrier has an approximately linear dependence on the DMI magnitude, as mentioned previously.

Regarding the simulations with a climbing image, it is usually the case that this variation of the algorithm helps the saddle point to climb up in energy along the band and thus improve the value of the energy barriers [13, 114]. However, for the skyrmion simulations, the largest energy points decreased their energy, as seen in Fig. 3.9. Furthermore, we analysed the evolution in energy of these saddle points with respect to the number of iterations of the algorithm, and we saw that they oscillate for a while be-

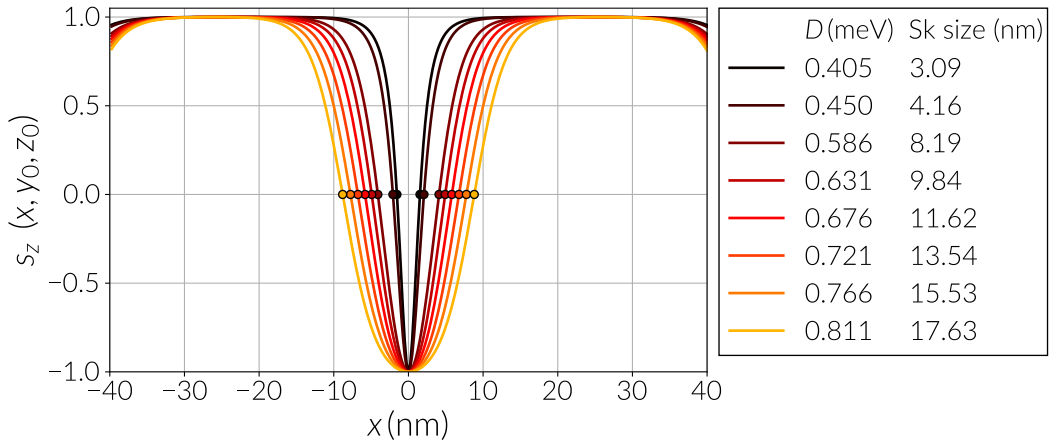


**Skyrmion profile as a function of the DMI magnitude.** For every case we show a continuous line that connects the discrete data points $s_z$ from every lattice site across the nanotrack long side (in the $x$ direction and passing through the nanotrack centre located at $(x_0, y_0, z_0)$). Small circles indicate points where $s_z = 0$ and using the distance between them we obtain the skyrmion size.

Figure 3.11

fore reaching a more stable state (see Fig. 3.14 and Supplementary Video S3 in Ref. [1]), which is given by the symmetrical destruction of the skyrmion, and these oscillations are prolonged for systems with larger DMI magnitudes. A plausible explanation for this phenomenon is as follows. As we mentioned before, the energy landscape has a rough shape or small peaks in energy around a critical point. In particular, this must be caused because a singularity that destroys a skyrmion could appear in any place around the skyrmion boundary, giving multiple possibilities for a saddle point. Additionally, besides a component of the effective force that makes a climbing image to go up in energy along the band, there is also a component that still allows it to follow a direction of minimum energy. Therefore, as the image tries to climb, it may also be pushed to a small minimum energy region if it is over a very narrow peak in the landscape, decreasing its energy. Through these dynamics, the climbing image can, overall, move to a region of lower energy and possibly to a smoother energy region, where it finally settles. Thus, according to our results, the climbing image is a mechanism that helps us to find more equilibrium solutions for the minimum energy transitions.

### 3.4.3. Simulation details

The following topics under this section show more detailed specifications of the simulations and the systems used to estimate the stability of the skyrmions. This material is based on the Supplementary Information of Ref. [1].

#### 3.4.3.1. Skyrmion size

In the main study we specified a range of DMI values to analyse the minimum energy transitions of the skyrmions. Specifically, we analysed skyrmions for DMI values from $D = 0.586\,\text{meV}$ to $0.811\,\text{meV}$ in steps of $0.045\,\text{meV}$. We obtained these skyrmions after relaxing them using the Landau-Lifshitz-Gilbert equation. In Fig. 3.11 we show the skyrmion profile for every case, by plotting the out of plane magnetisation component $m_z$ at the middle and across the long edge of the tracks. Using the convention of defining the skyrmion size as the width within the points where $s_z = 0$, we can see that the skyrmion size increases with larger DMI magnitudes. In addition, there is a small tilting at the boundaries which makes a skyrmion on the system to have a magnitude for the total topological charge, slightly smaller than one (or not perfectly zero for the ferromagnetic state).

#### 3.4.3.2. Initial states

Given an initial energy band, the Nudged Elastic Band Method (NEBM) will determine the lowest energy transition path between two equilibrium configurations that is accessible from the initial band. In general, it is difficult to predict an optimal initial guess for the bands, in particular for a system with such a high degree of complexity. In the context of the skyrmion transition, linear interpolations seem a robust starting point and are easily reproducible and applicable to different magnetic systems. A similar technique for initialising the system, where spin directions are interpolated, is using Rodrigues formula [13].

After exploring the system numerically, we also noticed the major role of the boundaries in the skyrmion annihilation and it was necessary to create an initial path close to this transition, which yields lower energy transition paths. Another way of guessing an initial path would be, for example, to use the dynamics that the system follows when applying spin polarised currents (as Sampaio et al. do in Ref. [86]) or magnetic fields (that is not the best choice since the Zeeman energy changes the energy landscape configuration). For the systems of this study, these paths converge to the same results obtained with linear interpolations.

#### 3.4.3.3. Energy band images

In our study we found three main energy paths for the skyrmion annihilation. For clarity, we provide here more detailed versions of the bands for every transition. Firstly, in Fig. 3.12 we show the skyrmion annihilation through the boundary of the nanotrack, when using a DMI magnitude of $D = 0.721\,\text{meV}$ and a band made of 21 images. In the first column of the figure, *i.e.*Fig. 3.12a, we plot the initial state for the NEBM algorithm, which we manually generate, thus we can see that the skyrmion boundaries are not perfectly defined, specially when approaching the stripe edge. The numbers at

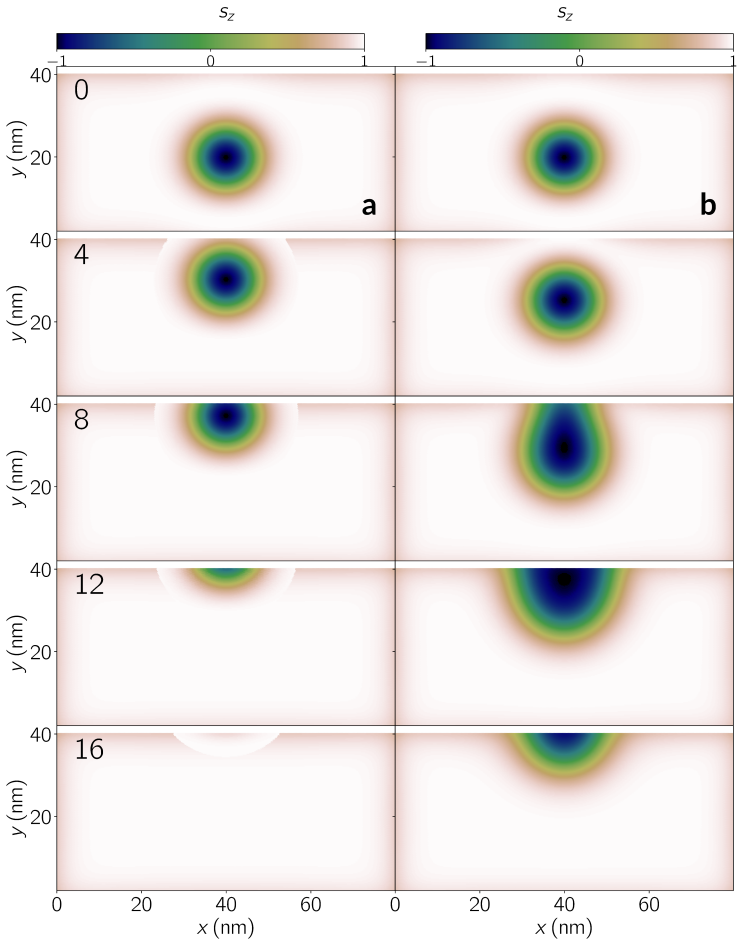


**Initial and final bands for the boundary annihilation energy path.** We use a band of 21 images based on a system with a DMI magnitude of $D = 0.721$ meV. Numbers on the top left of every row indicate the image number in the band. (a) Initial state for the NEBM algorithm. (b) Skyrmion annihilation through a boundary obtained after relaxing the band of column (a) with the NEBM.

Figure 3.12

the top left of Fig. 3.12 indicate the image number. Consequently, we apply the NEBM to this band and obtain the sequence shown in Fig. 3.12b, where helicoidal structures when the skyrmion is destroyed at the boundary are well defined, and the band has overall reduced its energy. Interestingly, the helicoidal structures are similar to those shown in in Ref. [86], when skyrmions are not successfully generated with spin polarised currents.

Similarly, in Fig. 3.13 we show the skyrmion destruction transition in three different stages, when using a DMI magnitude of $D = 0.721$ meV and a band made of 27 images. In Fig. 3.13a we depict the initial band when using linear interpolations on the spherical angles for the magnetisation field. The numbers on the top left indicate the image number in the band. Consequently, Fig. 3.13b illustrates the sequence after relaxing the initial state with the NEBM, where the final state is the skyrmion destruction

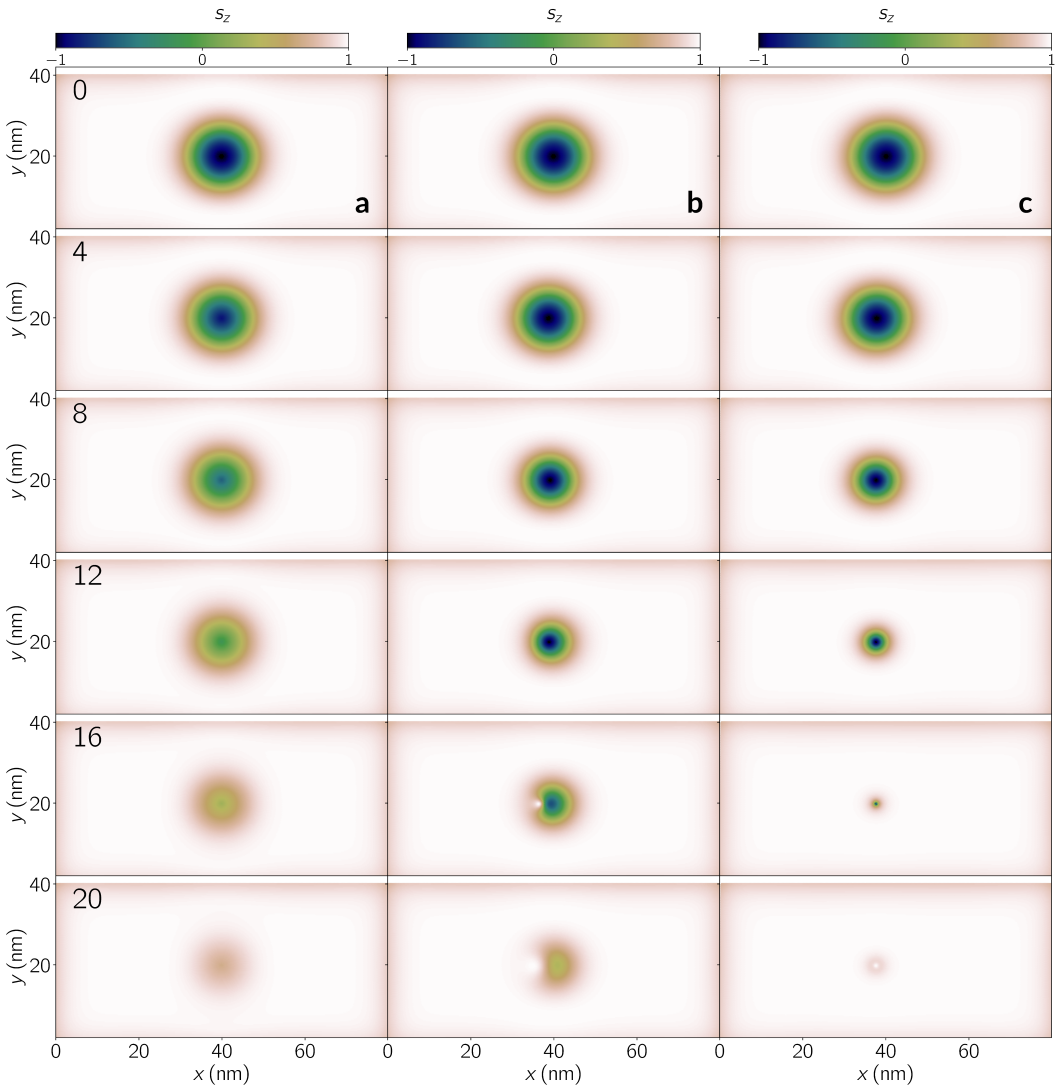


Figure 3.13 **Skyrmion destruction energy paths in three steps.** We use a band of 27 images based on a system with a DMI magnitude of $D = 0.721$ meV. Numbers on the top left of every row indicate the image number in the band. **(a)** Initial state obtained using linear interpolations. **(b)** Skyrmion destruction mediated by a singularity, after relaxing the band of column (a) with the NEBM. **(c)** Skyrmion collapse path, after relaxing the band of column (b) with the climbing image NEBM.

by a singularity that resembles a Bloch point, as discussed in the main text. Finally, the last column, shown in Fig. 3.13c, is the band of Fig. 3.13b relaxed with the climbing image NEBM, which we applied to the largest energy point of the band. For this case we clearly see the skyrmion collapse path.

#### 3.4.3.4. Skyrmion destruction evolution

According to our implementation of the NEBM, we checked how the maximum energy of the band evolves according to the iterations of the algorithm. We compute this mag-

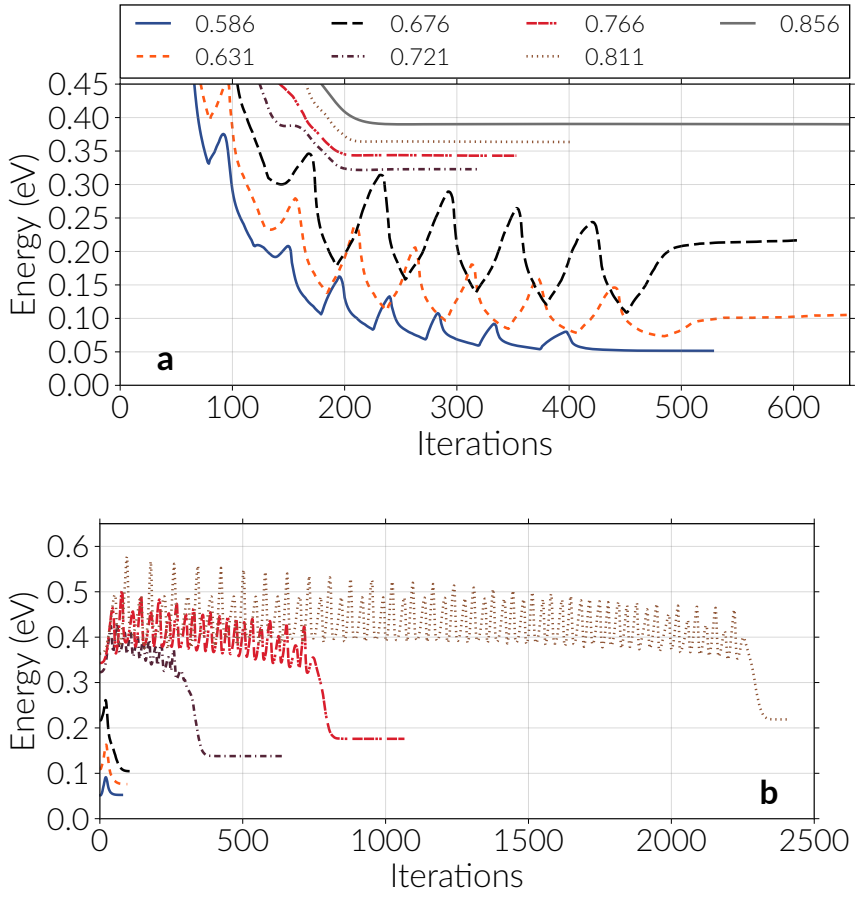


**Evolution of the maximum energy of the bands for the skyrmion destruction processes.** The evolution is computed with respect to the number of iterations of the NEBM relaxation equation (see Methods in the main text) and we show this process for different DMI values. The evolution is calculated using the images with largest energy in the bands. These images can change since they are allowed to move during the iterations. **(a)** Evolution using the NEBM and starting with linear interpolations for the initial bands. **(b)** Evolution using the climbing image NEBM, applied to the bands of (a) after relaxation (last NEBM step).

Figure 3.14

nitude using the image with the largest energy in the band, which can change since images move as the NEBM evolves. In Fig. 3.14 we show this evolution for the case of the skyrmion destruction discussed in the main text. In particular, Fig. 3.14a refers to the skyrmion destruction where the bands for $D = 0.721$ meV and above relax to the singularity mediated skyrmion destruction, and for magnitudes of $D = 0.676$ meV and below, the bands relax to the skyrmion collapse. We can observe that for the smaller DMI values, the maximum energy value oscillates before reaching convergence and this is due to the movement of images around the saddle point (where the last spins defining the skyrmion center flip) whose energy fluctuate dramatically when crossing this region.

Moreover, Fig. 3.14b depicts the evolution of the climbing image NEBM technique applied to the relaxed bands of Fig. 3.14a and all the bands relaxed towards the skyrmion

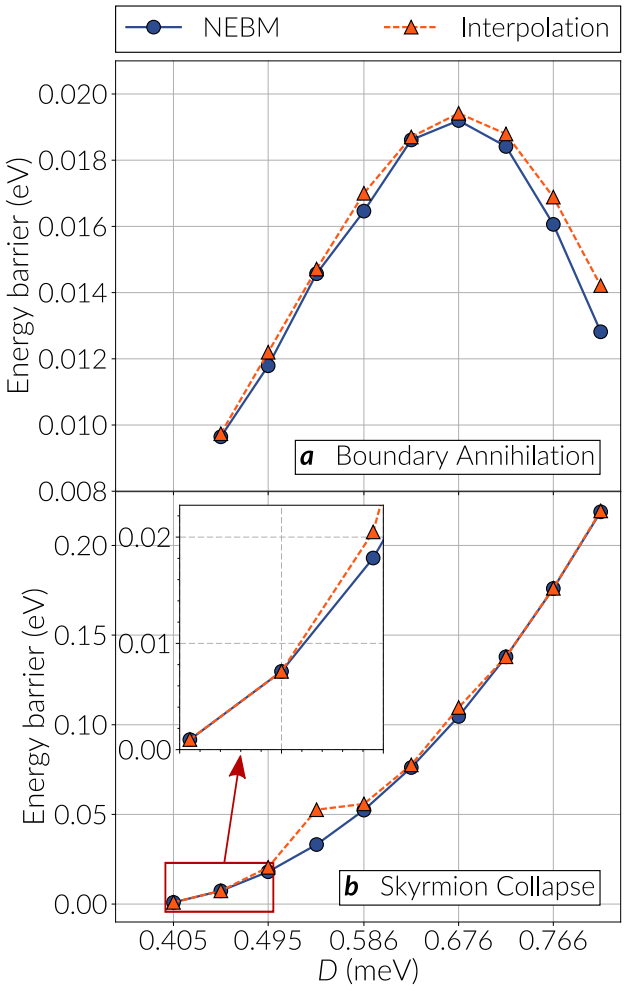


Figure 3.15 **Calculation of the energy barriers for an extended range of DMI magnitudes.** The NEBM curves show the energy barriers using the image with largest energy in the energy bands and the Interpolation curve are barriers computed when using a cubic polynomial interpolation on the bands. The energy barriers are calculated with respect to the skyrmion energy. The skyrmion cannot be stabilised below 0.405 meV. For $D = 0.541$ meV the polynomial interpolation overestimates the value of the energy barrier. The inset shows the skyrmion collapse energy barriers for the three smallest DMI magnitudes.

collapse. Bands with $D = 0.721$ meV and above take a long time to relax, specially when the DMI gets stronger. As we specified in the main text, we believe this is due to the rough shape of the energy landscape around the saddle point.

#### 3.4.3.5. Energy barriers for weak DMI

We analysed the energy barriers for DMI magnitudes in the range 0.586 to 0.811 meV. From Fig. 3.8, the tendency is that the skyrmion collapse curve decreases almost linearly in this range and extrapolating the curve it seems that at some small $D$ value it will cross the boundary annihilation curve. We then computed the values of the energy bar-

riers for DMI magnitudes weaker than 0.586 meV. Decreasing in steps of 0.045 meV, we could not stabilise a skyrmion for $D$ smaller than 0.405 meV, probably due to the strong exchange and anisotropy which are kept fixed. For this small DMI magnitude a skyrmion is only 3.09 nm wide.

We show in Fig. 3.15 the energy barriers computed for the whole range of DMI values in the main study and down to 0.405 meV. In this plot, we show both the energy barriers obtained using the image with the largest image in a band, which we call NEBM curve, and the energy barriers obtained after performing a polynomial interpolation on the bands, named Interpolation curve. In general, the interpolation gives optimal results for the boundary annihilation, which can be seen from Fig. 3.7. For the skyrmion collapse the polynomial approximation appears to agree well with the largest point of the band in most cases, but sometimes it can slightly overestimate the energy barrier when there is no good resolution around the saddle point, which is given by the reversal of the spins at the skyrmion nucleus. In particular, this happens for $D = 0.541$ meV, which is shown in Fig. 3.15b. Nevertheless, the quadratic tendency is clear when using the points from the NEBM curve. Interestingly, when comparing the inset of Fig. 3.15b with Fig. 3.15a at $D = 0.450$ meV, where the skyrmion is only 4.16 nm wide, the energy barrier of the skyrmion collapse is slightly smaller. Decreasing the DMI even further we could not obtain a clear value for the boundary annihilation, however in this range the skyrmion collapse barrier is smaller than 0.002 meV.

### 3.4.4. Discussion

Studying the paths through phase space along which a skyrmion can be annihilated from a track or created in the track, we find that for the geometry studied the lowest energy barrier is generally found by using the boundary of the track (see transition snapshots in Fig. 3.6a). This transition path circumvents the topological protection, as has been pointed out by Streubel et al. [83] explaining that the skyrmion topological protection is non-existent due to the system finiteness. Therefore, the low stability of these configurations found by the NEBM simulations seems reasonable. We quantify this stability by analysing the results using the Arrhenius-Néel law for the relaxation time

$$\tau = \tau_0 \exp\left(\frac{\Delta E}{k_B T}\right) \tag{3.10}$$

where $\tau_0$ is related to the attempt frequency $f_0 = \tau_0^{-1}$, $T$ is the temperature and $k_B$ is the Boltzmann constant. The attempt frequency magnitude is not easy to obtain since the theory normally refers to simple or macrospin systems, but its value is usually in the range [14, 128] $10^9$ to $10^{12}$ Hz. Using our computed values for the skyrmion energy barriers and $f_0 = 10^9$ Hz, we obtain, at room temperature: (i) for the boundary annihilation in nanotracks with $D = 0.676$ meV (barrier of approximately 0.0194 eV) an average lifetime of $\tau = 2.117$ ns, whereas (ii) for the skyrmion collapse, the barrier

is 0.110 eV, thus this gives us $\tau = 70.347$ ns. We must notice that the exponential is very sensitive to the energy barrier values, which can make a difference if the system follows the skyrmion collapse path, and $f_0$ could be smaller, which would make the lifetimes some orders of magnitudes larger. Although these times seem very small, they are computed at room temperature, hence an experiment [56] at 4.2 K, for example, would make a relaxation time of $\tau = 1.864 \times 10^{14}$ s. To confirm the phenomenon of low barriers, it would be ideal to compare experimental data showing skyrmion switching times that could be used to estimate an attempt frequency and exponential law for its average lifetime.

Moreover, we can compare our calculated energy barriers with respect to recent magnetic recording technology. In the context of heat assisted magnetic recording technology, using the data from Weller et al. [129] and approximating a magnetic grain with a spherical shape, the energy barrier for that system is approximately 95.54 $k_B T$ at room temperature ($T = 300$ K). In addition, from typical parameters of magnetic grains in perpendicular recording media, provided by Richter [4], we can estimate energy barriers of about 97.06 $k_B T$. On the other hand, for the skyrmionic system of $D = 0.676$ meV, the boundary annihilation gives us a barrier of only 0.75 $k_B T$ and the skyrmion collapse a barrier of 4.24 $k_B T$, which substantiates our findings of low thermal stability of skyrmions in confined systems.

This phenomenon of low stability must also be present in other finite geometries, like cylindrical structures that have been proposed recently [66, 86, 91], complicating any technological application of these systems, at least at room temperature, since at lower temperatures the energy barrier can be significant. For skyrmion based technology to operate at room temperatures, we need to find systems with larger energy barriers for skyrmion destruction; other DMI hosting materials such as those with a bulk interaction, or those of increased thickness may have larger barriers. This claim is only speculative since modifying the parameters involved in the system, such as adding thickness to the sample or applying external magnetic fields, changes the energy landscape and different paths would be encountered with the NEBM relaxation, which would require a proper analysis in a different study. On the other hand, a recent theoretical study [130] has proposed taking advantage of edge instabilities for the creation of skyrmions through the boundaries of a track, avoiding other larger topological energy barriers from different energy paths.

The processes of destroying the skyrmion by a collapse or by a singularity, are energetically feasible due to the discrete nature of the crystal lattice. In the case of an infinite system (i.e. no geometry boundaries), we have observed so far that these paths are the only possible ways to destroy a skyrmion. Thus having a skyrmion far away from boundaries is an option to get more stability but requires larger structures. Regarding the Bloch point like transition, we mentioned that it is not observed for the cases with weaker DMIs. We believe this is because it might be difficult to resolve this structure,

which spans a circle of about 3 lattice points of diameter, when the skyrmion is sufficiently small. Our preliminary results on samples of Fe on Ir, where skyrmions are only a few nanometres wide, have confirmed this.

We must emphasize that we are using an atomistic spin model, where each spin represents one atomic magnetic moment and which requires more computational effort than a micromagnetic model. However, a continuum description of the magnetisation field is inaccurate since the skyrmion collapse or Bloch point occurring in the higher energy paths we find, break the assumption of micromagnetics that the magnetisation changes slowly as a function of position. Because of this violation, it is not possible to predict quantitatively the energy associated to the saddle points of these paths, giving the energy barriers dependence on the sample discretisation.

Furthermore, for the skyrmion collapse path the energy barriers are larger for increasing DMI values. This is because the energy of helicoidal configurations approaches that of the ferromagnetic state, reaching a point where helicoids become the ground state of the system. Additionally, larger DMI magnitudes favour multiple twistings of the magnetisation. Therefore, paths that directly involve helicoidal structures are significantly preferred. This is also the reason why the boundary annihilation has very low barriers for strong DMI cases.

For DMI magnitudes below the range we have studied, the energy barriers become smaller and we noticed that at $D = 0.450\,\text{meV}$ the skyrmion collapse has a slightly smaller energy barrier than the boundary annihilation, which is expected from the tendency of the curves of Fig. 3.8. However, this DMI value is close to a critical value of $D = 0.405\,\text{meV}$, below which a skyrmion cannot be stabilised anymore. These results are shown in Appendix 3.4.3.

A recent publication [109] reports a study on cobalt monolayers by means of the NEBM and two different observed transition paths. Their so called Path 1 is similar to the skyrmion collapse we have reported in this work and, recently, by Lobanov et al. [110]. Their Path 2 adds a rotation of the spins before the core collapses, which resembles a horizontal cut of a three dimensional Bloch point. Although we observe this topological structure, in our case it usually appears at the skyrmion core boundary for large enough skyrmion sizes, which depends on the DMI magnitude. We have only noticed a skyrmion collapse with rotating spins as the initial state when we set up the initial band using linear interpolations, but which disappears as the elastic band reduces its energy. This has been also confirmed by Lobanov et al. [110]. In this context, a key difference between this skyrmion stability study and Ref. [109, 110] is that we take the role of the boundary into account. We find that skyrmion annihilation and creation via the boundary has an order of magnitude lower energy barrier for this track geometry and will thus be the preferred path for the system.

In summary, it is important to consider that due to the finite nature of magnetic samples in real life, skyrmions will have a weaker stability since they can be destroyed through

the boundaries and there is no topological protection. It may be possible to overcome this through geometry, material and device design.

All data from this study, used to create the figures, can be reproduced from a repository in Ref. [131].

# Chiral structures in Pd(Pd)/Fe/Ir islands

Chapter 4



The theoretical prediction of skyrmions in ferromagnetic materials has been confirmed in numerous experimental studies where non collinear structures are observed when imaging the magnetisation field profile. The first observations [132] of skyrmionic textures were obtained by Mühlbauer et al. using neutron scattering [37] and by Yu et al. using Lorentz transmission electron microscopy (LTEM) imaging [39]. Following investigations with LTEM [55, 133] and other techniques such as magnetic force microscopy [41], electron holography [134], X-ray magnetic circular dichroism with scanning transmission X-ray microscopy [50–52], differential phase contrast imaging with scanning transmission electron microscopy [36] and scanning tunneling microscopy with a spin-polarised tip [19, 58] (SP-STM), have also been effective for sampling the presence of skyrmions in chiral magnets.

In particular, Romming et al. [56, 58] have applied the SP-STM technique to characterise skyrmions in bilayers of palladium and iron above iridium surfaces. The stabilisation of skyrmionic textures in these PdFe samples requires the application of an external magnetic field and the skyrmion dimensions are significantly smaller than those found in cobalt based systems that have so far been shown in the literature. Palladium-iron systems can be controlled in order to delete and write individual skyrmions using spin-polarised currents [56], and the single spin resolution of the SP-STM has allowed to parameterise the skyrmion size as a function of the applied magnetic field by directly comparing experimental data and analytical theory [58]. Other non-collinear structures, such as spin spiral, are also observed as equilibrium states, in particular at zero field where they arise as the ground state of these systems [56]. These results have shown that PdFe on Ir samples are physically interesting systems for the study of chiral structures and for improving our understanding of the stability of skyrmions in crystals with broken symmetry.

In this chapter we analyse, through numerical simulations, PdFe islands on top of a (111)Ir surface, where the spatial confinement allows the stabilisation of a variety of non collinear configurations. We compare these results with experimentally observed magnetic orderings obtained from a study on this material (see Section 4.6) with different geometric shapes. Furthermore, in these experimental studies the islands have been manipulated by adding an extra Pd layer, affecting the island's magnetic environment and thus, the stabilisation of the magnetic structures. By widening our knowledge

| Constant | Unit | Romming et al. Pd on Fe on Ir(111) | Dupé et al. Pd(hcp) on Fe on Ir(111) | Dupé et al. Pd(fcc) on Fe on Ir(111) | Dupé et al. Pd BL(fcc) on Fe on Ir(111) | Simon et al. Pd(fcc) on Fe on Ir(111) |
|---|---|---|---|---|---|---|
| $a_z$ | Å | 4.08 | 4.08* | 4.08* | 6.31* | 4.08* |
| $J_{ij}$ | meV | 5.88 | 13.2 | 14.7 | 9 | 16.87 |
| $\mu$ | $\mu_B$ | 3.0 | 3.0* | 3.0* | 3.3* | 3.0* |
| $D_{ij}$ | meV | 1.56 | 1.2 | 1.0 | 1.35 | 0.82 |
| $\mathcal{K}$ | meV | 0.41 | 0.8 | 0.7 | 0.8 | 0.5 |
| $A$ | pJ | $2.0 \pm 0.4$ | 4.49 | 5.00 | 1.98 | 5.74 |
| $M_S$ | MA m$^{-1}$ | 1.1 | 0.96 | 0.96 | 0.76 | 1.07 |
| $D$ | mJ m$^{-2}$ | $3.9 \pm 0.2$ | 3.01 | 2.51 | 2.19 | 2.05 |
| $K$ | MJ m$^{-3}$ | $2.5 \pm 0.2$ | 4.92 | 4.31 | 3.18 | 3.07 |

Table 4.1 **Summary of magnetic parameters for PdFe or PdPdFe on an Ir surface.** The top panel refers to the atomistic values and the bottom panel to the micromagnetic ones. The third column of numerical data refers to a bilayer (BL) of Pd on top of Fe and Ir(111). Romming et al. [58] use experimental values and an analytical model to get the continuum magnitudes. Both Dupé et al. [135] and Simon et al. [64] use *ab-initio* calculations to compute the atomistic magnitudes and we show the values for the nearest neighbour interactions, although effective parameters that consider the effect of the next neighbours would be more adequate to our model [112]. The corresponding micromagnetic values are obtained using the formulas from Section 1.4. The atomic spacing of iron is $a_{\text{Fe}} = 2.715$ Å. We use values for an fcc stacking of both Fe [135]. Dupé et al. claim that Fe induces a magnetic moment of 0.3 $\mu_B$ on the Pd overlayer [135], thus we use this magnitude to estimate $\mu$ for PdPdFe, and for PdFe given by Simon et al. [64]. In addition, the sample thicknesses are computed according to the sum of corresponding interatomic spacings (see Supplementary Information for [135]): $a_{\text{Pd-Pd}} = 2.24$ Å, $a_{\text{Pd-Fe}} = 2.02$ Å and $a_{\text{Fe-Ir}} = 2.06$ Å. This simplification goes according to our assumption of a single entity for the 2 or 3 layers, although Ref. [64, 135] only refer to the Fe monolayer to perform atomistic simulations. Hence we marked the magnitudes from our approximation with a $*$.

about the equilibrium states present in these systems, it will be easier to estimate the stability of skyrmionic textures since we will have a better idea of the possible transition paths that these configurations might follow in the energy landscape.

In order to validate our simulations with the results of Ref. [58] we start by analysing the magnetic properties of skyrmions in the micromagnetic framework. In this context, considering that we are dealing with a monolayer system (ultrathin film limit), we treat the effect of dipolar interactions as an uniaxial anisotropy since an effective value for the anisotropy constant is extracted directly from a fit to experimental data using micromagnetics [58]. We discuss this in the first section of this chapter. Consequently, we convert the material parameters from the continuum to the discrete spin model and continue our analysis of PdFe or PdPdFe systems under this theoretical framework.

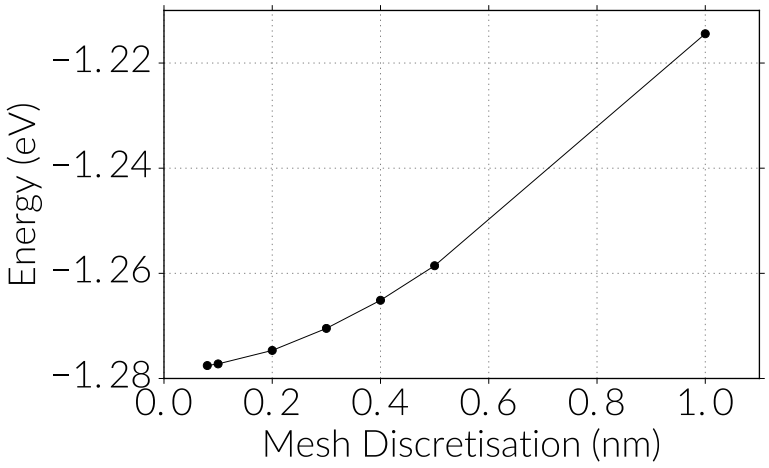


Figure 4.1

**Effect of the mesh discretisation on the energy of an isolated skyrmion.** Result of finite elements based micromagnetic calculations of the energy of a skyrmion in a Pd/Fe/Ir(111) sample, as a function of the discretisation of the mesh. The simulation is made in a two dimensional sample, where the discretisation refers to the average spacing between finite elements. The system's geometry is a 16 nm by 16 nm square. The energy is scaled by a monolayer thickness of 4.08 Å. The skyrmion is stabilised applying a magnetic field of $B_z = -1.5\,\mathrm{T}$. Material parameters are specified in Table 4.1.

## 4.1. Material characterisation

Originally, experiments performed in Pd/Fe/Ir(111) systems observed skyrmions and spin spirals in large samples. In this study we aim to study small confined islands and the effect of the geometry on the stabilisation of different chiral magnetic orderings. This material has an out of plane uniaxial anisotropy and the spin orbit coupling effect from the Pd overlayer and the Ir surface on the Fe material, induces an interfacial DMI, which is crucial for stabilising chiral states. However, skyrmions remain stable only when an external magnetic field is applied to the system. Regarding the influence of dipolar interactions, in these thin and small samples we will approximate them as an uniaxial anisotropy, as we explain in the next section.

### 4.1.1. Micromagnetics

In the study performed by Romming et al. [58], they fit the magnetisation field of Néel type skyrmions from their experimental data with a function based on the superposition of two domain walls, which we specified in equation 1.55. Although this function is defined in the continuum limit, there is a good agreement between the data and the analytical theory. This allows to describe the system within micromagnetics by directly extracting the magnetic parameters from a comparison of the function fit with an analytical energy functional that describes the system. Using this information it is possible to perform computational simulations to support the experimental results [58] and pre-

dict new phenomena.

In the energy functional described in Ref. [58] the demagnetising field is not considered explicitly. According to our discussion in Section 3.2, in the ultrathin film limit the energy contribution from dipolar interactions become significantly small [69, 110]. In addition, it is possible to approximate them as an uniaxial anisotropy [112], in particular for axisymmetric solutions (which can be proved analytically [30]), hence in the magnetic parameters from Ref. [58] the demagnetising field effect lies in the anisotropy constant (notice that if the stray field is taken explicitly as in Ref. [67] the anisotropy constant is likely to have a smaller magnitude). Thus far the most general proof about this approximation for thin films can be found in Ref. [136]. An important advantage of estimating the non-local dipolar interactions as an anisotropy is that numerical computations run and converge noticeably faster.

The energy functional for a magnetic structure $\mathbf{M} = M_s\mathbf{m}$ in a PdFe bilayer is written as

$$E = t\int_\Omega \mathrm{d}\Omega\left\{A\sum_{\alpha,\beta\in\{x,y,z\}}\left(\partial_\alpha m_\beta\right)^2 + D_c\left[\mathcal{L}_{xz}^{(x)} + \mathcal{L}_{yz}^{(y)}\right] - K(\mathbf{m}\cdot\hat{z}) - B_z M_z\right\} \tag{4.1}$$

The integration of the system is based on the assumption of a large sample of area $\Omega$ with thickness $t$. The PdFe bilayer is assumed as a single entity, thus we have a two dimensional system with $\mathbf{m} = \mathbf{m}(x,y)$, and the thickness of the sample is taken as the interatomic distance between Pd and Fe plus the distance between Pd and Ir, *i.e.* $t = a_{\text{Pd-Fe}} + a_{\text{Fe-Ir}} = 4.08$ Å. This distance is used to compute the saturation magnetisation $M_s$ from the $\mu$ value obtained by *ab-initio* calculations [135]. For this material, the DMI expression favours spin spirals whose rotation resemble Néel domain walls[1]. The effective anisotropy $K$ takes into account an uniaxial anisotropy and the approximation of the demagnetising field. The final term is the Zeeman energy for the applied magnetic field in the $z$ direction.

To describe a skyrmion in this system we use spherical coordinates for the magnetisation $\mathbf{m} = (\sin\theta\cos\psi, \sin\theta\sin\psi, \cos\theta)$, in terms of cylindrical coordinates as was done in Section 1.7.1. According to the symmetry of the skyrmion $\theta = \theta(\rho)$, $\psi = \psi(\varphi)$ and this DMI form accepts solutions with $\psi = \varphi$, hence the energy functional turns into

$$\begin{aligned} E = 2\pi t\int_0^\infty \Big\{ & A\left[(\partial_\rho\theta)^2 + \rho^{-2}\sin^2\theta\right] + D_c\left(\partial_\rho\theta + \rho^{-1}\sin\theta\cos\theta\right) \\ & - K\cos^2\theta - B_z M_s\cos\theta\Big\}\mathrm{d}\rho \end{aligned} \tag{4.2}$$

Using our finite elements micromagnetic code [77] we reproduced an isolated skyrmion employing a two dimensional PdFe bilayer with PBCs. The micromagnetic parameters

[1] Notice that the chirality is opposite to the one in Cobalt samples.

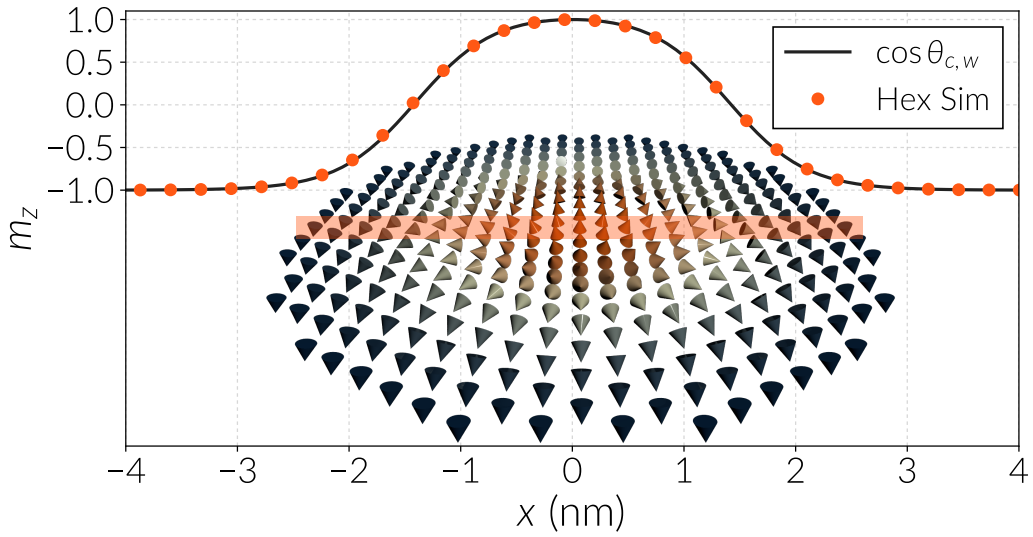


Figure 4.2

**Simulation of a skyrmion using a discrete spin model in a Pd/Fe/Ir(111) sample.** The PdFe bilayer is characterised by an hexagonal lattice. Data points correspond to the out of plane component of spins positioned along a line in the $x$ direction across the skyrmion centre located at $(x_0, y_0, z_0)$, as indicated by a rectangle in the skyrmion plot below the curve. The skyrmion spin field at the bottom is coloured according to the spins out of plane component $s_z$. The skyrmion was obtained using an atomistic simulation (Hex Sim) with a magnetic field of $B_z = -1.5$ T magnitude. The curve corresponds to the analytical model specified in equation 1.55, with values $c = 1.4$ and $w = 1.39$ obtained from Figure 2 of Ref. [58].

for the interactions, based on Ref. [58], are specified in Table 4.1. One particular result is shown in Fig. 1.5, for a skyrmion under an applied out of plane magnetic field of -1.5 T of magnitude, without considering dipolar interactions and using a finite element discretisation of 1 Å. Alongside the comparison with the analytical model, we performed an extra test of the micromagnetic simulation by defining samples of 16 nm by 16 nm and analysing how the energy of the system converges when decreasing the mesh spacing, *i.e.* in the continuum limit. These results are summarised in Fig. 4.1, where the energy curve tends to a value slightly above -1.28 eV and hence proving that a full skyrmion ordering is well described within the continuum model.

To describe other magnetic configurations present in this system we have to generalise the dependence of the spherical functions that define the magnetisation as $\theta = \theta(\rho, \varphi)$, $\psi = \psi(\rho, \varphi)$, however no closed form solution is known for spin spirals using this formalism. The standard procedure to describe more complex states is taking the corresponding interactions with $\mathbf{m}$ in Cartesian coordinates, and integrate the system numerically using the Landau-Lifshitz-Gilbert equation.

### 4.1.2. Atomistic

While the continuum theory can accurately describe skyrmion profiles, it is not optimal for analysing the stability of skyrmions since the mesh discretisation has an influence on the energy of some of the transitions required to destroy or nucleate them. Accordingly, we prefer an atomistic description of the system, which also provides a more accurate representation of the hexagonal crystal lattice of PdFe islands, and in Table 4.1 we show the micromagnetic parameters that fit the experimental data and the corresponding calculated atomistic parameters.

Within the discrete spin model we write the Hamiltonian for this system as

$$\mathscr{H} = -J\sum_{\langle i,j\rangle}^{P}\mathbf{s}_i\cdot\mathbf{s}_j + D\sum_{\langle i,j\rangle}^{P}\left(\mathbf{r}_{ij}\times\hat{\mathbf{z}}\right)\cdot\left[\mathbf{s}_i\times\mathbf{s}_j\right] - \mathcal{K}\sum_{i}^{P}\left(\mathbf{s}_i\cdot\hat{\mathbf{z}}\right)^2 - \sum_{i}^{P}B_z\mu_i^{(z)} \quad (4.3)$$

where $P$ is the number of spins, which depends on the lattice constant and the size of the island, $\mathcal{K}$ is an effective anisotropy taking into account an uniaxial anisotropy and an approximation of the dipolar interactions (see discussion in Section 4.1.1), $D$ is the DMI constant that describes the interfacial DMI for this material and the last term is the Zeeman interaction for the field applied perpendicular to the sample plane. As we did in the micromagnetic description, we treat the PdFe bilayer as a single material, therefore we only simulate a monolayer of spins to obtain our results.

Instead of calculating the continuum parameters obtained from a fit using experimental data, a different approach to obtain material parameters for the discrete model is through *ab-initio* calculations of the samples as has been done by Dupé et al. [135] and Simon et al. [64]. Correspondingly, we compare the magnitudes of the magnetic parameters obtained with different theoretical methods and summarise published results in Table 4.1. We notice that the best agreement with Romming et al. [58] results are from the Pd bilayer on Fe/Ir(111), nonetheless the first principle calculations overestimate the value of the uniaxial anisotropy. It is important to mention that the exchange and DMI parameters from first principle calculations in Table 4.1 were extracted only for the nearest neighbours from Refs. [64, 135]. However, it is known, for instance, that the exchange interaction is smaller in magnitude and antiferromagnetic with the next nearest neighbours and keep decreasing and varying in sign beyond them, which makes a frustrated exchange interaction [112]. Hence, it is customary take into account these long range effects by using effective parameters, nevertheless they are not commonly found in the literature. Only recently, Malottki et al. [112] have published a comparison of the effects of using an effective exchange or a long range frustrated exchange on the skyrmion stability in a Pd/Fe/Ir(111) system and magnitudes of the parameters involved in their study.

Using the converted parameters for the discrete spin model we simulated an isolated skyrmion in a PdFe bilayer by applying a magnetic field of $B_z = -1.5$ T to directly com-

pare its size with that of the skyrmion obtained experimentally in [58]. This result is shown in Fig. 4.2 where we plot the out of plane component of the spins at the centre of the skyrmion. The data points in the curve correspond to the spin directions from the spin field below the curve, which has a hedgehog-like profile characteristic of skyrmions with interfacial DMI. We compare the atomistic spin field profile with the continuum $\theta$ function that describes the magnetisation (see the final discussion in Section 1.7.1), where the parameters for the function were obtained from a fit to an experimental skyrmion image [58]. Remarkably, there is a perfect agreement between the discrete model and the continuum solution.

## 4.2. Magnetic textures in Pd/Fe/Ir(111) islands

In a recent experimental study, Romming et al. (see Section 4.6) have fabricated hexagonally shaped islands of biatomic PdFe on top of an Ir(111) surface and performed an SP-STM analysis on them, obtaining a series of images of a variety of magnetic orderings at different applied magnetic fields. Among these configurations, Néel skyrmions arise at specific magnetic field magnitudes, whose size agree with the ones described in Ref. [58] at large enough fields, since at weak fields the boundary of the island restricts the skyrmion shape, which tends to expand beyond the island edges. Furthermore, different helicoidal structures also emerge as equilibrium states and in some cases are observed along with skyrmions. Compared to the symmetrical skyrmions, helices are in general more difficult to describe due to the multiple orientations and branches they can adopt.

Our interest is on characterising this diversity of experimentally observed magnetic states by means of atomistic simulations. We seek to establish more precise ranges of parameters where the magnetic configurations can be stabilised and elucidate the physics involved on this process. Moreover, there are several other possible configurations that can be easily obtained through numerical calculations, hence our results can clarify if they could be realisable in laboratory for observation. We must keep in mind that experiments are performed at low temperatures and the microscope provides a small bias current when probing a sample thus the parameters in experimentally observed states cannot be compared exactly with our numerical outcomes, since the discrete spin model does not consider thermal fluctuations or any external excitation aside from the applied magnetic field.

## 4.3. Hexagonal islands

We have replicated the hexagonal islands obtained in experiments by defining a discrete spin lattice according to a bitmap image of a Pd/Fe/Ir(111) island with its corresponding spatial scale. We show both an experimental image of an island (see Section 4.6) and a computer simulated lattice for this island in Fig. 4.3a and b, respectively. The lattice is

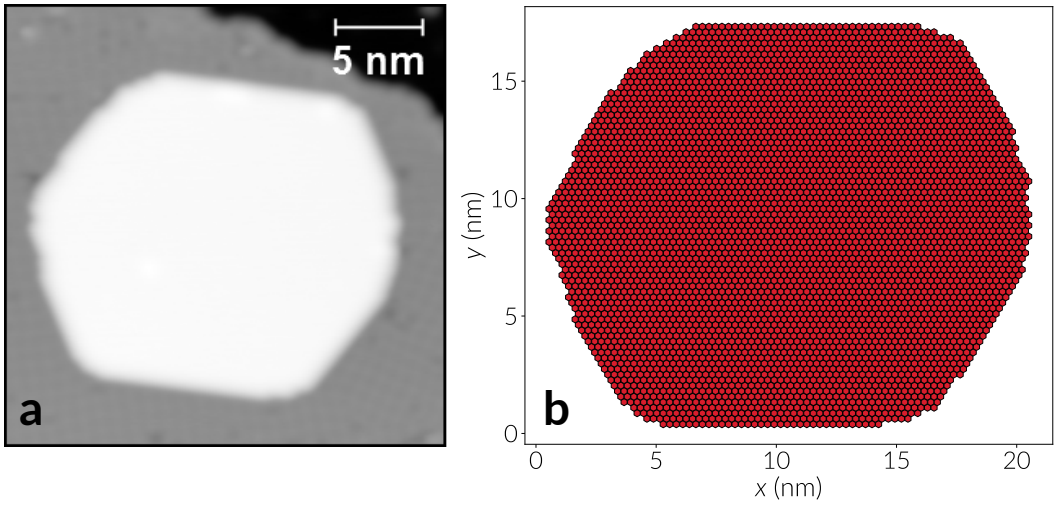


Figure 4.3 **Simulation of a hexagonal island from experiment.** (a) Image of a Pd/Fe/Ir(111) island, obtained experimentally by the group of Roland Wiesendanger at the University of Hamburg (see Section 4.6) using SP-STM. (b) Translation of the PdFe bilayer from experiment into an atomistic simulation, using a hexagonal lattice of spins. We use the lattice constant from Fe, $a_{\mathrm{Fe}} = 2.715\,\text{Å}$. The original image was rotated, simplified into a black and white colourmap and then converted to a discrete spin lattice using Fidimag [78]. The lattice is made of 4498 spins.

defined with an hexagonal arrangement of spins. We have assumed that atoms align uniformly along the edges thus although there are defects in some areas at the boundaries, the geometry is mostly well defined with the hexagonal arrangement of the atoms.

We begin our study by identifying a diverse range of skyrmionic textures obtained experimentally (see Fig. 4.7c-d) and predicted by our atomistic simulations, thus in Fig. 4.4 we show the energies and topological charge of five different configurations: (●) a uniform ordering, where spins are slightly tilted at the boundaries, (▲) a single skyrmion, as the one shown in Fig. 4.2, (■) three skyrmions, which are deformed because of the inter-skyrmion force, the boundary repulsion and because at this field magnitude they tend to occupy a larger area, (▼) a target state, which has been originally referred by Bogdanov and Hubert [31] as $2\pi$-vortex, and (×) a $3\pi$-vortex, which is a target state with an extra rotation. Our approach in Fig. 4.4 is to start with initial states that look similar to the five configurations and relax them using the Landau-Lifshitz-Gilbert equation for different magnetic fields. At the bottom of Fig. 4.4 we show relaxed states of the five configurations at applied fields of $B_z = -0.7\,\text{T}$ and $-1.0\,\text{T}$. They do not look the same for both fields because lower energy states can be found during relaxation or some of the configurations can become unstable. We will explain this in the following discussions, where we analyse the results of Fig. 4.4 in more detail.

For the five magnetic orderings used as initial state, ideally we would obtain similar configurations after relaxation. If this is the case, some of them can be distinguished by their topological charge, which we show in Fig. 4.4b. These values are not integer

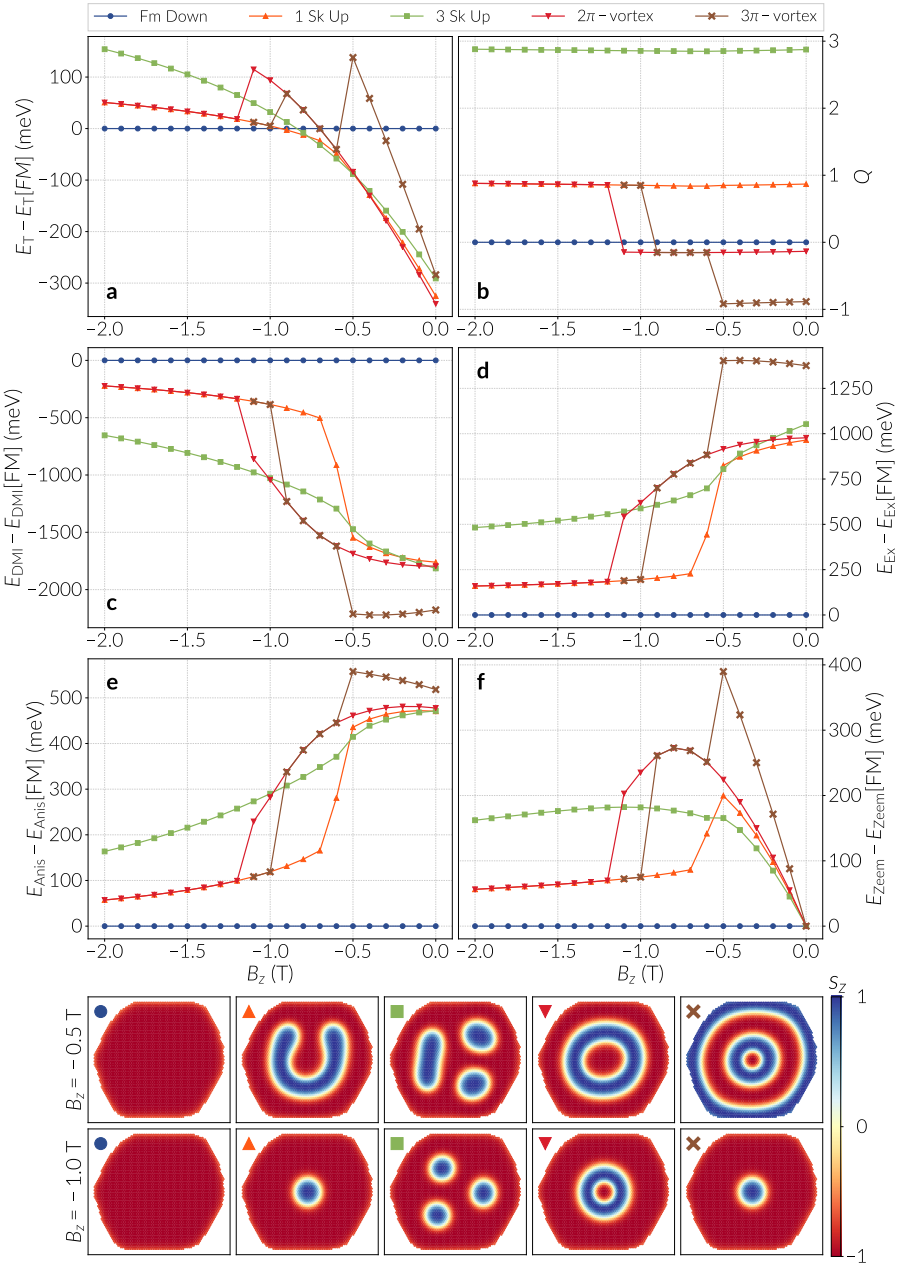


**Characterisation of skyrmionic textures in hexagonal islands.** Summary of the magnetic energies and topological charge of five different magnetic configurations: ferromagnetic ordering in the $-z$ direction (FM down), a single skyrmion with its core in the $+z$ direction (1 Sk Up), three skyrmions (3 Sk Up), a target state or $2\pi$-vortex, and a $3\pi$-vortex. Snapshots of these states under a field of $B_z = -0.7$ T and $B_z = -1.0$ T, are shown at the two bottom rows of the figure, where the colour scale refers to the out of plane spin component $s_z$. Every plot is shown as a function of the applied magnetic field, which points in the $-z$ direction of the sample. Energies are computed with respect to the ferromagnetic state for corresponding magnetic field magnitudes. (a) Total energy. (b) Topological charge. (c) Dzyaloshinskii-Moriya interaction energy. (d) Exchange interaction energy. (e) Anisotropy energy. (f) Zeeman interaction energy.

Figure 4.4

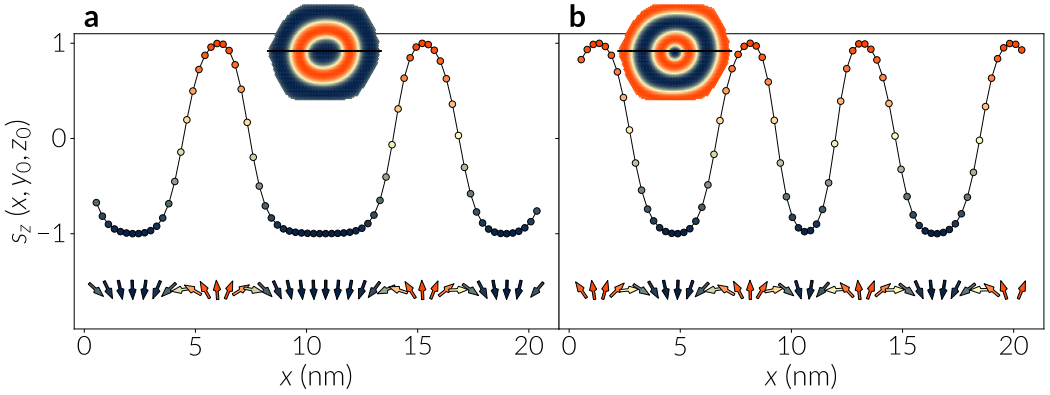


Figure 4.5 **Vortex states in hexagonal islands.** Spin field profile of vortex states in hexagonal islands, obtained by plotting the out of plane component of spins $s_z$ along a line passing through the centre of the sample located at $(x_0, y_0, z_0)$. These magnetic configurations shown in the figure are stabilised under a field of $B_z = -0.5$ T. At the bottom of every curve we show the spin (Néel like) orientations, which lie in the $xz$ plane. (a) $2\pi$-vortex. (b) $3\pi$-vortex.

due to the small tilting of the spins at the boundaries. For a single skyrmion $Q \approx 1$ and three skyrmions have $Q \approx 3$. This magnitude is positive for a rotation pointing outwards from the skyrmion centre. However, these magnitudes are similar when we have domains. For instance, observing the bottom row of Fig. 4.4 at a field $B_z = -0.5$ T, a single skyrmion looks as an elongated domain because the system found this was a lower energy state. We notice that although this elongated domain has the same topological charge of $Q \approx 1$, it is different from a skyrmion because of the jumps in the energy graphs below a field of $B_z = -0.5$ T. This is less evident when there are three skyrmions because only one of them is deformed and it has a more restricted area to expand within the island. In addition, the energy curves for the three skyrmion configuration is smoother though it is still possible to see a small jump. For the vortex configurations, it is not possible to use $Q$ to identify them. The reason is that a target state has two rotations with opposite orientation (see Fig. 4.5a) thus $Q \approx 0$, which is the same for different helicoidal states. In addition, a $3\pi$ vortex has an extra rotation facing inwards from its centre (see Fig. 4.5b), making $Q \approx -1$ which is also valid for a skyrmion with its core pointing in the $-z$ direction.

We analyse the total energy of the five configurations for different field magnitudes in Fig. 4.4a, where the field is applied in the $-z$ direction. The energy values are computed relative to the energy of the uniform state for corresponding field values. At weak fields, $|B_z| < 0.5$ T, the system prefers multiple rotations of the spins, hence the ferromagnetic ordering is a metastable state with the largest energy.

Regarding the single skyrmion (▲) and triple skyrmion (■) states, we can see that they are the most robust non collinear states against the applied magnetic field since although they deform at small fields they preserve their total topological charge $Q$ at

any field value. As the magnetic field strength increase, the size of the skyrmions is reduced, which is in agreement with the tendency in Ref. [58], and their shape becomes more symmetrical. This is especially the case for three skyrmions since they interact less with the surrounding boundary and other skyrmions.

For a single skyrmion we note from the energy of the interactions, depicted in Fig. 4.4c-f, that it turns from an elongated domain into a skyrmion at $B_z = -0.5\,\mathrm{T}$. We found this by relaxing the system with a very small tolerance (see simulation details in Section 4.5) since for weak tolerances we observed that the skyrmion relaxed to a circular bubble-like domain whose energy keeps the tendency shown by the curves from $B_z = -2.0\,\mathrm{T}$ up to $-0.7\,\mathrm{T}$, with no sudden jumps. Close to a field of $B_z = -0.8\,\mathrm{T}$ a single skyrmion (which is observed below $B_z = -0.5\,\mathrm{T}$) has lower energy than three skyrmions in the sample, partially due to the Zeeman energy which is smaller for a larger ferromagnetic environment in the direction of the applied field. This is evident from Fig. 4.4f where the Zeeman energy keeps increasing from $B_z = -0.5\,\mathrm{T}$ down to $B_z = -1.0\,\mathrm{T}$ for three skyrmions and only decreases for a single skyrmion in the island. The role of the Zeeman interaction for the triple skyrmion state is supported by the tendency of the DMI energy, which becomes less important when skyrmions get smaller with larger field magnitudes.

Two other physically interesting states are the $2\pi$ (▼) and $3\pi$ (×) vortices, which have been theoretically predicted [31] but up to now have not been experimentally observed in bulk or interfacial systems. In particular, the presence of target states in confined systems has been recently identified for cylindrical geometries [66,91,137]. For the hexagonal islands we have obtained these multiple-rotation orderings defining the direction of their inner core in the $-z$ direction, which follows the applied field orientation. The spin fields for the two vortex states are depicted in Fig. 4.5, where spin orientations lie in the $xz$ plane and it is evident the typical Néel profile for the spin rotations.

According to Fig. 4.4a, the $2\pi$ and $3\pi$-vortex states are only stable in a small range of field magnitudes. Specifically, starting from zero applied field, the $2\pi$-vortex is observed down to a field of $B_z = -1.1\,\mathrm{T}$ and then the system relaxes to a skyrmion for lower fields, which is evident from the topological charge in Fig. 4.4b. For the case of the $3\pi$-vortex, it is visible even in a smaller range, only down to a field of $B_z = -0.5\,\mathrm{T}$, and afterwards it relaxes to the target and skyrmion states. It is noteworthy that the multiple spin rotations of the $2\pi$-vortex with a large enough ferromagnetic background make this configuration the lowest energy state between the five orderings we are analysing. The uniform surrounding of spins is important because it decreases the overall exchange energy. For fields above $-0.5\,\mathrm{T}$, where both vortex states are defined, we can explain this effect if we refer to the exchange and DMI energies depicted in Fig. 4.4d and 4.4c, respectively, which are the main energy contributions. Even if the DMI energy of the $3\pi$-vortex is significantly smaller than the $2\pi$-vortex, which is caused by the extra twisting of the spin field, the effect of the exchange interaction is large enough to make the

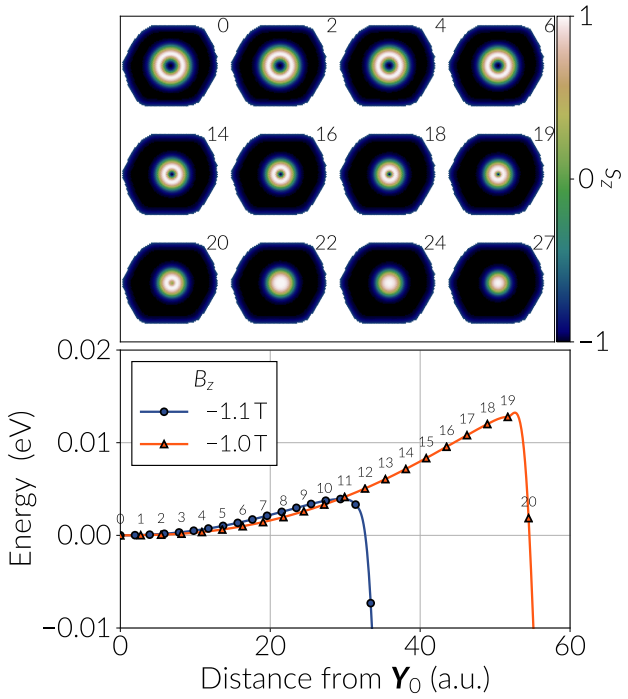


Figure 4.6 **Target state collapse into a skyrmion.** Minimum energy path between a target state and a skyrmion in a Pd/Fe/Ir(111) island for two external field magnitudes. The curve in the lower plot refers to the energy bands for two different external fields shown in the plot legend. The energy bands are only shown for their first few images. The energy scale is shifted with respect to the target state ($2\pi$-vortex) energy. The figure at the top shows snapshots of the images for the $B_z = -1.0\,\mathrm{T}$ case, where the numbers at every snapshot correspond to the numbers in the data points of the curve. The colourmap refers to the out of plane component of the spins.

total energy of the $3\pi$-vortex larger. This phenomenon is enhanced by the anisotropic energy (see Fig. 4.4e), which behaves similarly to the exchange energy at smaller magnitudes, and the Zeeman interaction (see Fig. 4.4f), which exhibits large energy magnitudes due to the spin rotations that make spins opposite to the field in a large area of the island. For fields below $-0.5\,\mathrm{T}$ the $3\pi$-vortex no longer exists and, in general, the target state energy is similar to the configuration with 3 skyrmions, probably due to a similar number of rotating spins in the sample.

### 4.3.1. Stability of target states in hexagonal islands

In Section 4.3 we observed that target states in Pd/Fe/Ir(111) islands could not be stabilised below a field of $B_z = -1.1\,\mathrm{T}$, where the system relaxes to an isolated skyrmion. One possible reason for this instability is that the energy barrier separating these two configurations is reduced as the magnetic field becomes stronger, thus a target state would decay below a critical field. Under this hypothesis we perform a stability calculation between a target state and a skyrmion by means of the NEBM. We set the target

state and the skyrmion as the initial and final state in an energy band, respectively, and initialised the energy band with a linear interpolation. The resulting energy band after relaxation is depicted in Fig. 4.6 for two different magnetic fields, $B_z = -1.1\,\mathrm{T}$ and $B_z = -1.0\,\mathrm{T}$. We confirm from this figure that the energy barrier decreases as we increase the magnetic field magnitude. At the top of Fig. 4.6 we show snapshots for the images of the band with $B_z = -1.0\,\mathrm{T}$ whose curve is numbered. The sequence shows a collapse of the target state into a skyrmion, where the saddle point is given when the inner core of the target state reverts to give rise to the skyrmion core which points in the $+z$ direction. Since we could not relax a target state at $B_z = -1.2\,\mathrm{T}$ (it might be possible using a weak tolerance for the relaxation of the target state), the critical field must lie between $B_z = -1.1\,\mathrm{T}$ and -1.2 T. For a field of $B_z = -0.9\,\mathrm{T}$, which we do not show here, we saw that the energy barrier is significantly larger, around 0.05 eV, although the transition is mediated by a singularity rather than by a collapse. As we observed in Chapter 3, we expect that the energy path given by a singularity is not a true first order saddle point, thus the algorithm might find the target state collapse after applying the climbing image method to the result for $B_z = -0.9\,\mathrm{T}$. This analysis requires further investigation in the future.

### 4.3.2. Field sweep in hexagonal islands

From the relaxation of the skyrmionic textures of Section 4.3 we obtained a general view of the range of magnetic fields where those configurations can be stabilised. A different technique is to perform a field sweep similar to a hysteresis process. In a collaboration with the group of Roland Wiesendanger from the University of Hamburg, Romming et al. have performed a field sweep on Pd/Fe/Ir(111) hexagonal islands (shown in Fig. 4.3a) and measured the magnetic configurations by SP-STM imaging. Their experimental results are shown in Fig. 4.7 where the contrast refers to the non-collinearity of the configurations. The process start with a spin spiral and the island saturates at 4.0 T. We can distinguish skyrmions from frames b-f and g. When decreasing the field, in frame g there is an extra skyrmion which was probably excited because of temperature effects or the bias voltage from the SP-STM tip. helicoidal structures with multiple branches from the h frame and onwards, after passing the zero-field step.

To reproduce the experimentally observed configurations with our code, the difficulty lies on choosing an adequate initial configuration since, normally, it is not possible to know every possible equilibrium state. In particular, helicoids are hard to analyse because they can manifest as branches, *i.e.* long domains oriented in the $+z$ or $-z$ direction, that can be oriented in any direction in the island. Correspondingly, we selected five magnetic orderings based on different number of skyrmions and the configuration from Fig. 4.7b-c where a skyrmion and a helicoid coexist next to each other. To set our starting point in the hysteretic-like analysis, we relax these configurations at a magnetic field of $B_z = -2.5\,\mathrm{T}$, which are the states in the first row of Fig. 4.8. As we

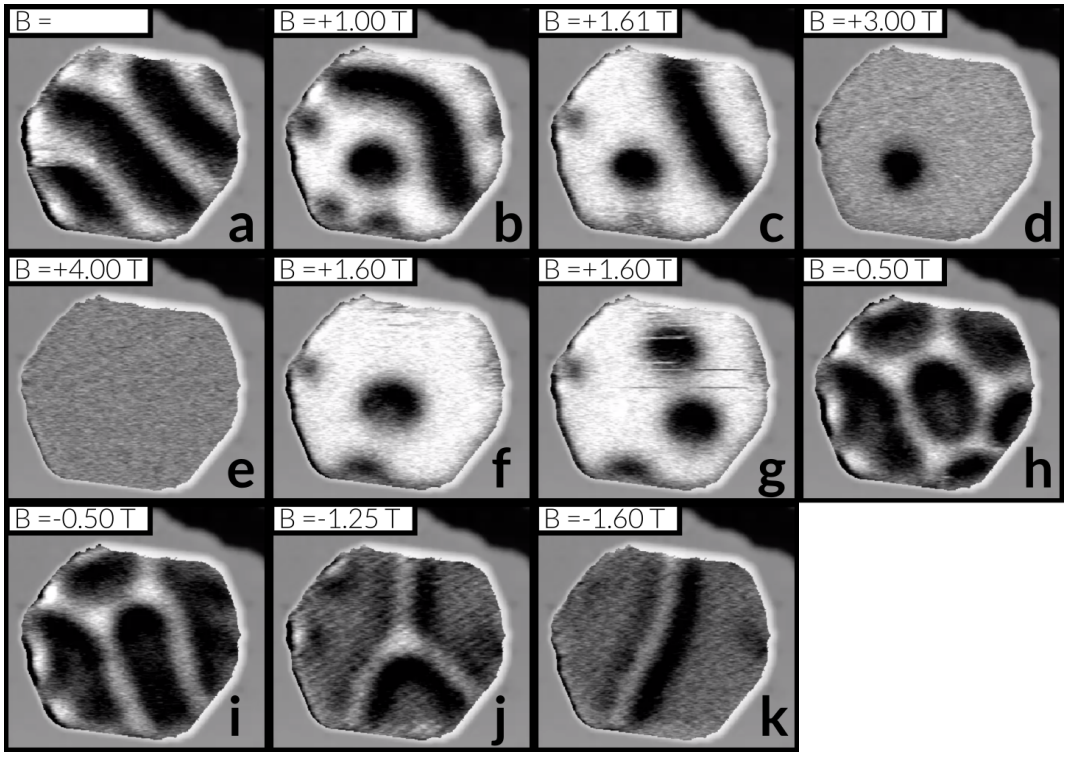


Figure 4.7 **Experimental observation of magnetic textures in hexagonal islands.** Images obtained using SP-STM during an external field sweep on Pd/Fe/Ir(111) islands. Measurements were performed by the group of Roland Wiesendanger at the University of Hamburg (see Section 4.6). Colour contrast indicates the non-collinearity of the spin field.

mentioned in Section 4.3, these orderings can be directly characterised by their topological charge and, effectively, we see in the first row of Fig. 4.8 that $Q$ indicates the number of skyrmions in the sample and for a helicoid $Q \approx 0$ because it only has spins rotating in a single direction. We then increase the magnetic field in 100 mT magnitude for every initial state and relax each system again. We repeat this process up to a field of $B_z = 2.5$ T and register the resulting configurations under equilibrium for every step where the field is increased. As a result, we obtain the evolution of every initial state given by the columns of Fig. 4.8 and 4.9, where we only show snapshots of the relaxed states in steps of 500 mT. We observe that as we reach the zero field step skyrmions try to expand and occupy a large area in the sample and in particular, when there is a large number of skyrmions, as the case of column A in Fig. 4.8 at zero field, these configurations appear more symmetrical since they occupy the available space more optimally through a hexagonal arrangement which is typical of skyrmion lattices. Consequently, as we pass the zero field step we start observing interesting chiral configurations which critically depend on the initial state. When we start with different number of skyrmions we notice that domains oriented in the $+z$ direction appear surrounded by elongated domains pointing in the $-z$ direction in the form of branches whose ends tend to finish

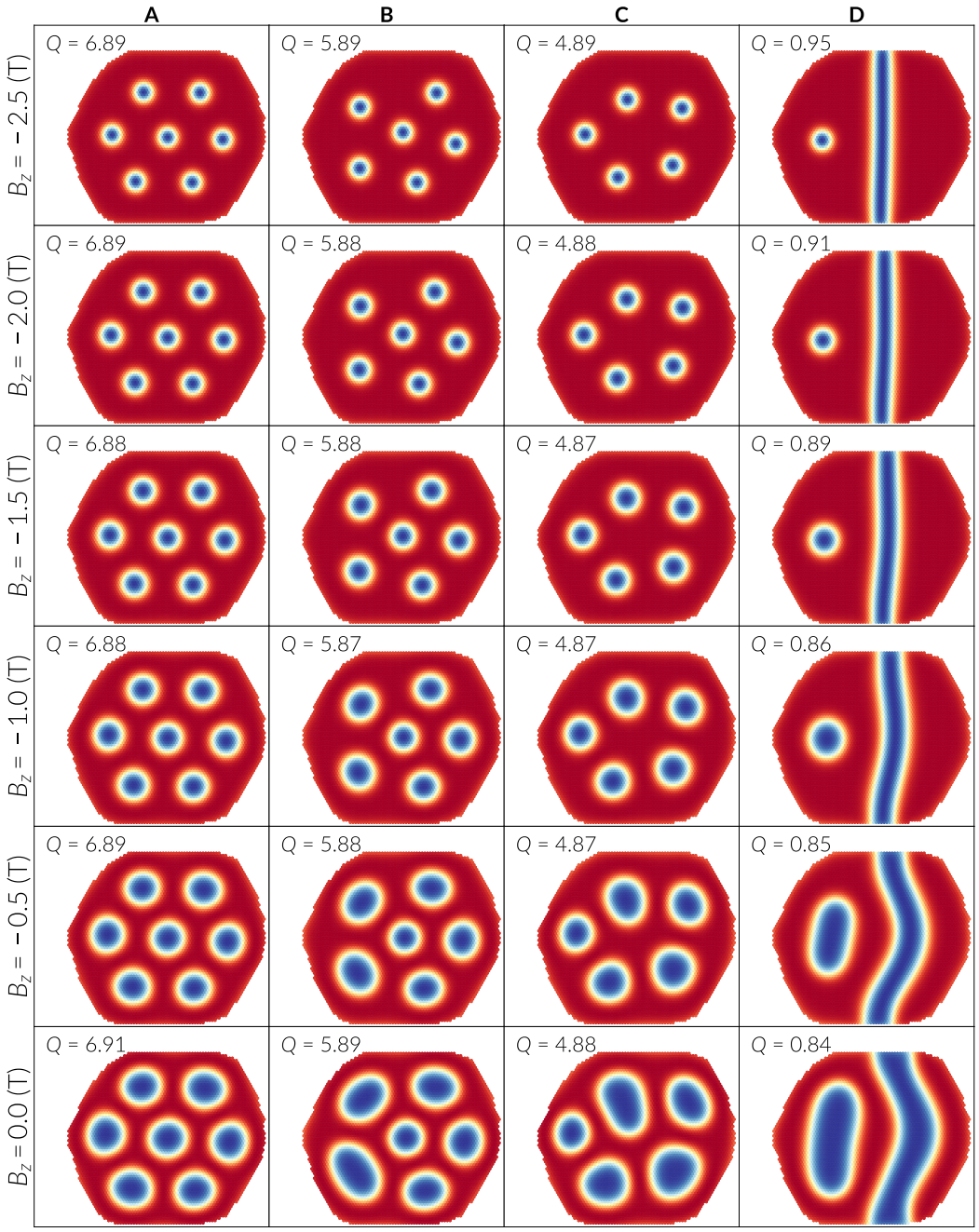


**Field sweep of magnetic orderings in a hexagonal island.** Snapshots of magnetic configurations obtained after relaxation during a field sweep, as in a hysteresis process, with a starting field of $B_z = -2.5\,\mathrm{T}$. Columns indicate the field variation process for different initial states. The field sweep was computed in steps of 0.1 T, with this figure only showing the resulting orderings in steps of 0.5 T. The field magnitude is depicted at the left side of every row, where all the snapshots are shown at the same field value. The top left number at every snapshot plot refers to the topological charge of the system. The colour scale indicates the out of plane component of spins which is the colour scale of the snapshots in Fig. 4.4.

Figure 4.8

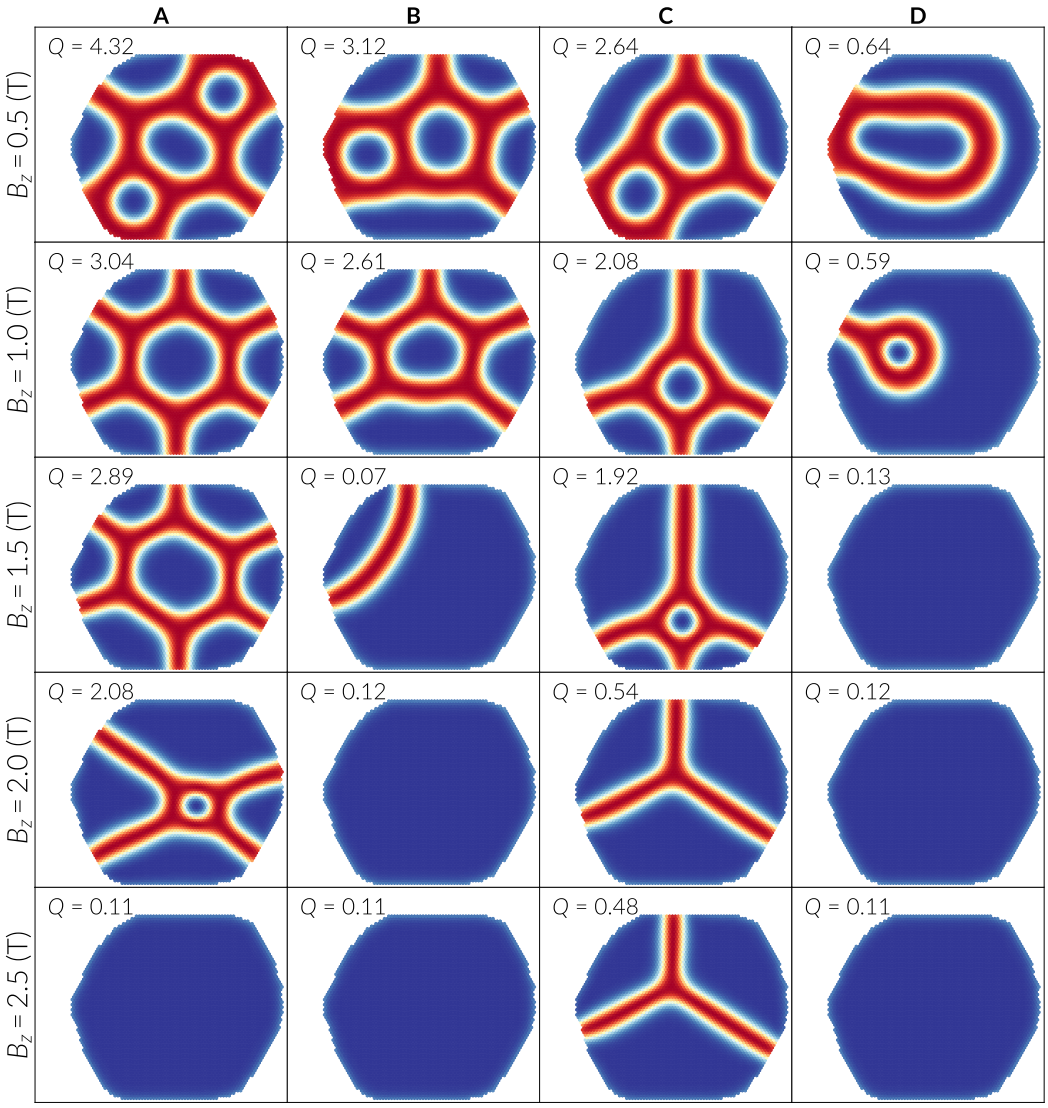


Figure 4.9 **Field sweep of magnetic orderings in a hexagonal island.** Continuation of the field sweep process explained in Fig. 4.8. Field magnitudes for this case are psitive and larger than zero field, thus the field is oriented out of plane in the $+z$ direction.

perpendicular to the hexagon sides rather than the corners. These enclosed domains carry a topological charge of $+1$ since their surrounding domain wall are equivalent to the skyrmion boundary. While some of the skyrmionic structures are partially destroyed at the boundary of the island, the total number of domains in the $+z$ direction is the same as the number of initial skyrmions, which is evident from columns A-C of Fig. 4.9 at fields of 0.5 and 1.0 T. As expected, these incomplete skyrmionic domains do not have an (approximately) integer topological charge and it is possible to roughly estimate this magnitude depending on the domain shape.

Referring to column A of Fig. 4.9, at $B_z = 0.5$ T we have a skyrmionic domain which contributes $Q = 1$ and four incomplete domains that can be identified with $Q \approx 1/3$,

approximately summing up the total charge $Q$. We estimated a 1/3 charge because the incomplete domains sit at a corner of the hexagonal island which forms a $2\pi/3$ angle, thus making a third of a full skyrmionic texture. On the other hand, if we now refer to the state of column C at the same field, the same argument cannot be applied to the more elongated boundary domains at the upper sides of the sample, where the more straight profiles of their surrounding domain walls are likely to give a small $Q$, hence we obtain a total charge of $Q \approx 2.33$ only considering the domain at the bottom right of the island, being the actual total charge $Q = 2.64$. However, we still have to consider the spin tilting at the boundaries, which can contribute up to $Q \approx 0.13$, as seen in column D at 1.5 T for a uniform ordering in the $+z$ direction. For the state of column A at 0.5 T our $Q$ estimate is in agreement with the value from the simulation thus it is likely that the contributions from the boundary spins with a positive $z$ component cancel out with the spins with $-z$ component because they are almost in the same proportion. Regarding column C, the lacking 0.31 charge must be explained by the number of edge $+z$ and $-z$ spins, which seems to have a small positive contribution to $Q$, and by the small $Q$ from the two larger boundary domains at the top corners of the island, whose separating domain walls are not completely straight. These issues indicate that it is not straightforward to estimate the total topological charge but general arguments can be applied to the more symmetrical cases.

When we keep increasing the magnetic field further than 1.0 T the spin spiral branches start to dissapear or skyrmionic domains trapped within them reverse their orientation giving rise to more simple spiral structures. In general, these states at positive fields are the ones that most resemble the experimentally observed magnetic orderings of Fig. 4.7. For example, Fig. 4.7h is similar to column B of Fig. 4.9 at 1.0 T, where spirals end perpendicular to the hexagon sides. Similarly, we see the triple junction of Fig. 4.7j in column C of Fig. 4.9 at 2.0 T. The other single spirals have also been observed starting from other initial configurations. Although we do not show it here, we tried to replicate the exact loop of Fig. 4.7 starting from a spin spiral but we could only obtain a single spiral when increasing the field. Interestingly, at strong magnetic fields above 3.0 T the spiral became a single skyrmion before saturation.

Besides the ramified spin spirals from columns A-C of Fig. 4.9, there are other curious magnetic orderings such as the perfectly symmetric confined domain of column D at $B_z = 1.0$ T, which is close to a $2\pi$-vortex except for the tail ending up at the boundary of the island. This structure has been observed in experiment but for samples with an extra Pd layer on top.

## 4.4. Target states in Fe based hexagons

In our search for a range of parameters where target states can be stabilised, we analyse Pd/Fe/Ir(111) hexagons of different sizes. This can help as a reference for future

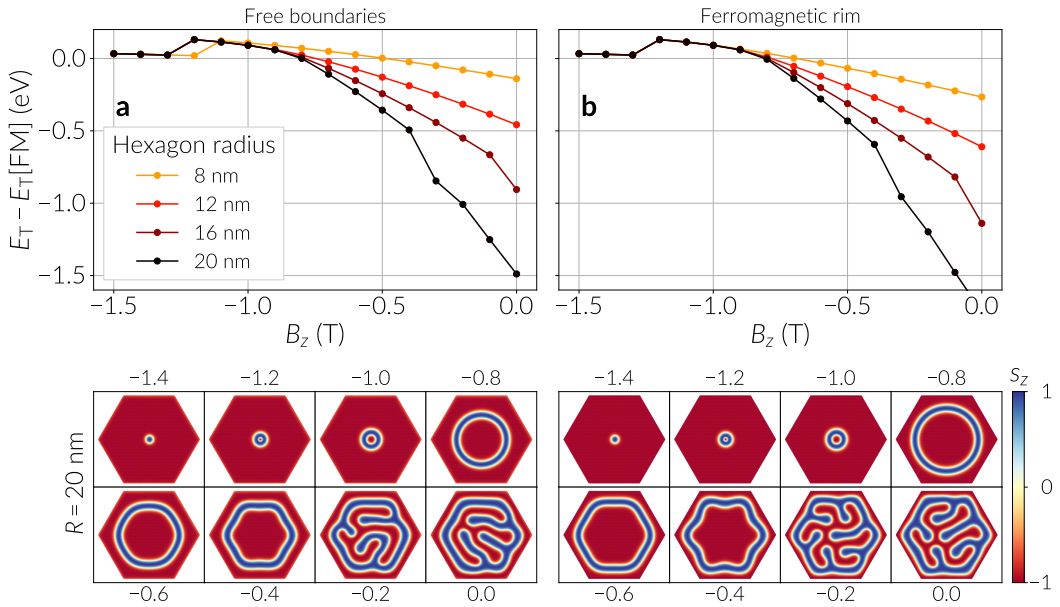


Figure 4.10 **Energy of target states in hexagons for two different boundary conditions.** The curves refer to the total energy $E_T$ of a target state as a function of the applied field, in Pd/Fe/Ir(111) hexagons of different sizes and boundary conditions. The hexagon size is defined by its *circumradius*. The energy is shown with respect to the energy of the ferromagnetic state for corresponding field values. Snapshots of the hexagons for a circumradius of $R = 20$ nm are shown below for the two plots, which indicate different boundary conditions. Magnitudes above or below snapshots specify the magnetic field $B_z$ and the colour scale refers to the out of plane component of the spins. (a) Energy of hexagons with free boundary conditions. (b) Energy of hexagons where spins are pinned in the $-z$ direction, making a ferromagnetic rim.

experimental measurements.

Following the methodology of Fig. 4.4, we initialise hexagon systems of different size with a target state ($2\pi$-vortex) and relax them for different field magnitudes. We characterise the size of the hexagons by their circumradius $R$ and the relaxation is done using the Landau-Lifshitz-Gilbert equation. Using four different circumradius, $R = 8,\ 12,\ 16$ and 20 nm, we summarise the computed energies in Fig. 4.10a, where energy values are relative to the ferromagnetic state in the $-z$ direction. In addition, for a radius of $R = 20$ nm, we show snapshots of the relaxed states at the bottom of Fig. 4.10a, for fields ranging from $B_z = -1.4$ T up to zero field in steps of 200 mT. We observe that at weak fields, increasing the size of the hexagon decreases its energy relative to the uniform ordering. If we observe the snapshot of the system at zero-field, we see a distorted domain where spins are oriented in the $-z$ direction and which favours the DMI energy. This warped domain is only observed for $R$ larger than 14 nm (simulations were performed for sizes in steps of 2 nm) and the shape of the domain varies according to the hexagon size. As we decrease the field below $-0.2$ T, we start noticing the target state which becomes more symmetric and smaller in size with stronger fields. This oc-

curs down to a field of $B_z = -1.2\,\mathrm{T}$ approximately, where the target state is no longer stable and the system relaxes to a skyrmion. Only for $R = 8$ nm the target state is stabilised down to $-1.1\,\mathrm{T}$. Furthermore, at a field of $B_z = -0.8\,\mathrm{T}$ and for $R$ larger than 12 nm, the energy of the target states is larger than the uniform configuration and the energy curves follow the same tendency for lower fields. For smaller sizes of hexagons the ferromagnetic ordering is preferred at smaller field magnitudes.

The systems we have described so far were simulated with free boundaries, which causes a slight spin tilting at the sample edges. For the hexagons we modified this condition and fixed the spins in the $-z$ direction to analyse if the boundary conditions have some effect on the stability of target states. Our main motivation is the fabrication of islands with an extra Pd layer, i.e. Pd/Pd/Fe/Ir(111), obtained by the group of Roland Wiesendanger at the University of Hamburg (see Section 4.6). In this system, the overlayer of Pd is surrounded by Pd/Fe/Ir(111) which leads to a different boundary condition than Fe/Ir(111). For instance, at strong fields the surrounding material is ferromagnetic, leading to a coupling with the double Pd island. This new condition is thought to be one of the reasons for the observation of target state-like configurations in these systems. To simulate this effect computationally, we started by pinning spins at the boundary of our Pd/Fe/Ir(111) islands, creating a ferromagnetic rim. In Fig. 4.10b we performed the same analysis as in Fig. 4.10a, using different hexagon sizes and magnetic fields. Our results show that there are not significant changes compared to using free boundaries. We can see though that larger islands have even lower energies at weak fields and small sized hexagons decrease their energy for larger fields. In addition we observe that the $B_z = -0.8\,\mathrm{T}$ energy curve follows the tendency of larger systems and becomes unstable at $B_z = -1.2\,\mathrm{T}$ as well.

## 4.5. Simulation details

The atomistic simulations were performed using Fidimag [78]. To speed up the relaxation of the different magnetic systems studied in this chapter, we use the Landau-Lifshitz-Gilbert equation without the precessional term and set a damping value around 0.9. In addition, we set for the gyromagnetic ratio $\gamma = 1$ which only changes the time scale (we are not interested in dynamical effects, only in energy minimisation). Fidimag uses a time variable step method from Sundials [115] CVODE library, to integrate the Landau-Lifshitz-Gilbert equation. On every time step, we compute the largest difference between spins of the last step with respect to spins of the previous step, $\Delta\mathbf{s} = \max(|\mathbf{s}_{\mathrm{LAST}} - \mathbf{s}_{\mathrm{PREV}}|)$, and we divide this magnitude for the current time step $\Delta t$ given by the integrator. We stop the relaxation when this value $\Delta\mathbf{s}/\Delta t$ is smaller than a specified tolerance. A weak tolerance for the relaxation is about $10^{-4}$ and a strong tolerance is set for a magnitude around $10^{-6}$.

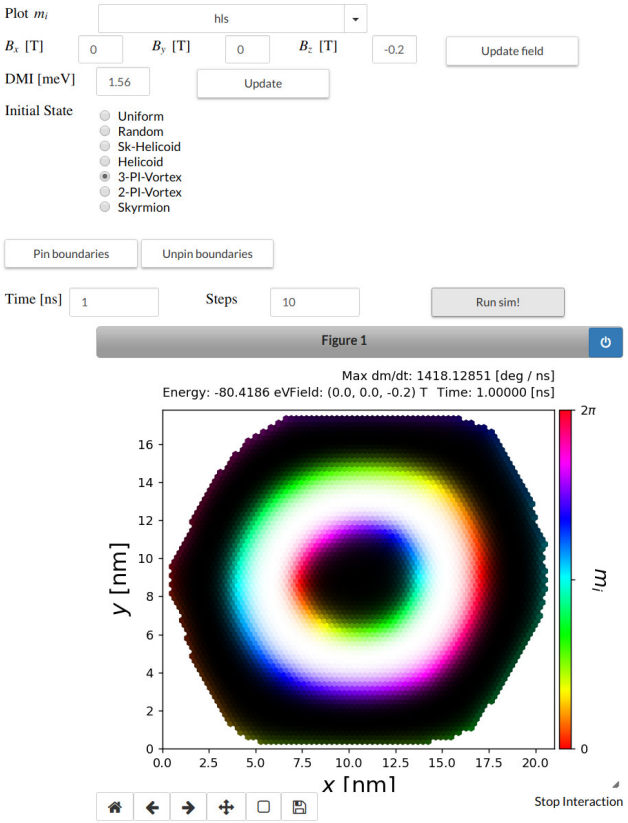


Figure 4.11 **Interactive widget for atomistic simulations.** View of an interactive interface for real time visualisation of atomistic simulations. The interface is based on Matplotlib's widgets library [138]. The system shown in the figure is a Pd/Fe/Ir(111) island which can be initialised with different magnetic configurations. Magnetic parameters such as the external magnetic field and the DMI strength can be updated by specifying values in the text boxes. Different colourmaps can be used for visualising the spin field components and the picture shows a HSL colour scale.

### 4.5.1. Simulation widget

At the beginning of our study we required a general idea for the stabilisation of a variety of magnetic configurations in the Pd/Fe/Ir(111) island shown in Fig. 4.3. To facilitate this process we developed an interactive interface for our atomistic simulations, which are implemented in Fidimag [78]. The interface was programmed using a library for creating widgets from the plotting tool Matplotlib [138]. This library allows to create buttons and text boxes to update variables in real time, which can be linked to Matplotlib's plotting tools. For recent versions of Matplotlib the widgets can take advantage of an interactive Matplotlib backend that works on Jupyter notebooks [139]. Therefore, using the modular and class based structure of Fidimag (see Chapter 5) it was possible to easily apply widgets to create real time visualisations of the simulations. In Fig. 4.11 we show an image of the simulation widget in a Jupyter notebook, where it is possible to set different initial magnetic configurations and update the magnetic field to relax the

system for an specified time. Furthermore, there are different colourmaps to visualise the components of the spins. In Fig. 4.11 a target state is visualised using an HSL colour model which indicates the spin orientation in plane and the out of plane component in a black and white scale, allowing the observation of a full view of the three dimensional spin field into a two dimensional map. This code can be extended to update any magnetic interaction, such as the DMI which is shown in Fig. 4.11, or to simulate any magnetic system with Fidimag. The simulation widget has been useful to explore the system and start defining a methodology to characterise magnetic textures on these ferromagnetic islands. Currently the code is hosted in a private repository and will be eventually released as open source when results from this chapter are published.

## 4.6. Experimental data

Experiments discussed in this chapter are based on SP-STM imaging of Pd/Fe/Ir(111) and Pd/Pd/Fe/Ir(111) islands, performed by N. Romming, K.v. Bergmann and A. Kubetzka, who are part of the group of Roland Wiesendanger from the Institute of Applied Physics and Interdisciplinary Nanoscience Center Hamburg, University of Hamburg. Experimental data shown and referenced in this chapter was taken from permission of R. Wiesendanger group. Ideas from the analysis of simulations with experimental results are product of this collaborative project.

## 4.7. Discussion

Using atomistic simulations we have been able to characterise magnetic configurations in Pd/Fe/Ir(111) systems by varying their size, the applied magnetic field and boundary conditions. Performing a field sweep on hexagonal islands, as has been done experimentally, we can reproduce some of the magnetic states observed in laboratory, although not at similar magnetic fields since our simulations are based on a theory at zero temperature. In addition, our analysis has been mostly focused on specifying a range of parameters to observe target states and our results show that they can be stabilised at weak magnetic fields. By applying the NEBM on hexagonal islands simulated from experiments, we could justify that target states cannot be stabilised below a critical field since the energy barrier decreases for strong field magnitudes. Using perfectly hexagonal lattices, we noticed that target states, at weak fields, decrease in energy when increasing the size of the hexagons and the effect is more intense when setting ferromagnetic boundaries. It is worth mentioning that for larger sizes, dipolar effects, which are not considered in our model (only as an effective anisotropy), are likely to have a noticeable influence on the domains and maybe the stabilisation of target states, thus future analysis on larger islands should consider this.

When we implemented fixed boundary conditions on hexagons, our motivation was to replicate the different edge condition when an extra palladium layer is added to the

Pd/Fe/Ir(111) islands. For further exploration on the double Pd systems we could use more accurate magnetic parameters for the islands. For example, *ab-initio* calculations for these systems would be useful to obtain parameters that can be compared to experiments on finite sized islands with a ferromagnetic boundary. In Table 4.1 we show values computed by Dupé et al. [135] for a double layer of Pd on Fe/Ir(111) which can be used as a starting point to compare with the available experimental data.

The results obtained in this chapter are still an ongoing collaboration with the experimental group. Besides the hexagonal islands we studied, Romming et al. (see Section 4.6) have also fabricated truncated triangles using double Pd layers and observed target state-like configurations on them. Applying the techniques we described in this chapter we can continue the study on these truncated triangles and consider new effects. For instance, it is possible to tune their geometry to analyse if the shape has an influence on the stability of different magnetic textures.

# Reproducible computational science

Chapter 5



The act of observation is inherent to the scientific method in natural sciences. In traditional research the observation of natural phenomena is made directly through experiments and appropriate instrumentation, however, since the middle of the last century the creation and fast development of computers have allowed new methods for observation and prediction through numerical calculations. Initially, numerical computations were used to obtain solutions for complex theoretical problems whose equations cannot be tackled analytically, or to analyse experimental data [140]. Modern research, on the other hand, has allowed the development of computer based experiments for problems that cannot be reasoned analytically or are inaccessible to experiment. [141, 142], where numerical results are compared to traditional observation and hardware and software to the instrumentation and methods for observation [142].

With the popularity of research based computational simulations, the issue of *reproducibility* has come to be questioned. This term refers to the possibility that experiments and results from research could be repeated under different conditions. Reproducibility has been in general a topic that has been criticized in multiple scientific fields [143] and is essential for the verification and credibility of published works. Moreover, science is a social endeavour where knowledge is built from findings of different groups, thus reproducible science is critical to improve and promote novel and high quality research. In order to improve reproducibility, it is natural to make research transparent and accessible to others, hence open science has also been a strongly debated topic, especially within scientific journals. Accordingly, accessibility to data or computational code used in a paper has started to be a requirement for publishing [142, 144–146].

In the context of computational based research, the discussion of reproducibility started in the nineties and was identified as "a way of organizing computational research that allows both the author and the reader of a publication to verify the reported results" [141]. Recently, in an extensive analysis on reproducibility and best practices for numerical experiments, Fehr et al. [142] argue about three main ideas to help establishing scientific software within open science practices: (i) replicability, (ii) reproducibility and (iii) reusability. Proper documentation of the code and the methodology applied in the computational experiment benefit all three ideas of Fehr et al. Furthermore, open sourcing the software is recommended since it is crucial for (i) and (ii), especially because the code would be available for reviewing and verification by others [144, 145]. Besides the

evident benefits of open source, it does not imply quality in a scientific software since a well developed code requires documentation, debugging, testing, installation methods, etc. which, in the current research model, are tasks that are not as valuable as writing and publishing papers [141, 147, 148]. Nevertheless, with the increasing dependence of contemporary science on software, efforts have been made to set up standards for making scientific software citable [148] and different institutions have started to support research software practices [141], giving computational science more credit.

In the following sections we explain two open codes we have developed to obtain the results discussed in this thesis and which are compatible with the computational practices suggested by Fehr et al. [142] for open science. The first is a major software project called Fidimag that we use to perform atomistic and micromagnetic simulations. The other is a series of scripts that we used to obtain the results of Ref. [1], making its results completely reproducible.

## 5.1. Fidimag

Fidimag is a program to simulate magnetic systems using micromagnetics, where computations are based on the finite differences numerical method, or atomistically, where simulations use a Heisenberg like discrete spin model. It was originally developed by Wang [73] in 2015 and later the code was refactored, improved with new features and registered under a DOI address in Ref. [78] for citation [148]. The code is written in the C language with an interface using Python. It is hosted in Github and is open source under a 3-clause BSD license, thus making reproducibility [142] feasible for results obtained through this software.

According to good coding practices, documentation is provided for installation, general functionalities of the software and underlying theory for the calculations in [116]. Moreover, documentation through extensive comments for the functions and methods are directly written in the source code. The code has been structured in a modular fashion: magnetic interactions, magnetic dynamics and system specifications, either if it is micromagnetic or atomistic, are separated in their own libraries and methods, facilitating reusability [142] and extension of the software. These features are supported by multiple unit and integration tests [142] which check that methods work as expected, results are compatible with theory and that any modification to the software keeps it consistent.

## 5.2. Reproducible publication

At the conclusions of Chapter 3 we stated that all the results from the study could be reproduced from Ref. [131]. This repository contains a series of files that automatise the process of running the simulations used in Ref. [1] and generating the corresponding

data. The automatisation is achieved through multiple `Makefile` scripts but, in particular, by a Docker script that installs Fidimag.

Docker [149] is an user friendly open source tool to create a virtual environment based on the Linux operating system kernel, which has many interesting features for scientific reproducibility [150]. One of the advantages of creating these environments or *containers* is solving software dependency issues[1] that are commonly found when running a code in a different environment from where it was originally programmed, for example in different computers or operating systems. In a Docker container, which is defined by a file called *image*[2], the software is already installed and configured, and a Docker image can even store data files from research to facilitate data distribution [150]. This approach gives a significant benefit to small software projects where code maintainability is expensive [141], and works perfectly for reproducibility because a container can be easily distributed to any machine where Docker runs, giving other people the possibility to easily obtain the numerical outcomes from computer based research.

For the case of Ref. [131], the Docker container is created by a small piece of code called `Dockerfile`. In this file, it is specified that an `Ubuntu 16.04` operating system environment is created in order to install all the necessary dependencies for Fidimag [78]. Along this file there is a `Makefile` that provides the `relaxation`, `nebm` and `plot_nebm` commands to relax a skyrmion or a uniform configuration in a nanotrack system using the Landau-Lifshitz-Gilbert equation, evolve a skyrmion-ferromagnetic transition with the NEBM and plot the NEBM data, respectively, for a specific DMI magnitude given by the environment variable `DMI` (which is specified as the micromagnetic equivalent in $10^{-4}\,\mathrm{J\,m^{-2}}$, for example, setting `DMI=32` it means that we run the simulation with $D = 0.721\,\mathrm{meV}$). On top of these scripts, there is another `Makefile` that automatically executes all the simulations specified in Ref. [1], allowing a user to to simply type in a terminal `make run_all`, provided that Docker is installed on the system. All these scripts and a detailed documentation of their functionality and the simulation results, are hosted in the Github repository linked to [131].

[1] This means dependency on external programs and libraries that, when they are updated, can break the functionality of the main code.

[2] A Docker image is an immutable set of instructions, programs and files structured in layers. When a Docker container is created, it uses an image and adds an extra layer for writing and deleting data. For more information see Docker [149] documentation.

# Chapter 6

# Conclusions

In this thesis we have applied computational simulations to study the properties of complex chiral magnetic configurations in different nano-scaled ferromagnetic systems where Dzyaloshinskii-Moriya interactions (DMI) are present. In addition, we have focused on the study of the thermal stability of magnetic structures using numerical methods. Thermal stability of a magnetic configuration means a measure of its robustness against random thermal fluctuations, which are present in systems at finite temperatures. In this case, it is relevant to quantify the stability at room temperature for any potential application of a magnetic structure in a technology or device.

For the study of thermal stability of magnetic systems we have implemented a numerical method called the Nudged Elastic Band Method (NEBM) in an open source package for atomistic and micromagnetic simulations Fidimag [78], which we have developed collaboratively in our group. This algorithm can be used to compute transition paths and energy barriers between two equilibrium states of potentially any magnetic system described by a discrete Heisenberg-like atomistic model or by the continuum theory of micromagnetics. The energy barrier between two stable configurations is the energy necessary to apply to the system (*e.g.* by means of temperature) to drive one of these states into the other. The barriers can be used to estimate the lifetime of the magnetic states, which is crucial for technological applications, for example, if these states are used as information units.

We have applied the NEBM to analyse the thermal stability of skyrmions in thin racetracks or mono-layered systems where no magnetic field is required for their stabilisation. Skyrmions are magnetic structures with non-trivial topology that arise as equilibrium states in magnetic systems with DMI. Skyrmions are of interest for magnetic recording technology because their topology grants them an extra stability. As a result, they are manipulable structures that can be applied, for instance, as information carriers in racetrack-like memories [121]. Nevertheless, the thermal stability of skyrmions in finite sized systems at zero applied field, which is important for an energy efficient technological application, has only recently started to be understood and quantified using theoretical methods. In our study we estimated the thermal stability of skyrmions by computing energy barriers associated to their destruction or nucleation mechanisms. Accordingly, we found three different transitions for the skyrmion destruction (nucleation): annihilation through the boundary, skyrmion collapse and destruction via a sin-

gularity. The transition with least energy cost is the one mediated by the sample edges and the energy cost associated to this process is significantly smaller than the energy involved in transitions of current technologies such as perpendicular magnetic recording. This result strongly suggests that, for the skyrmion application on nanotrack based devices, it is necessary to devise novel engineering methods to avoid the skyrmion escape through the sample boundaries or to further explore materials and systems hosting skyrmions that enhance their stability. Furthermore, we argued that the so called topological protection of skyrmions is a weak concept in a discrete model since there is always a finite energy barrier separating the skyrmion structure from other equilibrium states and, in addition, in a finite sized sample this protection is circumvented by the destruction mechanisms via the boundary of the system. These results have been published in Ref. [1].

In our analysis of skyrmions in thin films we showed the effects of the demagnetising field on the size of skyrmions. In very thin samples it is possible to approximate the effects of dipolar interactions by an uniaxial anisotropy, however this requires knowledge of effective anisotropy constants that account for the stray field influence and these parameters are not usually given in the literature. Otherwise, it is possible to perform a full calculation of the demagnetising field which, numerically, is computationally expensive. Moreover, for thin samples we found a discrepancy in skyrmion sizes when converting their magnetic parameters from the micromagnetic to the atomistic model and we realised this effect is caused by the dipolar interactions. We think the problem stems from the assumptions made when deriving the demagnetising field in the continuum from the discrete spin model. In this context, the small dimensionality along the thickness might have an important role since the continuum approximation is not valid for systems made of a few monolayers. Our results on this topic are not conclusive, hence we suggested ideas that can lead to a future study to find a correction factor or explanation for the agreement of magnetic structures when using atomistic and micromagnetic simulations with dipolar interactions.

We started a collaboration with an experimental group from the University of Hamburg to apply our computational simulations software to analyse non-colinear configurations in Pd/Fe/Ir(111) nano-sized islands. The magnetic structures in these islands have been probed by the experimentalists using spin polarised scanning tunneling microscopy (SP-STM). We described their observations by applying the discrete spin model and replicating a magnetic field sweep as done in the experiments. As a result, we obtained multiple experimentally observed helicoidal structures, although at different magnetic fields because our simulations are performed at zero temperature and experiments at finite temperature. Furthermore, simulations allowed us to stabilise other magnetic configurations with cylindrical symmetry, such as $3\pi$ and $2\pi$ — vortexes, which are skyrmion-like textures with extra spin rotations. It is worth mentioning that, at weak magnetic fields, the confined geometry of the islands is important for the stabilisation

of the skyrmionic textures since they tend to occupy a large area of the sample. For the case of the vortex states we found that they can be stabilised in a small range of magnetic field magnitudes and are energetically favoured close to zero field. This result can guide future experiments for the observation of these vortex states which, until now, has not been achieved. Additionally, we analysed the stability of the $2\pi$-vortex state to explain why they are not stabilised above a specific applied field magnitude. The reason is that the energy barrier separating this state with an isolated skyrmion decreases as the field magnitude increases. To analyse other effects on the stability of vortexes we modified the sample geometry and changed the boundary conditions, nonetheless we did not find any significant outcomes. This study is an ongoing project thus our results are still under discussion. We believe our findings are important to understand the stabilisation of other chiral orderings besides skyrmions in thin confined systems and that future experiments can prove our theoretical observations.

Finally, we dedicated a chapter on the discussion of good practices for scientific coding and data sharing. In modern research, computational based studies have become a standard technique for the verification and prediction of physics phenomena in complex systems. Following these practices, we showed two examples of computer software that we developed for the studies of this thesis.

# Magnetic moment

Appendix

A



## A.1. Orbital angular momentum

If we define a tiny loop of current $\mathcal{I}$, under the influence of an external field $\mathbf{B}$, the force $\mathbf{F}$ exerted on an infinitesimal section of this loop $\mathrm{d}\mathbf{l}$ is

$$\mathrm{d}\mathbf{F} = \mathcal{I}\,\mathrm{d}\mathbf{l} \times \mathbf{B}\,, \tag{A.1}$$

and therefore, assuming a constant field, the torque is[1]

$$\begin{aligned}\boldsymbol{\tau} &= \mathcal{I} \oint \mathbf{r} \times (\mathrm{d}\mathbf{l} \times \mathbf{B}) \\ &= \left(\mathcal{I} \int_{\mathcal{S}} \mathrm{d}\boldsymbol{\mathcal{S}}\right) \times \mathbf{B} \\ &= \mathcal{I}\boldsymbol{\mathcal{A}} \times \mathbf{B}\end{aligned}$$

where $r$ is the position vector to the infinitesimal section, $\boldsymbol{\mathcal{A}} = \left(\int_{\mathcal{S}} \mathrm{d}\mathcal{S}\right)\hat{n}$ is the surface area enclosed by the current loop and $\hat{n}$ is the normal to this surface. Furthermore, from classical electromagnetism, it is known that the torque on a magnetic dipole moment $\mathbf{m}$ is $\boldsymbol{\tau} = \mathbf{m} \times \mathbf{B}$, thus we define the magnetic moment as

$$\mathbf{m} = \mathcal{I}\boldsymbol{\mathcal{A}}$$

If we now take the classical picture of an electron orbiting around a nucleus, which is Bohr's model of the atom, the current can be defined as

$$\mathcal{I} = \Delta q\, v_e = \frac{q_e}{2\pi R} v_e = \frac{(-e)(-v)}{2\pi R}$$

where $R$ is the radius of the orbit and $e$, $v > 0$ are the charge and velocity of the electron.

Choosing the origin at the nucleus for the position vector $\mathbf{R}$ (so $R$ is the radius) the angular momentum is normal to the area enclosed by the orbit, hence

$$\mathbf{L} = m_e|\mathbf{R} \times \mathbf{v}_e|\hat{n} = m_e R(-v)\hat{n}$$

[1] Expanding the triple cross product and using a variation of Stoke's theorem

We can now relate the angular momentum to the magnetic moment

$$\mathbf{m} = \frac{1}{m_e}\left(\frac{(-e)(-v)}{2\pi R}\right)(\pi R^2) m_e \hat{n} = -\frac{e}{2m_e}\mathbf{L}$$

An alternative and more formal derivation is given by Jackson [151] where, for any current distribution $\mathbf{J}(\mathbf{r})$, the magnetic moment is defined as

$$\mathbf{m} = \frac{1}{2}\int \mathbf{r}' \times \mathbf{J}(\mathbf{r}')\, d^3 r'$$

## A.2. Spin dynamics

Since spin is a quantum mechanical object, it is possible to use Eherenfest's theorem within the Heisenberg picture, for the time evolution of the expectation value of the spin operator $\hat{\mathbf{S}}$ as

$$i\hbar \frac{\partial \langle \hat{\mathbf{S}} \rangle (t)}{\partial t} = \left\langle \left[\hat{\mathbf{S}}, \mathscr{H}(t)\right] \right\rangle \tag{A.2}$$

where $\mathscr{H}$ is the time dependent Hamiltonian. For a time dependent external field $\mathbf{B}(t)$, we have[2]

$$\mathscr{H}(t) = \frac{g\mu_B}{\hbar}\hat{\mathbf{S}} \cdot \mathbf{B} \tag{A.3}$$

The spin operator follows the angular momentum algebra

$$\left[\hat{S}_i, \hat{S}_j\right] = i\hbar \epsilon_{ijk} \hat{S}_k \tag{A.4}$$

Therefore, we can prove that

$$i\hbar \frac{\partial \langle \hat{S}_i \rangle (t)}{\partial t} = \frac{g\mu_B}{\hbar}(i\hbar)\epsilon_{ijk} B_j \langle \hat{S}_k \rangle \tag{A.5}$$

which is basically

$$\frac{\partial \langle \hat{\mathbf{S}} \rangle}{\partial t} = -\frac{g\mu_B}{\hbar}\langle \hat{\mathbf{S}} \rangle \times \mathbf{B} \tag{A.6}$$

By defining $\boldsymbol{\mu} = -(g\mu_B \hbar^{-1})\langle \hat{\mathbf{S}} \rangle = -\gamma \langle \hat{\mathbf{S}} \rangle$, with $\gamma > 0$, we obtain the usual precessional term of the LLG equation

$$\frac{\partial \boldsymbol{\mu}}{\partial t} = -\gamma \boldsymbol{\mu} \times \mathbf{B} \tag{A.7}$$

In this equation, the field $\mathbf{B}$ can now be identified as the sum of the effective field from the magnetic interactions in the material.

[2] Remember that we have defined the Bohr magneton as a positive unit in terms of the electron charge $e > 0$.

### A.2.1. Alternative derivation of the spin dynamical equation

A more formal derivation of the spin dynamical equation can be obtained by finding the classical analogon of the spin commutator relations. In this context Bauer [152], based on the fact that spin operators follow a Lie algebra, refers to Bulgac and Kusnezov [153], who demonstrate that for an arbitrary Lie algebra it is possible to define a Lie-Poisson bracket that naturally connects a quantum commutation relation to a classical counterpart. Accordingly, Bauer [152] shows that for arbitrary functions of spin operators it is possible to use these Lie-Poisson brackets to find the time evolution of a spin in the classical limit, $\hat{\mathbf{S}} \to \mathbf{S}$, thus for the $i$th spin in a lattice it can be proved that

$$\hbar \frac{\partial \mathbf{S}_i}{\partial t} = -\mathbf{S}_i \times \frac{\partial \mathscr{H}}{\partial \mathbf{S}_i} \tag{A.8}$$

where $\mathscr{H} = \mathscr{H}(\{\mathbf{S}\})$ is a function of the spin vectors in the lattice, $\{\mathbf{S}\} = (\mathbf{S}_1, \mathbf{S}_2, \ldots)$, which we relate as the Hamiltonian. In the dynamical equation this term appears as the derivative with respect to the spin vector which we identify as an effective field acting on the spin [152]. Using the standard definition of $\boldsymbol{\mu} = -g\mu_\mathrm{B}\mathbf{S}$ (in this case, $\mathbf{S}$ can be regarded as our previous definition of the spin expectation value), we can redefine this equation as

$$\frac{\partial \boldsymbol{\mu}_i}{\partial t} = -\gamma \boldsymbol{\mu}_i \times \mathbf{H}_\mathrm{eff}^{(i)} \tag{A.9}$$

with

$$\mathbf{H}_\mathrm{eff}^{(i)} = -\frac{\partial \mathscr{H}}{\partial \boldsymbol{\mu}_i} \tag{A.10}$$

We can now redefine $\mathbf{S}$ as the magnetic moment orientation $\boldsymbol{\mu} = g\mu_\mathrm{B}\mathbf{S} = \mu\mathbf{s}$, instead of using it as the spin angular momentum which points antiparallel to the magnetic moment vector.

# Micromagnetic limit of interfacial DMI

Appendix

B



In this chapter we will derive micromagnetic expressions for the interfacial DMI in hexagonal and square lattices, which have been shown by Rohart and Thiaville in Ref. [66]. One of the difficulties for the calculations is knowing the correct orientations of the Dzyaloshinskii vectors in the sample. According to Ref. [49], when a ferromagnetic layer is adjacent to a non-magnetic material with a strong spin-orbit coupling (SOC), an interfacial DMI is induced at the interface and the Dzyaloshinskii vectors are perpendicular to a triangle made of two neighbouring magnetic atoms and an atom from the large SOC system (this is a 3-sites mechanism, see [9, 48] for a thorough explanation). For an FCC(111) surface, the Dzyaloshinskii vectors lie in a plane perpendicular to the vector connecting a site *i* to a site *j* in the magnetic layer, however their out of plane orientation is not completely determined using symmetry assumptions from Dzyaloshinkii's theory. This has been mentioned by Crépieux and Lacroix [48] and Vedmedenko et al. [154], for the case that the DMI originates from the 3-sites mechanism analysed by Levy and Fert [48, 49]. Nevertheless, it is argued [19] that the Dzyaloshinskii vectors mostly lie in plane for a low dimensional system, thus we will choose the vectors according to the convention used by Rohart and Thiaville [66], on the grounds of Moriya's [27] symmetry rules (see Supplementary material of Ref. [63]). This means we approximate the DMI vector as

$$\mathbf{D}_{ij} = \mathbf{r}_{ij} \times \hat{z}\,, \tag{B.1}$$

with $\mathbf{r}_{ij}$ the distance vector from the *i*th to the *j*th site of the lattice, and $z$ as the out of plane direction. Even if $\mathbf{D}_{ij}$ has a $z$ component, the derivatives cancel out in the continuum limit (since we assume invariance of $\mathbf{m}$ along the thickness). These orientations of the Dzyaloshinskii vectors are also seen in Ref. [64] for a central Fe atom with its nearest neighbours, where Simon et al. compute the vectors using first principle calculations.

## B.1. Hexagonal lattice

We will write the derivation of the continuum expression for the interfacial DMI starting from the atomistic formalism and for a hexagonal lattice of lattice constant $a$. The discrete lattice has the structure shown in Fig. B.1.

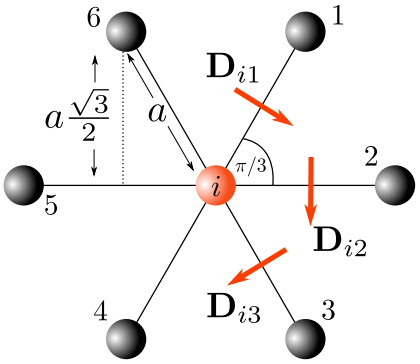


Figure B.1 **Nearest Neighbours of a spin in a hexagonal lattice site *i*..** Dzyaloshinskii-Moriya vectors are defined according to Rohart and Thiaville [66] convention and the in-plane components depicted in [48, 64].

Every lattice site $i$ has 6 nearest neighbours (NN) in symmetrical positions separated by angles of $\pi/3$. According to this, we will compute the interactions with 3 NNs and, because of the symmetry, the other 3 NNs will contribute to the same amount (see details below). The position vectors $\mathbf{r}_{ij}$ from the lattice site $i$ to the position of the $j$th neighbour of the first three NNs, are:

$$\begin{aligned}\mathbf{r}_{i2} &= (x_i + a, y_i, z_i)\\ \mathbf{r}_{i3} &= \left(x_i + \frac{a}{2}, y_i - a\frac{\sqrt{3}}{2}, z_i\right).\end{aligned} \tag{B.2}$$

The Hamiltonian for the Dzyaloshinkii-Moriya Interaction (DMI) is defined as

$$\mathscr{H}_{\text{DM}} = \sum_{\langle i,j\rangle} \mathbf{D}_{ij} \cdot \mathbf{S}_i \times \mathbf{S}_j = \sum_{\langle i,j\rangle} w_{\text{DM}}^{(ij)}. \tag{B.3}$$

In expression B.3, the $\langle i, j\rangle$ label means counting the interactions between every pair of spins *once*. For simplicity we will perform the summation running through every single spin site $i$ in the lattice and computing the energy contribution from every NN, thus interactions will be counted twice for every pair of spins. Additionally, we will only compute the interactions with half of the total nearest neighbours because it is easy to prove that the three others will contribute the same amount. The summation can be redefined as

$$\begin{aligned} E_{\mathrm{DM}} &= \sum_{\langle i,j\rangle} w_{\mathrm{DM}}^{(ij)} \\ &= \frac{1}{2}\sum_{i}\sum_{j\in \mathrm{NN}} w_{\mathrm{DM}}^{(ij)} \\ &= \frac{1}{2}\sum_{i}\left\{ w_{\mathrm{DM}}^{(i\to 1,2,3)} + w_{\mathrm{DM}}^{(i\to 4,5,6)} \right\} \\ &= \sum_{i} w_{\mathrm{DM}}^{(i\to 1,2,3)} \,. \end{aligned} \tag{B.4}$$

According to our reference system, and considering only the in-plane components of the Dzyaloshinskii vectors (we will assume they have the same magnitude) for a FCC(111) surface, they can be described as:

$$\begin{aligned} \mathbf{D}_{i1} &= \left(\frac{a}{2}\hat{x} + a\frac{\sqrt{3}}{2}\hat{y}\right)\times\hat{z} = D_x\hat{x} - D_y\hat{y} \\ \mathbf{D}_{i2} &= (a\hat{x})\times\hat{z} = -D\hat{y} \\ \mathbf{D}_{i3} &= \left(\frac{a}{2}\hat{x} - a\frac{\sqrt{3}}{2}\hat{y}\right)\times\hat{z} = -D_x\hat{x} - D_y\hat{y}\,, \end{aligned} \tag{B.5}$$

with

$$\begin{aligned} D_x &= \frac{\sqrt{3}}{2}D \\ D_y &= \frac{1}{2}D \\ |\mathbf{D}_{i1}| = |\mathbf{D}_{i2}| &= |\mathbf{D}_{i3}| = D \end{aligned} \tag{B.6}$$

Interestingly, when the DMI is originated by Moriya's mechanism (2-sites mechanism) between a (111) surface spin interacting with neighbouring spins in the magnetic layer below it (bulk atoms), the Dzyaloshisnkii vectors can be determined and have a similar structure than the in-plane vectors we consider above (see Table 1 in Ref. [48]).

If we start computing the DMI energy density using the first neighbour, we have

$$w_{\mathrm{DM}}^{(i1)} = \mathbf{D}_{i1}\cdot\left\{\left(S_y^{(i)}S_z^{(1)} - S_z^{(i)}S_y^{(1)}\right)\hat{x} + \left(S_z^{(i)}S_x^{(1)} - S_x^{(i)}S_z^{(1)}\right)\hat{y}\right\}\,, \tag{B.7}$$

where, for $j\in\{1,2,3\}$ (neighbours), we obtain $S_\alpha^{(j)} = S_\alpha(\mathbf{r}_{ij}) = S_\alpha(x_{ij}, y_{ij}, z_{ij})$, $\alpha\in\{x,y,z\}$.

Furthermore, noticing that $\mathbf{S}_\alpha^{(1)} = \mathbf{S}_\alpha(\mathbf{r}_{i1})$, and using the definition of position vectors (equation B.2), we can expand with respect to the nearest neighbours up to order $\mathcal{O}(a)$ (assuming $|a|\ll 1$), as follows

$$
\begin{aligned}
w_{\mathrm{DM}}^{(i1)} =& D_x \left\{ S_y^{(i)} \left( S_z^{(i)} + \frac{a}{2}\frac{\partial S_z^{(i)}}{\partial x} + \frac{a\sqrt{3}}{2}\frac{\partial S_z^{(i)}}{\partial y} \right) \right. \\
& \left. - S_z^{(i)} \left( S_y^{(i)} + \frac{a}{2}\frac{\partial S_y^{(i)}}{\partial x} + \frac{a\sqrt{3}}{2}\frac{\partial S_y^{(i)}}{\partial y} \right) \right\} \\
& - D_y \left\{ S_z^{(i)} \left( S_x^{(i)} + \frac{a}{2}\frac{\partial S_x^{(i)}}{\partial x} + \frac{a\sqrt{3}}{2}\frac{\partial S_x^{(i)}}{\partial y} \right) \right. \\
& \left. - S_x^{(i)} \left( S_z^{(i)} + \frac{a}{2}\frac{\partial S_z^{(i)}}{\partial x} + \frac{a\sqrt{3}}{2}\frac{\partial S_z^{(i)}}{\partial y} \right) \right\},
\end{aligned}
\tag{B.8}
$$

hence

$$
\begin{aligned}
w_{\mathrm{DM}}^{(i1)} =& D_x \frac{a}{2} \left\{ S_y^{(i)} \frac{\partial S_z^{(i)}}{\partial x} + \sqrt{3} S_y^{(i)} \frac{\partial S_z^{(i)}}{\partial y} - S_z^{(i)} \frac{\partial S_y^{(i)}}{\partial x} - \sqrt{3} S_z^{(i)} \frac{\partial S_y^{(i)}}{\partial y} \right\} \\
& - D_y \frac{a}{2} \left\{ S_z^{(i)} \frac{\partial S_x^{(i)}}{\partial x} + \sqrt{3} S_z^{(i)} \frac{\partial S_x^{(i)}}{\partial y} - S_x^{(i)} \frac{\partial S_z^{(i)}}{\partial x} - \sqrt{3} S_x^{(i)} \frac{\partial S_z^{(i)}}{\partial y} \right\}.
\end{aligned}
\tag{B.9}
$$

Analogously

$$
w_{\mathrm{DM}}^{(i2)} = -D \left( S_z^{(i)} S_x^{(2)} - S_x^{(i)} S_z^{(2)} \right)
\tag{B.10}
$$

and

$$
\begin{aligned}
w_{\mathrm{DM}}^{(i3)} =& - D_x \frac{a}{2} \left\{ S_y^{(i)} \frac{\partial S_z^{(i)}}{\partial x} - \sqrt{3} S_y^{(i)} \frac{\partial S_z^{(i)}}{\partial y} - S_z^{(i)} \frac{\partial S_y^{(i)}}{\partial x} + \sqrt{3} S_z^{(i)} \frac{\partial S_y^{(i)}}{\partial y} \right\} \\
& - D_y \frac{a}{2} \left\{ S_z^{(i)} \frac{\partial S_x^{(i)}}{\partial x} - \sqrt{3} S_z^{(i)} \frac{\partial S_x^{(i)}}{\partial y} - S_x^{(i)} \frac{\partial S_z^{(i)}}{\partial x} + \sqrt{3} S_x^{(i)} \frac{\partial S_z^{(i)}}{\partial y} \right\}.
\end{aligned}
\tag{B.11}
$$

Summing these 3 contributions to the DMI energy density, we get

$$
\begin{aligned}
w_{\mathrm{DM}}^{(i\to 1,2,3)} =& w_{\mathrm{DM}}^{(i1)} + w_{\mathrm{DM}}^{(i2)} + w_{\mathrm{DM}}^{(i3)} \\
=& D_x \frac{a}{2} 2\sqrt{3} \left\{ S_y^{(i)} \frac{\partial S_z^{(i)}}{\partial y} - S_z^{(i)} \frac{\partial S_y^{(i)}}{\partial y} \right\} \\
& - D_y \frac{a}{2} 2 \left\{ S_z^{(i)} \frac{\partial S_x^{(i)}}{\partial x} - S_x^{(i)} \frac{\partial S_z^{(i)}}{\partial x} \right\} \\
& - Da \left\{ S_z^{(i)} \frac{\partial S_x^{(i)}}{\partial x} - S_x^{(i)} \frac{\partial S_z^{(i)}}{\partial x} \right\}.
\end{aligned}
\tag{B.12}
$$

The limit to the continuum is straightforward if we correctly define infinitesimal units from the lattice cells. Firstly, taking into account that we are using a two dimensional hexagonal lattice, we can compute a single lattice cell volume using the cross product of the lattice vectors to get the area and, consequently, multiply this area by the thickness

of the sample (which we assume that it has the same structure along $\hat{z}$; we can also consider that we are only describing a monolayer and the thickness is only to get the cells volume). Therefore, using the lattice vectors

$$\mathbf{a} = \frac{a}{2}\hat{x} + \frac{\sqrt{3}}{2}a\hat{y} \qquad \mathbf{b} = a\hat{x}\,, \tag{B.13}$$

the volume of a lattice cell is

$$\Delta V = a_z|\mathbf{a}\times\mathbf{b}| = \frac{\sqrt{3}}{2}a^2 a_z\,. \tag{B.14}$$

Considering the continuum limit for the spins as an average magnetisation in a lattice volume cell at position $i$ as

$$\mathbf{S}_i \longrightarrow \frac{S}{M_s}\mathbf{M}_i\,, \tag{B.15}$$

with saturation magnetisation $M_s$, and using the definitions of $D_x$ and $D_y$, we obtain

$$w_{\mathrm{DM}}^{(i\to 1,2,3)} = D\frac{S^2}{M_s^2}\frac{\sqrt{3}}{2}a\sqrt{3}\left\{M_y^{(i)}\frac{\partial M_z^{(i)}}{\partial y} - M_z^{(i)}\frac{\partial M_y^{(i)}}{\partial y} + M_z^{(i)}\frac{\partial M_x^{(i)}}{\partial x} - M_x^{(i)}\frac{\partial M_z^{(i)}}{\partial x}\right\}. \tag{B.16}$$

Consequently, we can easily get a cell volume dividing the previous expression by $aa_z$ and then treat it as an infinitesimally small volume to turn the summation into an integral. In this limit, the magnetisation will be treated as a field, *i.e.* $\mathbf{M}_i \longrightarrow \mathbf{M}(\mathbf{r})$, and using the Lifshitz invariant definition with normalised magnetisation, $\mathcal{L}_{\mu\nu}^{(\rho)} = m_\mu\partial_\rho m_\nu - m_\nu\partial_\rho m_\mu$, $\mu,\nu,\eta\in\{x,y,z\}$, we arrive to the expressions

$$\begin{aligned} E_{\mathrm{DM}} &= \frac{DS^2}{M_s^2}\sqrt{3}\frac{1}{aa_z}\sum_i \Delta V\left\{M_y^{(i)}\frac{\partial M_z^{(i)}}{\partial y} - M_z^{(i)}\frac{\partial M_y^{(i)}}{\partial y} + M_z^{(i)}\frac{\partial M_x^{(i)}}{\partial x} - M_x^{(i)}\frac{\partial M_z^{(i)}}{\partial x}\right\} \\ &\overset{\Delta V\to 0}{=} DS^2\sqrt{3}\frac{1}{aa_z}\int_V dV\left\{\mathcal{L}_{yz}^{(y)} - \mathcal{L}_{zx}^{(x)}\right\}. \end{aligned} \tag{B.17}$$

Therefore, the micromagnetic DMI energy in a hexagonal lattice of thickness $a_z$ and lattice constant $a$ in the plane, has the structure

$$E_{\mathrm{DM}} = D_c\int_V dV\left\{\mathcal{L}_{yz}^{(y)} + \mathcal{L}_{xz}^{(x)}\right\}, \tag{B.18}$$

with $D_c = DS^2\sqrt{3}(aa_z)^{-1}$.

## B.2. Simple Cubic lattice

In a square lattice the derivation of the DMI in the continuum limit follows the same logic than the derivations performed in Section B.1, if we refer to the Dzyaloshinskii

vector orientations provided by Crépieux and Lacroix in [48]. Starting with the Dzyaloshinskii-Moriya Hamiltonian, the continuum expression can be written as

$$E = D_c \int_V dV \left( \mathcal{L}^{xz}_{(x)} + \mathcal{L}^{yz}_{(y)} \right) , \tag{B.19}$$

where, using the notation of the previous Section,

$$D_c = \frac{DS^2}{aa_z} . \tag{B.20}$$

It is common to find $D_c$ defined by $D$ with the $S$ factor included, *i.e.* $DS^2 \rightarrow D$.

# Micromagnetic limit of the exchange

Appendix

C

The limit to the continuum of the exchange interaction, starting from the discrete spin model, is defined in different textbooks [14,23] but a complete derivation of the expressions is not usually provided. We are interested in hexagonal lattices thus we compute the exchange interaction for this geometry. As shown in Section 1.4.1, the Hamiltonian for the exchange reads

$$\mathscr{H}_{\text{ex}} = -\sum_{\substack{\langle i,j\rangle \\ i\neq j}} \mathbf{S}_i \cdot \mathbf{J}_{ij} \cdot \mathbf{S}_j = -\frac{1}{2}\sum_i \sum_{\substack{j\in \text{NN} \\ i\neq j}} \mathbf{S}_i \cdot \mathbf{J}_{ij} \cdot \mathbf{S}_j \,. \tag{C.1}$$

Assuming that the spin field changes smoothly such that the angle between neighbouring spins is small, we can approximate

$$\mathbf{s}_i \cdot \mathbf{s}_j = \cos\phi_{ij} \approx 1 - \frac{1}{2}\phi_{ij}^2 + \dots \,, \tag{C.2}$$

and by the cosine law we have

$$\phi_{ij}^2 = |\mathbf{s}_i - \mathbf{s}_j|^2 \,. \tag{C.3}$$

Assuming a homogeneous material ($\mathbf{J}_{ij} = J$), the Hamiltonian now reads

$$\mathscr{H}_{\text{ex}} \approx \frac{1}{4} J S^2 \sum_i \sum_{\substack{j\in \text{NN} \\ i\neq j}} |\mathbf{s}_i - \mathbf{s}_j|^2 \,, \tag{C.4}$$

where we have discarded a term that is constant. For the hexagonal lattice, the nearest neighbours are shown in Fig. B.1 and their positions relative to the $i$th lattice site are given by equations B.2. For each neighbour we can expand the spin vectors with respect to the $i$ site assuming that lattice spacings are small, obtaining

$$\begin{aligned} \mathbf{S}_j &= \mathbf{S}(\mathbf{r}_{ij}) \\ &= \mathbf{S}(\mathbf{r}_i + \mathbf{r}_j) \\ &= \mathbf{S}(\mathbf{r}_i) + (\mathbf{r}_j \cdot \boldsymbol{\nabla})\mathbf{S}(\mathbf{r}_i) + \dots \\ &\approx \mathbf{S}_i + (\mathbf{r}_j \cdot \boldsymbol{\nabla})\mathbf{S}_i \end{aligned} \tag{C.5}$$

Now it is possible to compute the summation terms $\phi_{ij}^2$ of equation C.4 for every neigh-

bour:

$$\begin{aligned}\phi_{i1}^2 &= \left(\left[\frac{a}{2}\hat{x} + \frac{\sqrt{3}a}{2}\hat{y}\right] \cdot \boldsymbol{\nabla}\mathbf{s}_i\right)^2 \\ &= \frac{a^2}{4}\left[(\partial_x \mathbf{s}_i)^2 + 3(\partial_y \mathbf{s}_i)^2 + \sqrt{3}(\partial_x \mathbf{s}_i)\cdot(\partial_y \mathbf{s}_i)\right].\end{aligned} \tag{C.6}$$

Similarly

$$\phi_{i2}^2 = a^2(\partial_x \mathbf{s})^2 \tag{C.7}$$

and

$$\begin{aligned}\phi_{i3}^2 &= \left(\left[\frac{a}{2}\hat{x} + \frac{\sqrt{3}a}{2}\hat{y}\right] \cdot \boldsymbol{\nabla}\mathbf{s}_i\right)^2 \\ &= \frac{a^2}{4}\left[(\partial_x \mathbf{s}_i)^2 + 3(\partial_y \mathbf{s}_i)^2 - \sqrt{3}(\partial_x \mathbf{s}_i)\cdot(\partial_y \mathbf{s}_i)\right].\end{aligned} \tag{C.8}$$

Summing up these 3 contributions we get

$$\phi_{i1}^2 + \phi_{i2}^2 + \phi_{i3}^2 = \frac{3}{2}a^2\left[(\partial_x \mathbf{s}_i)^2 + (\partial_y \mathbf{s}_i)^2\right] \tag{C.9}$$

It is easy to see that the other 3 neighbours contribute the same amount to the summation. Defining a cell volume as in Section B.1 with a sample thickness $a_z$, we have

$$\begin{aligned}\mathscr{H}_{\text{ex}} &= \frac{1}{4}JS^2\sum_i 2\left\{\frac{3}{2}a^2\left[(\partial_x \mathbf{s}_i)^2 + (\partial_y \mathbf{s}_i)^2\right]\right\} \\ &= \frac{3}{4}JS^2\frac{2}{\sqrt{3}a_z}\sum_i\left(\frac{\sqrt{3}}{2}a_z a^2\right)\left[(\partial_x \mathbf{s}_i)^2 + (\partial_y \mathbf{s}_i)^2\right]\end{aligned} \tag{C.10}$$

Using the cell volume as an infinitesimal unit, we now set the limit to the continuum

$$\mathscr{H}_{\text{ex}} \overset{\Delta V\to 0}{=} \frac{\sqrt{3}JS^2}{2a_z}\int_\Omega \Delta z\,\mathrm{d}\Omega\left[(\partial_x \mathbf{m})^2 + (\partial_y \mathbf{m})^2\right] \tag{C.11}$$

with the integral defined over an area $\Omega$ and $\mathbf{m}$ as the continuous magnetisation field. We can recognise the relation between the micromagnetic exchange constant with the discrete exchange tensor from the factor in the integral which contains information from the lattice:

$$A = \frac{\sqrt{3}JS^2}{2a_z}. \tag{C.12}$$

# Comparison of magnetic parameters

Appendix

D

- For a square lattice:

$$A = \frac{JS^2}{2a_z} \qquad D_c = \frac{S^2 D}{aa_z} \qquad M_s = \frac{g\mu_B S}{a^2 a_z} \qquad K_u = \frac{\mathcal{K}_u}{a^2 a_z} \tag{D.1}$$

- For a hexagonal lattice:

$$A = \frac{\sqrt{3}JS^2}{2a_z} \qquad D_c = \frac{\sqrt{3}DS^2}{aa_z} \qquad M_s = \frac{g\mu_B S}{\frac{\sqrt{3}}{2}a^2 a_z} \qquad K_u = \frac{\mathcal{K}_u}{\frac{\sqrt{3}}{2}a^2 a_z} \tag{D.2}$$

Micromagnetic parameters: exchange constant $A$, DMI constant $D_c$, saturation magnetisation $M_s$ and uniaxial anisotropy constant $K_u$.

Atomistic parameters: exchange tensor $J$, DMI constant $D$, magnetic moment $\mu = g\mu_B S$, total spin $S$, uniaxial anisotropy constant $\mathcal{K}_u$, lattice constant in plane $a$ and lattice constant along thickness $a_z$.

# Bibliography


[1] D. Cortés-Ortuño, W. Wang, M. Beg, R. A. Pepper, M.-A. Bisotti, R. Carey, M. Vousden, T. Kluyver, O. Hovorka, and H. Fangohr. *Thermal stability and topological protection of skyrmions in nanotracks.* Scientific Reports, **7**(1):4060, 2017.

[2] J. Stöhr and H. C. Siegmann. *Magnetism - From Fundamentals to Nanoscale Dynamics*, volume 152 of *Springer Series in Solid-State Sciences*. Springer-Verlag Berlin Heidelberg, first edition, 2006.

[3] H. J. Richter. *Recent advances in the recording physics of thin-film media.* Journal of Physics D: Applied Physics, **32**(23):3092–3092, 1999.

[4] H. J. Richter. *The transition from longitudinal to perpendicular recording.* Journal of Physics D: Applied Physics, **40**(9):R149–R177, 2007.

[5] R. L. Stamps, S. Breitkreutz, J. Åkerman, A. V. Chumak, Y. Otani, G. E. W. Bauer, J.-U. Thiele, M. Bowen, S. a. Majetich, M. Kläui, I. L. Prejbeanu, B. Dieny, N. M. Dempsey, and B. Hillebrands. *The 2014 Magnetism Roadmap.* Journal of Physics D: Applied Physics, **47**(33):333001, 2014.

[6] Y. Shiroishi, K. Fukuda, I. Tagawa, H. Iwasaki, S. Takenoiri, H. Tanaka, H. Mutoh, and N. Yoshikawa. *Future options for HDD storage.* IEEE Transactions on Magnetics, **45**(10):3816–3822, 2009.

[7] N. Nagaosa and Y. Tokura. *Topological properties and dynamics of magnetic skyrmions.* Nature nanotechnology, **8**(12):899–911, 2013.

[8] R. Wiesendanger. *Nanoscale magnetic skyrmions in metallic films and multilayers: a new twist for spintronics.* Nature Reviews Materials, **1**(6):16044, 2016.

[9] A. Fert, N. Reyren, and V. Cros. *Magnetic skyrmions: advances in physics and potential applications.* Nature Reviews Materials, **2**(17031):1–15, 2017.

[10] W. F. Brown. *Thermal Fluctuations of a Single-Domain Particle.* Physical Review, **130**(5):1677–1686, 1963.

[11] H. Jónsson, G. Mills, and K. W. Jacobsen. *Nudged elastic band method for finding minimum energy paths of transitions.* Classical and Quantum Dynamics in Condensed Phase Simulations - Proceedings of the International School of Physics, pages 385–404, 1998.

[12] G. Henkelman, G. Jóhannesson, and H. Jónsson. *Methods for Finding Saddle Points and Minimum Energy Paths.* Theoretical Methods in Condensed Phase Chemistry, **5**:269–300, 2002.

[13] P. F. Bessarab, V. M. Uzdin, and H. Jónsson. *Method for finding mechanism and activation energy of magnetic transitions, applied to skyrmion and antivortex annihilation.* Computer Physics Communications, **196**:1–37, 2015.

[14] A. Aharoni. *Introduction to the Theory of Ferromagnetism*, volume 109. Oxford University Press, second edition, 2000.

[15] W. Greiner. *Quantum Mechanics.* Springer-Verlag Berlin Heidelberg, 4th edition, 2000.

[16] A. G. Gurevich and G. A. Melkov. *Magnetization Oscillations and Waves.* CRC Press, Inc, 1996.

[17] W. Nolting and A. Ramakanth. *Quantum Theory of Magnetism.* Springer Berlin Heidelberg, first edition, 2009.

[18] S. Blügel and G. Bihlmayer. *Magnetism of Low-dimensional Systems: Theory.* In Handbook of Magnetism and Advanced Magnetic Materials, volume 1: Fundamentals and Theory, pages 1–42. John Wiley & Sons, Ltd, 2007.

[19] S. Heinze, K. von Bergmann, M. Menzel, J. Brede, A. Kubetzka, R. Wiesendanger, and G. B. S. Blügel. *Spontaneous atomic-scale magnetic skyrmion lattice in two dimensions.* Nature Physics, **7**:713–718, 2011.

[20] P. Ferriani, K. von Bergmann, E. Vedmedenko, S. Heinze, M. Bode, M. Heide, G. Bihlmayer, S. Blügel, and R. Wiesendanger. *Atomic-Scale Spin Spiral with a Unique Rotational Sense: Mn Monolayer on W(001).* Physical Review Letters, **101**(2):027201, 2008.

[21] M. Bode, E. Vedmedenko, K. von Bergmann, A. Kubetzka, P. Ferriani, S. Heinze, and R. Wiesendanger. *Atomic spin structure of antiferromagnetic domain walls.* Nature materials, **5**(6):477–481, 2006.

[22] T. Gilbert. *A Phenomenological Theory of Damping in Ferromagnetic Materials.* IEEE Transactions on Magnetics, **40**(6):3443–3449, 2004.

[23] S. Chikazumi. *Physics of Ferromagnetism*, volume 94 of *International Series of Monographs on Physics.* Oxford University Press, second edition, 2009.

[24] P. Bruno. *Physical origins and theoretical models of magnetic anisotropy*. In Magnetismus von Festkörpern und Grenzflächen, page 950. Forschungszentrum Jülich, 1993.

[25] J. Lindner and M. Farle. *Magnetic Anisotropy of Heterostructures*. In Magnetic Heterostructures, volume 227 of *Springer Tracts in Modern Physics*, pages 45–96. Springer Berlin Heidelberg, Berlin, Heidelberg, 2008.

[26] I. Dzyaloshinskii. *A thermodynamic theory of "weak" ferromagnetism of antiferromagnetics*. Journal of Physics and Chemistry of Solids, **4**(4):241–255, 1958.

[27] T. Moriya. *Anisotropic superexchange interaction and weak ferromagnetism*. Physical Review, **120**(1):91–98, 1960.

[28] A. Bogdanov and D. Yablonskii. *Thermodynamically stable "vortices" in magnetically ordered crystals. The mixed state of magnets*. Zh. Eksp. Teor. Fiz, **95**(1):178, 1989.

[29] A. N. Bogdanov, M. V. Kudinov, and D. A. Yablonskii. *Theory of magnetic vortices in easy-axis ferromagnets*. Sov. Phys. Solid State, **31**(10):1707–1710, 1989.

[30] A. Bogdanov and A. Hubert. *Thermodynamically stable magnetic vortex states in magnetic crystals*. Journal of magnetism and magnetic materials, **138**(3):255–269, 1994.

[31] A. Bogdanov and A. Hubert. *Stability of vortex-like structures in uniaxial ferromagnets*. Journal of Magnetism and Magnetic Materials, **195**(1):182–192, 1999.

[32] L. D. Landau and E. Lifshitz. *Statistical Physics*, volume 5 of *Course of Theoretical Physics*. Butterworth-Heinemann, third edition, 1980.

[33] I. E. Dzyaloshinskii. *Theory of helicoidal structures in antiferromagnets. II. Metals*. Soviet Physics JETP, **19**(4):960–971, 1964.

[34] P. Bak and M. H. Jensen. *Theory of helical magnetic structures and phase transitions in MnSi and FeGe*. Journal of Physics C: Solid State Physics, **13**(31):L881–L885, 1980.

[35] X. Z. Yu, N. Kanazawa, Y. Onose, K. Kimoto, W. Z. Zhang, S. Ishiwata, Y. Matsui, and Y. Tokura. *Near room-temperature formation of a skyrmion crystal in thin-films of the helimagnet FeGe*. Nature Materials, **10**(2):106–109, 2011.

[36] D. McGrouther, R. J. Lamb, M. Krajnak, S. McFadzean, S. McVitie, R. L. Stamps, A. O. Leonov, A. N. Bogdanov, and Y. Togawa. *Internal structure of hexagonal skyrmion lattices in cubic helimagnets*. New Journal of Physics, **18**(9):095004, 2016.

[37] S. Mühlbauer, B. Binz, F. Jonietz, C. Pfleiderer, A. Rosch, A. Neubauer, R. Georgii, and P. Böni. *Skyrmion Lattice in a Chiral Magnet*. Science, **323**(5916):915–919, 2009.

[38] T. Tanigaki, K. Shibata, N. Kanazawa, X. Yu, Y. Onose, H. S. Park, D. Shindo, and Y. Tokura. *Real-Space Observation of Short-Period Cubic Lattice of Skyrmions in MnGe*. Nano Letters, **15**(8):5438–5442, 2015.

[39] X. Z. Yu, Y. Onose, N. Kanazawa, J. H. Park, J. H. Han, Y. Matsui, N. Nagaosa, and Y. Tokura. *Real-space observation of a two-dimensional skyrmion crystal*. Nature, **465**(7300):901–904, 2010.

[40] W. Münzer, A. Neubauer, T. Adams, S. Mühlbauer, C. Franz, F. Jonietz, R. Georgii, P. Böni, B. Pedersen, M. Schmidt, A. Rosch, and C. Pfleiderer. *Skyrmion lattice in the doped semiconductor $Fe_{1-x}Co_xSi$*. Physical Review B, **81**:041203, 2010.

[41] P. Milde, D. Köhler, J. Seidel, L. M. Eng, A. Bauer, A. Chacon, J. Kindervater, S. Mühlbauer, C. Pfleiderer, S. Buhrandt, C. Schütte, and A. Rosch. *Unwinding of a Skyrmion Lattice by Magnetic Monopoles*. Science, **340**(6136):1076–1080, 2013.

[42] S. Seki, X. Z. Yu, S. Ishiwata, and Y. Tokura. *Observation of Skyrmions in a Multiferroic Material*. Science, **336**(6078):198–201, 2012.

[43] S. L. Zhang, G. van der Laan, and T. Hesjedal. *Direct experimental determination of the topological winding number of skyrmions in $Cu_2OSeO_3$*. Nature Communications, **8**(14619):1–7, 2017.

[44] Y. Tokunaga, X. Z. Yu, J. S. White, H. M. Rønnow, D. Morikawa, Y. Taguchi, and Y. Tokura. *A new class of chiral materials hosting magnetic skyrmions beyond room temperature*. Nature Communications, **6**:7638, 2015.

[45] W. Li, C. Jin, R. Che, W. Wei, L. Lin, L. Zhang, H. Du, M. Tian, and J. Zang. *Emergence of skyrmions from rich parent phases in the molybdenum nitrides*. Physical Review B, **93**:060409, 2016.

[46] A. K. Nayak, V. Kumar, T. Ma, P. Werner, E. Pippel, R. Sahoo, F. Damay, U. K. Rößler, C. Felser, and S. S. P. Parkin. *Magnetic antiskyrmions above room temperature in tetragonal Heusler materials*. Nature, **548**(7669):561–566, 2017.

[47] I. Kezsmarki, S. Bordacs, P. Milde, E. Neuber, L. M. Eng, J. S. White, H. M. Ronnow, C. D. Dewhurst, M. Mochizuki, K. Yanai, H. Nakamura, D. Ehlers, V. Tsurkan, and A. Loidl. *Neel-type skyrmion lattice with confined orientation in the polar magnetic semiconductor GaV4S8*. Nature Materials, **14**(11):1116–1122, 2015.

[48] A. Crépieux and C. Lacroix. *Dzyaloshinsky-Moriya interactions induced by symmetry breaking at a surface*. Journal of Magnetism and Magnetic Materials, **182**(3):341–349, 1998.

[49] A. Fert, V. Cros, and J. Sampaio. *Skyrmions on the track.* Nature Nanotechnology, **8**(3):152–156, 2013.

[50] C. Moreau-Luchaire, C. Moutafis, N. Reyren, J. Sampaio, C. A. F. Vaz, N. Van Horne, K. Bouzehouane, K. Garcia, C. Deranlot, P. Warnicke, P. Wohlhüter, J.-M. George, M. Weigand, J. Raabe, V. Cros, and A. Fert. *Additive interfacial chiral interaction in multilayers for stabilization of small individual skyrmions at room temperature.* Nature Nanotechnology, **11**(5):444–448, 2016.

[51] O. Boulle, J. Vogel, H. Yang, S. Pizzini, D. de Souza Chaves, A. Locatelli, T. O. Menteş, A. Sala, L. D. Buda-Prejbeanu, O. Klein, M. Belmeguenai, Y. Roussigné, A. Stashkevich, S. M. Chérif, L. Aballe, M. Foerster, M. Chshiev, S. Auffret, I. M. Miron, and G. Gaudin. *Room-temperature chiral magnetic skyrmions in ultrathin magnetic nanostructures.* Nature Nanotechnology, **11**(5):449–454, 2016.

[52] S. Woo, K. Litzius, B. Kruger, M.-Y. Im, L. Caretta, K. Richter, M. Mann, A. Krone, R. M. Reeve, M. Weigand, P. Agrawal, I. Lemesh, M.-A. Mawass, P. Fischer, M. Klaui, and G. S. D. Beach. *Observation of room-temperature magnetic skyrmions and their current-driven dynamics in ultrathin metallic ferromagnets.* Nature Materials, **15**(5):501–506, 2016.

[53] X. Ma, G. Yu, X. Li, T. Wang, D. Wu, K. S. Olsson, Z. Chu, K. An, J. Q. Xiao, K. L. Wang, and X. Li. *Interfacial control of Dzyaloshinskii-Moriya interaction in heavy metal/ferromagnetic metal thin film heterostructures.* Physical Review B, **94**:180408, 2016.

[54] W. Legrand, D. Maccariello, N. Reyren, K. Garcia, C. Moutafis, C. Moreau-Luchaire, S. Colin, K. Bouzehouane, V. Cros, and A. Fert. *Room-temperature current-induced generation and motion of sub-100nm skyrmions.* Nano Letters, 2017.

[55] S. D. Pollard, J. A. Garlow, J. Yu, Z. Wang, Y. Zhu, and H. Yang. *Observation of stable Néel skyrmions in cobalt/palladium multilayers with Lorentz transmission electron microscopy.* Nature Communications, **8**, 2017.

[56] N. Romming, C. Hanneken, M. Menzel, J. E. Bickel, B. Wolter, K. von Bergmann, A. Kubetzka, and R. Wiesendanger. *Writing and Deleting Single Magnetic Skyrmions.* Science, **341**(6146):636–639, 2013.

[57] J. Hagemeister, N. Romming, K. von Bergmann, E. Y. Vedmedenko, and R. Wiesendanger. *Stability of single skyrmionic bits.* Nature Communications, **6**(8455), 2015.

[58] N. Romming, A. Kubetzka, C. Hanneken, K. von Bergmann, and R. Wiesendanger. *Field-Dependent Size and Shape of Single Magnetic Skyrmions.* Physical Review Letters, **114**(17):1–5, 2015.

[59] K. von Bergmann, M. Menzel, A. Kubetzka, and R. Wiesendanger. *Influence of the Local Atom Configuration on a Hexagonal Skyrmion Lattice.* Nano Letters, **15**(5):3280–3285, 2015.

[60] M. Bode, M. Heide, K. von Bergmann, P. Ferriani, S. Heinze, G. Bihlmayer, a. Kubetzka, O. Pietzsch, S. Blügel, and R. Wiesendanger. *Chiral magnetic order at surfaces driven by inversion asymmetry.* Nature, **447**(7141):190–193, 2007.

[61] K. von Bergmann, A. Kubetzka, O. Pietzsch, and R. Wiesendanger. *Interface-induced chiral domain walls, spin spirals and skyrmions revealed by spin-polarized scanning tunneling microscopy.* Journal of Physics: Condensed Matter, **26**(39):394002, 2014.

[62] J. Cho, N.-H. Kim, S. Lee, J.-s. Kim, R. Lavrijsen, A. Solignac, Y. Yin, D.-S. Han, N. J. J. van Hoof, H. J. M. Swagten, B. Koopmans, C.-Y. You, N. J. J. V. Hoof, and H. J. M. Swagten. *Thickness dependence of the interfacial Dzyaloshinskii–Moriya interaction in inversion symmetry broken systems.* Nature Communications, **6**(7635):1–7, 2015.

[63] H. Yang, A. Thiaville, S. Rohart, A. Fert, and M. Chshiev. *Anatomy of Dzyaloshinskii-Moriya Interaction at Co/Pt Interfaces.* Physical Review Letters, **115**(26):1–5, 2015.

[64] E. Simon, K. Palotas, and L. Rozsa. *Formation of magnetic skyrmions with tunable properties in PdFe bilayer deposited on Ir (111).* Physical Review B, **094410**(90):1–7, 2014.

[65] R. Skomski, a. Kashyap, J. Zhou, and D. J. Sellmyer. *Anisotropic exchange.* Journal of Applied Physics, **97**(10):2005–2007, 2005.

[66] S. Rohart and A. Thiaville. *Skyrmion confinement in ultrathin film nanostructures in the presence of Dzyaloshinskii-Moriya interaction.* Physical Review B, **88**(18):184422, 2013.

[67] N. S. Kiselev, A. N. Bogdanov, R. Schäfer, and U. K. Rößler. *Chiral skyrmions in thin magnetic films: new objects for magnetic storage technologies?* Journal of Physics D: Applied Physics, **44**(39):392001, 2011.

[68] A. Leonov. *Twisted, localized, and modulated states described in the phenomenological theory of chiral and nanoscale ferromagnets.* Dr. rer. nat. Dissertation, Technischen Universität Dresden, 2012.

[69] A. O. Leonov, T. L. Monchesky, N. Romming, A. Kubetzka, A. N. Bogdanov, and R. Wiesendanger. *The properties of isolated chiral skyrmions in thin magnetic films.* New Journal of Physics, **18**(6):1–12, 2015.

[70] J. E. Miltat and M. J. Donahue. *Numerical micromagnetics: finite difference methods*. In Handbook of Magnetism and Advanced Magnetic Materials, volume 2: Micromagnetism, pages 1–23. John Wiley & Sons, Ltd, 2007.

[71] R. F. L. Evans, W. J. Fan, P. Chureemart, T. a. Ostler, M. O. a. Ellis, and R. W. Chantrell. *Atomistic spin model simulations of magnetic nanomaterials*. Journal of Physics: Condensed Matter, **26**(10):103202, 2014.

[72] D. Chernyshenko and H. Fangohr. *Computing the demagnetizing tensor for finite difference micromagnetic simulations via numerical integration*. Journal of Magnetism and Magnetic Materials, **381**:440–445, 2015.

[73] W. Wang. *Computer simulation studies of complex magnetic materials*. Doctoral thesis, Faculty of Engineering and the Environment, University of Southampton, 2015.

[74] J. Miltat, G. Albuquerque, and A. Thiaville. *An Introduction to Micromagnetics in the Dynamic Regime*. In Spin Dynamics in Confined Magnetic Structures I, page 336. Springer Science and Business Media, 2002.

[75] D. Wei. *Micromagnetics and Recording Materials*. SpringerBriefs in Applied Sciences and Technology. Springer Berlin Heidelberg, Berlin, Heidelberg, 2012.

[76] A. Hubert and R. Schäfer. *Magnetic domains*, volume 21. Springer, 1998.

[77] University of Southampton. Finmag: Micromagnetic Simulation Framework (2012-2015).

[78] D. Cortés-Ortuño, W. Wang, R. Pepper, M.-A. Bisotti, T. Kluyver, M. Vousden, and H. Fangohr. Fidimag v2.0. Zenodo doi:10.5281/zenodo.167858, 2016. `http://computationalmodelling.github.io/fidimag/`.

[79] B. Berg and M. Lüscher. *Definition and statistical distributions of a topological number in the lattice $O(3)$ $\sigma$–model*. Nuclear Physics, Section B, **190**(2):412–424, 1981.

[80] G. Yin, Y. Li, L. Kong, R. K. Lake, C. L. Chien, and J. Zang. *Topological charge analysis of ultrafast single skyrmion creation*. Physical Review B, **93**(17):174403, 2016.

[81] Nature Publishing Group. *Skyrmion Makeover*. Nature, **465**:846, 2010.

[82] C. Pfleiderer. *Magnetic order: Surfaces get hairy*. Nature Physics, **7**(9):673–674, 2011.

[83] R. Streubel, L. Han, M.-Y. Im, F. Kronast, U. K. Rößler, F. Radu, R. Abrudan, G. Lin, O. G. Schmidt, P. Fischer, and D. Makarov. *Manipulating Topological States by Imprinting Non-Collinear Spin Textures*. Scientific Reports, **5**:8787, 2015.

[84] W. Jiang, X. Zhang, G. Yu, W. Zhang, X. Wang, M. Benjamin Jungfleisch, J. E. Pearson, X. Cheng, O. Heinonen, K. L. Wang, Y. Zhou, A. Hoffmann, and S. G. E. te Velthuis. *Direct observation of the skyrmion Hall effect*. Nature Physics, **13**(2):162–169, 2017.

[85] K. Everschor-Sitte and M. Sitte. *Real-space Berry phases: Skyrmion soccer (invited)*. Journal of Applied Physics, **115**(17):172602, 2014.

[86] J. Sampaio, V. Cros, S. Rohart, a. Thiaville, and A. Fert. *Nucleation, stability and current-induced motion of isolated magnetic skyrmions in nanostructures*. Nature Nanotechnology, **8**(11):839–44, 2013.

[87] J. Iwasaki, M. Mochizuki, and N. Nagaosa. *Current-induced skyrmion dynamics in constricted geometries*. Nature Nanotechnology, **8**:742–747, 2013.

[88] Ulrich K. Rößler, A. A. Leonov, and A. N. Bogdanov. *Chiral Skyrmionic matter in non-centrosymmetric magnets*. Journal of Physics: Conference Series, **303**(1):13, 2011.

[89] U. K. Rößler, A. N. Bogdanov, and C. Pfleiderer. *Spontaneous skyrmion ground states in magnetic metals*. Nature, **442**(7104):797–801, 2006.

[90] J. C. Gallagher, K. Y. Meng, J. T. Brangham, H. L. Wang, B. D. Esser, D. W. McComb, and F. Y. Yang. *Robust Zero-Field Skyrmion Formation in FeGe Epitaxial Thin Films*. Physical Review Letters, **118**:027201, 2017.

[91] M. Beg, R. Carey, W. Wang, D. Cortés-Ortuño, M. Vousden, M.-A. Bisotti, M. Albert, D. Chernyshenko, O. Hovorka, R. L. Stamps, and H. Fangohr. *Ground state search, hysteretic behaviour, and reversal mechanism of skyrmionic textures in confined helimagnetic nanostructures*. Scientific Reports, **5**(October):17137, 2015.

[92] A. B. Borisov and F. N. Rybakov. *Spiral structures in helical magnets*. JETP Letters, **96**(8):521–524, 2012.

[93] Y.-O. Tu. *Determination of Magnetization of Micromagnetic Wall in Bubble Domains by Direct Minimization*. Journal of Applied Physics, **42**(13):5704, 1971.

[94] K. Y. Guslienko. *Nanomagnetics Skyrmion State Stability in Magnetic Nanodots With Perpendicular Anisotropy*. IEEE Magnetics Letters, **6**(4000104), 2015.

[95] W. Döring. *Point singularities in micromagnetism*. Journal of Applied Physics, **39**(2):1006–1007, 1968.

[96] A. Thiaville, J. M. García, R. Dittrich, J. Miltat, and T. Schrefl. *Micromagnetic study of Bloch-point-mediated vortex core reversal*. Physical Review B, **67**(9):094410, 2003.

[97] A. D. Verga. *Skyrmion to ferromagnetic state transition: A description of the topological change as a finite-time singularity in the skyrmion dynamics.* Physical Review B, **90**(174428):1–8, 2014.

[98] R. Hertel and C. M. Schneider. *Exchange explosions: Magnetization dynamics during vortex-antivortex annihilation.* Physical Review Letters, **97**(17):1–4, 2006.

[99] S. Gliga, Y. Liu, and R. Hertel. *Energy thresholds in the magnetic vortex core reversal.* Journal of Physics: Conference Series, **303**:12005, 2011.

[100] R. G. Elías and A. Verga. *Magnetization structure of a Bloch point singularity.* European Physical Journal B, **82**(2):159–166, 2011.

[101] J. Miltat and A. Thiaville. *Vortex cores – Smaller than small.* Science, **298**(5593):555, 2002.

[102] C. Andreas, S. Gliga, and R. Hertel. *Numerical micromagnetism of strong inhomogeneities.* Journal of Magnetism and Magnetic Materials, **362**:7–13, 2014.

[103] G. Henkelman and H. Jónsson. *Improved tangent estimate in the nudged elastic band method for finding minimum energy paths and saddle points.* The Journal of Chemical Physics, **113**(22):9978–9985, 2000.

[104] R. Dittrich, T. Schrefl, D. Suess, W. Scholz, H. Forster, and J. Fidler. *A path method for finding energy barriers and minimum energy paths in complex micromagnetic systems.* Journal of Magnetism and Magnetic Materials, **250**:12–19, 2002.

[105] D. Suess, S. Eder, J. Lee, R. Dittrich, and J. Fidler. *Reliability of Sharrocks equation for exchange spring bilayers.* Physical Review B, **75**:174430, 2007.

[106] W. Scholz, J. Fidler, T. Schrefl, and D. Suess. *Scalable parallel micromagnetic solvers for magnetic nanostructures.* Computational Materials Science, **28**(2):366–383, 2003.

[107] G. Hrkac, S. Bance, a. Goncharov, T. Schrefl, and D. Suess. *Thermal stability of bubble domains in ferromagnetic discs.* Journal of Physics D: Applied Physics, **40**(9):2695–2698, 2007.

[108] C. Vogler, F. Bruckner, B. Bergmair, T. Huber, D. Suess, and C. Dellago. *Simulating rare switching events of magnetic nanostructures with forward flux sampling.* Physical Review B, **88**(13):134409, 2013.

[109] S. Rohart, J. Miltat, and A. Thiaville. *Path to collapse for an isolated Néel skyrmion.* Physical Review B, **93**(21):214412, 2016.

[110] I. S. Lobanov, H. Jónsson, and V. M. Uzdin. *Mechanism and activation energy of magnetic skyrmion annihilation obtained from minimum energy path calculations.* Physical Review B, **94**(17), 2016.

[111] D. Stosic, J. Mulkers, B. Van Waeyenberge, T. B. Ludermir, and M. V. Milošević. *Paths to collapse for isolated skyrmions in few-monolayer ferromagnetic films*. Physical Review B, **95**:214418, 2017.

[112] S. von Malottki, B. Dupé, P. F. Bessarab, A. Delin, and S. Heinze. *Enhanced skyrmion stability due to exchange frustration*. Scientific Reports, **7**(1):12299, 2017.

[113] P. F. Bessarab, G. P. Müller, I. S. Lobanov, F. N. Rybakov, N. S. Kiselev, H. Jónsson, V. M. Uzdin, S. Blügel, L. Bergqvist, and A. Delin. *Annihilation mechanisms and lifetime of racetrack skyrmions*. Preprint at arXiv:1706.07173, 2017.

[114] G. Henkelman, B. P. Uberuaga, and H. Jónsson. *A climbing image nudged elastic band method for finding saddle points and minimum energy paths*. The Journal of Chemical Physics, **113**(22):9901, 2000.

[115] A. C. Hindmarsh, P. N. Brown, K. E. Grant, S. L. Lee, R. Serban, D. E. Shumaker, and C. S. Woodward. *SUNDIALS: Suite of Nonlinear and Differential/ Algebraic Equation Solvers*. ACM Trans. Math. Software, pages 363–396, 2005.

[116] Fidimag Documentation. Online (Accessed: 3rd of July of 2017). `http://fidimag.readthedocs.io/en/latest/?badge=latest`.

[117] P. Landeros, S. Allende, J. Escrig, E. Salcedo, D. Altbir, and E. E. Vogel. *Reversal modes in magnetic nanotubes*. Applied Physics Letters, **90**(10):–, 2007.

[118] J. López-López, D. Cortés-Ortuño, and P. Landeros. *Role of anisotropy on the domain wall properties of ferromagnetic nanotubes*. Journal of Magnetism and Magnetic Materials, **324**(13):2024–2029, 2012.

[119] D. Cortés-Ortuño and H. Fangohr. Test system for Nudged Elastic Band Method in nanoscale magnetism. Zenodo doi:10.5281/zenodo.167870, 2016. `https://doi.org/10.5281/zenodo.167870`.

[120] G. Yu, P. Upadhyaya, X. Li, W. Li, S. K. Kim, Y. Fan, K. L. Wong, Y. Tserkovnyak, P. K. Amiri, and K. L. Wang. *Room-Temperature Creation and Spin–Orbit Torque Manipulation of Skyrmions in Thin Films with Engineered Asymmetry*. Nano letters, **16**(3):1981–1988, 2016.

[121] S. S. P. Parkin, M. Hayashi, and L. Thomas. *Magnetic domain-wall racetrack memory*. Science, **320**(5873):190–194, 2008.

[122] W. F. Brown Jr. *Micromagnetics*. John Wiley & Sons Inc., 1963.

[123] G. Adam. *New approach to Lorentz approximation in micromagnetism*. Journal of Applied Physics, **43**(11):4763, 1972.

[124] T. Jourdan, A. Marty, and F. Lançon. *Multiscale method for Heisenberg spin simulations*. Physical Review B, **77**(22):224428, 2008.

[125] T. Jourdan. *Approche multiéchelle pour le magnétisme . Application aux hétérogénéités structurales et aux singularités magnétiques*. PhD thesis, Université Joseph Fourier, 2008.

[126] J.-W. Yoo, S.-J. Lee, J.-H. Moon, and K.-J. Lee. *Phase Diagram of a Single Skyrmion in Magnetic Nanowires*. IEEE Transactions on Magnetics, **50**(11):2–5, 2014.

[127] R. G. Elías and A. D. Verga. *Topological changes of two-dimensional magnetic textures*. Physical Review B, **89**(134405):9, 2014.

[128] T. Schrefl, H. Forster, D. Suess, S. Werner, T. Vassilios, and J. Fidler. *Micromagnetic Simulation of Switching Events*. In Advances in Solid State Physics, volume 41, pages 623–635. Springer Berlin Heidelberg, 2001.

[129] D. Weller, G. Parker, O. Mosendz, E. Champion, B. Stipe, X. Wang, T. Klemmer, G. Ju, and A. Ajan. *A HAMR Media Technology Roadmap to an Areal Density of 4 Tb/in*$^2$. IEEE Transactions on Magnetics, **50**(1):1–8, 2014.

[130] J. Müller, A. Rosch, and M. Garst. *Edge instabilities and skyrmion creation in magnetic layers*. New Journal of Physics, **18**(065006):1–13, 2016.

[131] D. Cortés-Ortuño and H. Fangohr. Thermal stability and topological protection of skyrmions: Supplementary data. Zenodo doi:10.5281/zenodo.167874, 2016. `https://doi.org/10.5281/zenodo.167870`.

[132] G. Finocchio, F. Büttner, R. Tomasello, M. Carpentieri, and M. Kläui. *Magnetic skyrmions: from fundamental to applications*. Journal of Physics D: Applied Physics, **49**(42):423001, 2016.

[133] A. O. Leonov, Y. Togawa, T. L. Monchesky, A. N. Bogdanov, J. Kishine, Y. Kousaka, M. Miyagawa, T. Koyama, J. Akimitsu, T. Koyama, K. Harada, S. Mori, D. McGrouther, R. Lamb, M. Krajnak, S. McVitie, R. L. Stamps, and K. Inoue. *Chiral Surface Twists and Skyrmion Stability in Nanolayers of Cubic Helimagnets*. Physical Review Letters, **117**:087202, 2016.

[134] K. Shibata, A. Kovács, N. S. Kiselev, N. Kanazawa, R. E. Dunin-Borkowski, and Y. Tokura. *Temperature and Magnetic Field Dependence of the Internal and Lattice Structures of Skyrmions by Off-Axis Electron Holography*. Physical Review Letters, **118**:087202, 2017.

[135] B. Dupé, M. Hoffmann, C. Paillard, and S. Heinze. *Tailoring magnetic skyrmions in ultra-thin transition metal films*. Nature Communications, **5**(May):4030, 2014.

[136] H. J. G. Draaisma and W. J. M. de Jonge. *Surface and volume anisotropy from dipole-dipole interactions in ultrathin ferromagnetic films.* Journal of Applied Physics, **64**(7):3610–3613, 1988.

[137] A. O. Leonov, U. K. Rößler, and M. Mostovoy. Target-skyrmions and skyrmion clusters in nanowires of chiral magnets. In EPJ Web of Conferences, volume 75, page 05002. EDP Sciences, 2014.

[138] J. D. Hunter. *Matplotlib: A 2D Graphics Environment.* Computing in Science Engineering, **9**(3):90–95, 2007.

[139] T. Kluyver, B. Ragan-Kelley, F. Përez, B. Granger, M. Bussonnier, J. Frederic, K. Kelley, J. Hamrick, J. Grout, S. Corlay, P. Ivanov, D. Avila, S. Abdalla, C. Willing, and J. D. Team. Project Jupyter: Open source, interactive data science, scientific computing across over 40 programming languages. In Positioning and Power in Academic Publishing: Players, Agents and Agendas, Proceedings of the 20th International Conference on Electronic Publishing, pages 87–90. IOS Press BV, 2016.

[140] T. C. Schulthess. *Programming revisited.* Nature Physics, **11**(5):369–373, 2015.

[141] T. Hey and M. C. Payne. *Open science decoded.* Nature Physics, **11**(5):367–369, 2015.

[142] J. Fehr, J. Heiland, C. Himpe, and J. Saak. *Best practices for replicability, reproducibility and reusability of computer-based experiments exemplified by model reduction software.* AIMS Mathematics, **1**(Math-01-00261):261, 2016.

[143] M. R. Munafò, B. A. Nosek, D. V. Bishop, K. S. Button, C. D. Chambers, N. P. du Sert, U. Simonsohn, E.-J. Wagenmakers, J. J. Ware, and J. P. Ioannidis. *A manifesto for reproducible science.* Nature Human Behaviour, **1**:0021, 2017.

[144] D. C. Ince, L. Hatton, and J. Graham-Cumming. *The case for open computer programs.* Nature, **482**(7386):485–488, 2012.

[145] N. M. Editorial. *Social software.* Nature Methods, **4**(3):189–189, 2007.

[146] N. M. Editorial. *Enhancing reproducibility.* Nature Methods, **10**(5):367–367, 2013.

[147] D. S. Chawla. *The unsung heroes of scientific software.* Nature, **529**(7584):115, 2016.

[148] K. E. Niemeyer, A. M. Smith, and D. S. Katz. *The Challenge and Promise of Software Citation for Credit, Identification, Discovery, and Reuse.* J. Data and Information Quality, **7**(4):16:1–16:5, 2016.

[149] D. Merkel. *Docker: Lightweight Linux Containers for Consistent Development and Deployment*. Linux J., **2014**(239), 2014.

[150] C. Boettiger. *An Introduction to Docker for Reproducible Research*. SIGOPS Oper. Syst. Rev., **49**(1):71–79, 2015.

[151] J. D. Jackson. *Classical electrodynamics*. John Wiley & Sons, 2007.

[152] D. Bauer. *Atomistic Spin-Dynamics in Confined Magnetic Nano-Structures*. Diplomarbeit in physik, Fakultät für Mathematik, Informatik und Naturwissenschaften der Rheinisch-Westfälischen Technischen Hochschule Aachen, 2008.

[153] A. Bulgac and D. Kusnezov. *Classical limit for Lie algebras*. Annals of Physics, **199**(1):187–224, 1990.

[154] E. Y. Vedmedenko, L. Udvardi, P. Weinberger, and R. Wiesendanger. *Chiral magnetic ordering in two-dimensional ferromagnets with competing Dzyaloshinsky-Moriya interactions*. Physical Review B, **75**(104431):1–8, 2007.